Article

A Phenomenological Model for the Tooth Friction Coefficient in Gear Transmissions: Predictive Modelling from Operating Conditions and Uncertainty Estimation

Maxence Bigerelle [1,*], Julie Lemesle [2], Eddy Chevallier [1], Yasser Diab [3], Thomas Touret [3], Christophe Changenet [3] and Fabrice Ville [4]

[1] Univ. Polytechnique Hauts-de-France, CNRS, UMR 8201 – LAMIH – Laboratoire d'Automatique de Mécanique et d'Informatique Industrielles et Humaines, F-59313 Valenciennes, France

[2] Valutec, Univ. Polytechnique Hauts-de-France, 59314 Valenciennes CEDEX 9, France

[3] LabECAM, ECAM LaSalle Campus de Lyon, Université de Lyon, 69321 Lyon, France

[4] INSA Lyon, CNRS, LaMCoS, UMR5259, 69621 Villeurbanne, France

***** Correspondence: maxence.bigerelle@uphf.fr

Abstract: Accurate modelling of the tooth friction coefficient is central to the efficiency, vibratory and durability analyses of enclosed gear drives. Physically-based models describe these contacts through a large set of coupled thermal, contact and lubrication laws whose individual parameters carry uncertainties that are difficult to propagate. In this work we introduce the HAF model, a three-parameter phenomenological description of the friction coefficient as a function of the slide-to-roll ratio (SRR). The three parameters carry a tribological meaning: h (hysteresis) governs the steepness of the sigmoidal transition, a (attrition) the slope of the plateau, and v (friction level) the overall magnitude. The model is calibrated by non-linear regression on fourteen two-disc traction curves acquired with a one-factor-at-a-time (star) design around a reference operating point (1.6 GPa, 80 °C, 20 m/s): the contact pressure (1.2, 1.6, 1.9 GPa), the injection temperature (40, 80, 100 °C) and the mean speed (10, 20, 30 m/s) are each varied in turn, for both smooth and rough discs. A dedicated residual-resampling bootstrap method (BIG) is proposed to quantify the uncertainty of the parameters; it yields near-Gaussian, weakly correlated estimates, whereas the four bootstrap schemes native to SAS produce strong singularities. The three HAF parameters are then expressed as linear functions of load, temperature, speed and roughness; the bootstrap distributions show that the large majority of the regression coefficients are significantly different from zero at the 95 % level, and the resulting closed-form model reproduces the measured friction coefficient almost perfectly ($R^2 \approx 0.99998$) with Gaussian, zero-mean residuals that satisfy the Gauss–Markov conditions. Being differentiable and equipped with bootstrap confidence intervals, the model predicts friction over the whole operating envelope and lends itself to gradient-based optimisation of the operating conditions that minimise friction — and hence power loss and surface damage.

Keywords: friction; gear; two-disc machine; phenomenological model; hysteresis; attrition; bootstrap; uncertainty; roughness

Highlights

- A three-parameter phenomenological model (HAF) predicts the tooth friction coefficient.
- Its parameters carry a tribological meaning: hysteresis, attrition and friction level.
- A residual-resampling bootstrap yields near-Gaussian, significant coefficient statistics.
- Load, temperature, speed and roughness effects on friction are statistically identified.
- The differentiable model predicts friction and optimises low-friction conditions.

Graphical Abstract

GRAPHICAL ABSTRACT

A phenomenological model for the tooth friction coefficient in gear transmissions

Three interpretable parameters · robust bootstrap uncertainty · a predictive law over the operating envelope

1 EXPERIMENTS



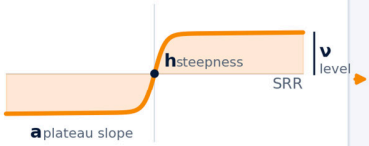
two-disc machine

rolling-sliding contact

- Load 1.2–1.9 GPa
- Temperature 40–100 °C
- Speed 10–30 m/s
- Roughness smooth / rough

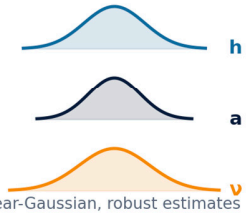
2 HAF MODEL — TRACTION CURVE

ν friction level **h** hysteresis **a** attrition



$$F(\mathrm{SRR}) = 2\nu\left(\frac{1}{1+e^{-h\cdot \mathrm{SRR}}} + a\cdot \mathrm{SRR} - 0.5\right)$$

3 BOOTSTRAP UNCERTAINTY



near-Gaussian, robust estimates

PREDICTIVE MODEL

h, a, ν = f (load, temperature, speed, roughness)

Linear laws feed the HAF equation → friction predicted across the whole operating envelope, with confidence bounds

Nomenclature

HAF friction model	
SRR	slide-to-roll ratio (–)
F(SRR)	tooth friction coefficient predicted by the model (–)
v	friction-level parameter of the HAF model (–)
h	hysteresis parameter of the HAF model (–)
a	attrition parameter of the HAF model (–)
Operating conditions	
Load	maximum Hertzian contact pressure (GPa)
Temperature	operating (bulk) temperature (°C)
Speed	mean entrainment speed (m/s)
Rough	surface-roughness state (boolean: 0 = smooth, 1 = rough)
Linear coefficient models (Section 7)	
h_i, a_i, v_i	model intercepts (–)
h_l, a_l, v_l	load coefficients (GPa^{-1})
h_t, a_t, v_t	temperature coefficients ($°C^{-1}$)
h_s, a_s, v_s	speed coefficients ($(m/s)^{-1}$)
h_r, a_r, v_r	roughness coefficients (–)
ε	residual (error) term of a linear model (–)
Statistics and bootstrap	
$\hat{h}$, $\hat{a}$, $\hat{v}$	bootstrap point estimates of h, a and v (–)
R^2	coefficient of determination of a linear model (–)
σ	bootstrap standard deviation of a coefficient (coefficient unit)
m/σ	ratio of a coefficient to its standard deviation; t-value (–)
χ^2	chi-square goodness-of-fit statistic (–)
N	number of bootstrap resamples (–)

1. Introduction

Sliding friction at the tooth flank is one of the main sources of power loss in geared transmissions and a significant contributor to vibration and noise. As environmental constraints push transmissions towards ever more severe operating conditions, the accurate prediction of the friction coefficient has become essential for efficiency, dynamic and failure analyses of mechanical drives. Friction directly conditions energy losses and the heat generated at the contact, which in turn alters lubricant properties and induces thermal expansions that affect the alignment of the gear set. Higher friction also accelerates surface wear and modulates the excitation responsible for noise and vibration.

The friction coefficient depends on numerous coupled parameters — load, speed, temperature, surface roughness and the physico-chemical properties of the solids and of the lubricant. Quiban et al. [*1*] proposed a semi-empirical model that couples an Eyring–Reynolds description of the lubricant with a stochastic representation of the rough surfaces, and calibrated it on a two-disc machine. Britton et al. [*2*] reported that superfinishing gear teeth from about 0.4 µm to 0.05 µm Ra reduces friction by roughly 30 %, while Akbarzadeh and Khonsari [*3*] showed by simulation that increasing the RMS roughness from 0.1 to 0.7 µm multiplies friction by a factor of three for Newtonian lubricants and up to ten for shear-thinning ones. These studies confirm the multifaceted, tightly coupled role of the surface and the lubricant in setting the friction coefficient, a complexity that any predictive model must contend with.

Physically-based models are flexible and informative, but they assemble a large number of contact, thermal and lubrication laws, each of which is a simplified representation carrying its own uncertainty. Propagating these uncertainties through the whole chain of equations, and guaranteeing the robustness of an inverse calibration, is therefore delicate. The drive towards higher-efficiency and electrified transmissions has renewed the need for accurate tooth-friction prediction [4,5], and data-driven and machine-learning approaches are increasingly used to the same end [6,7], although they offer little physical insight and seldom quantify uncertainty. The present paper adopts a complementary standpoint: rather than resolving the physics of the contact, it describes the measured traction curve with a compact phenomenological law — the HAF model — whose three parameters can be estimated robustly and whose uncertainties can be quantified directly. The reference model of Quiban et al. [*1*] is used throughout as a benchmark and as the source of the experimental traction curves.

2. Models for the Tooth Friction Coefficient in Gear Transmissions

2.1. Aim of the Experiment

The traction data exploited here were obtained on a two-disc machine reproducing the rolling–sliding contact of gear teeth. Smooth discs, operating under full-film lubrication, provide a reference measurement of the lubricant shear stress free of asperity interactions. Rough discs, whose roughness magnitude and orientation reproduce those of ground gear teeth, generate a representative value of the friction carried by the asperities. Combining the two surface states with a range of pressures, temperatures and speeds makes it possible to isolate the respective contributions of the fluid film and of the asperities to the overall friction coefficient.

2.2. Physically-Based Friction Model

The model of Quiban et al. [*1*], derived from the mixed-lubrication framework of Diab et al. [*8*], splits the normal load and the apparent contact area into a fluid part and an asperity part, so that the friction coefficient is written as the pressure-weighted sum of a fluid shear stress and an asperity shear stress. The lubricant is

treated as an Eyring–Reynolds fluid: the fluid shear stress derives from a Newtonian stress and a reference Eyring stress that depends on pressure and on the local contact temperature, the latter being obtained iteratively from the generated heat and a thermal resistance. The asperity contribution follows a stochastic contact description based on the spectral moments of the roughness profiles. This physically-based model requires the calibration of three Eyring parameters on smooth discs and of one asperity friction coefficient on rough discs, in addition to a large set of tabulated physical laws — a comprehensive but parameter-heavy description. More recent physically-based approaches follow the same logic, coupling multi-tooth-meshing dynamics to the friction coefficient [9] or deriving the mean tooth friction from an instantaneous local model that accounts for lubricant shear and asperity contact [10], while quantitative-EHL studies continue to refine the underlying rheology [11]. This parameter-heavy character motivates the phenomenological alternative developed below.

2.3. A New Empirical Friction Model: the HAF Model

We propose a three-parameter phenomenological model, referred to as the HAF model (Hysteresis, Attrition, Friction), that describes the measured friction coefficient as a function of the slide-to-roll ratio (SRR). The friction curve is expressed by Equation (1):

$$F(SRR) = 2v\left(\frac{1}{1+e^{-h\cdot SRR}} + a\cdot SRR - 0.5\right) \quad (1)$$

Each parameter has a distinct physical interpretation and controls a specific feature of the curve:

- ***Parameter v (friction):*** scales the whole curve and represents the overall friction level; larger v raises the friction coefficient at every SRR.
- ***Parameter h (hysteresis):*** controls the steepness of the sigmoidal transition around SRR = 0. A larger h produces a sharper rise followed by an earlier saturation, reflecting the internal friction of the material.
- ***Parameter a (attrition):*** introduces a linear trend on the plateau. A positive a increases friction with SRR (contact hardening), a negative a decreases it (contact softening), and relates to the abrasive interaction of the surfaces.

The resulting curve shows the rapid initial increase of friction with SRR governed by h, followed by a plateau modulated by the linear attrition term a, the whole being scaled by v. Figure 1 illustrates the sensitivity of the friction coefficient to the three parameters.

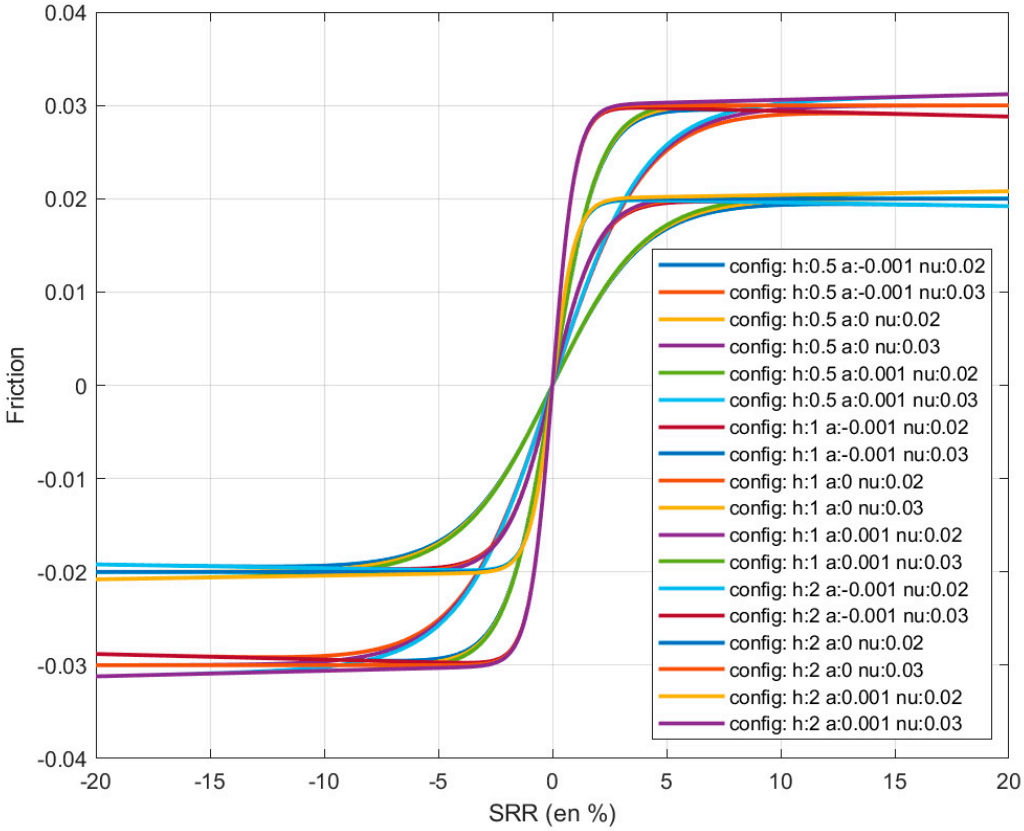


Figure 1. Simulation of the HAF model for various values of the three parameters (h, a, v). The friction coefficient is plotted against the slide-to-roll ratio SRR (%) for three values of h (0.5, 1, 2), three values of a (−0.001, 0, 0.001) and two values of v (0.02, 0.03), illustrating the sensitivity of the curve to each parameter.

2.4. On the Interest of a Phenomenological Model

The physically-based model of Quiban et al. [*1*] combines many contact, thermal and lubrication laws, each simplified and each carrying uncertainty. The three Eyring parameters are calibrated on smooth discs and the asperity friction coefficient on rough discs, so that the shape of the experimental curve is influenced by uncertainties propagating through the whole model. Ensuring the robustness of such an inverse calibration is therefore difficult. Our approach instead captures the phenomenological behaviour of the lubricated contact with three coefficients whose uncertainties are directly controllable. By calibrating these coefficients on the measured curves and quantifying their dispersion, the HAF model manages uncertainty explicitly and, in return, offers a diagnostic tool to assess the robustness of more detailed physically-based models.

3. Experimental Data

The traction curves analysed in this study were measured on the two-disc machine described in Quiban et al. [*1*], for both smooth and rough discs. The data follow a one-factor-at-a-time (star) design built around a reference operating point (1.6 GPa, 80 °C, 20 m/s): starting from that point, the maximum contact pressure (1.2, 1.6, 1.9 GPa), the oil injection temperature (40, 80, 100 °C) and the mean entrainment speed (10, 20, 30 m/s) are each varied in turn, the other two variables being held at their reference value. This gives seven

operating conditions per surface state and, with smooth and rough discs, fourteen traction curves in total. For each condition the friction coefficient was recorded as a function of the slide-to-roll ratio over the range −20 % to +20 %. Because only one factor varies at a time, this design identifies the main effects of load, temperature and speed on the HAF parameters, without estimating their interactions. Smooth discs establish a reference lubricant response under full-film lubrication, whereas rough discs reveal the asperity contribution characteristic of ground gear teeth. The high-pressure rheology of such gear oils is itself intricate and central to the traction response [12].

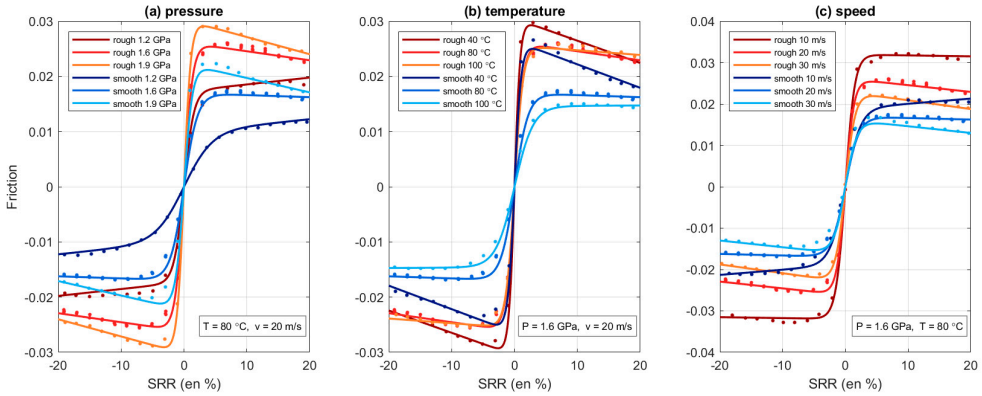


Figure 2. Friction coefficient versus slide-to-roll ratio (SRR) for rough and smooth surfaces. (a) Three contact pressures (1.2, 1.6, 1.9 GPa) at 20 m/s and 80 °C; (b) three temperatures (40, 80, 100 °C) at 20 m/s and 1.6 GPa; (c) three mean speeds (10, 20, 30 m/s) at 80 °C and 1.6 GPa. Symbols are the experimental points extracted from the reference two-disc measurements; solid lines are the HAF model fits.

4. Parameter Estimation of the HAF Model

The three HAF parameters were estimated for every operating condition by non-linear regression, using the *NLIN* procedure of the SAS system. A grid of starting values was scanned (h from 0 to 3 in steps of 0.01, a from −0.02 to 0.04 in steps of 0.0001 and v from 0 to 0.05 in steps of 0.001) to provide a broad search space, and the residual sum of squares (SSE) between measured and predicted friction was minimised by the Levenberg–Marquardt algorithm, which blends the Gauss–Newton and gradient-descent methods for robust convergence. Iterations were stopped when the change in the estimates fell below tolerance or after a maximum of 15 000 iterations.

The response surfaces of the SSE with respect to the parameter pairs (Figure 3) confirm the existence of a single, well-marked minimum for each condition, which supports the identifiability of the three parameters. Table 1 gathers the estimated values for all fourteen operating conditions (seven per surface state). The friction level v and the hysteresis h both increase with pressure and are systematically higher for rough surfaces, whereas the attrition a shifts from positive to negative values as pressure increases. The uncertainty analysis of Sections 5 and 6 is illustrated on the pressure sweep (the two surface states at the three pressures), while the linear laws of Section 7 use all fourteen curves.

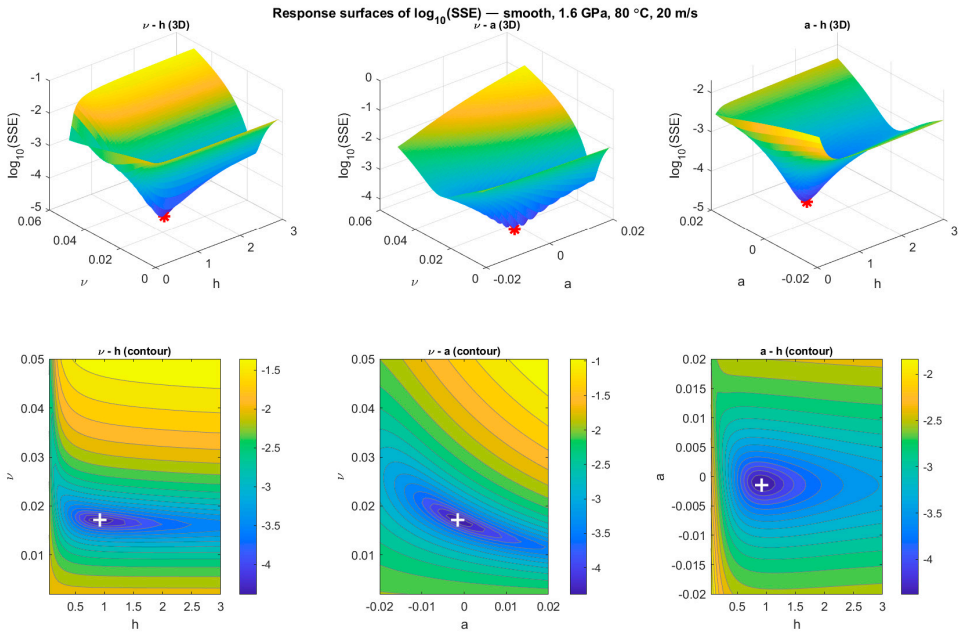


Figure 3. Response surface of $\log_{10}$(SSE) versus the v–a parameter pair for one operating condition (rough surface, 1.2 GPa, 80 °C, 20 m/s), obtained during the non-linear optimisation. The complete set of the three views (v–a, v–h, a–h) for each operating condition is given in Appendix A, Figure A1; a single, well-defined minimum is observed in every case.

Table 1. HAF parameters (h, a, v) and residual sum of squares (SSE) estimated by non-linear regression for the fourteen operating conditions of the star design (seven per surface state).

Roughness	Load (GPa)	Temp (°C)	Speed (m·s^{-1})	SSE	h	a	v
Rough	1.2	80	20	1.4×10^{-5}	1.267	0.0036	0.0175
Rough	1.6	40	20	1.3×10^{-5}	2.215	−0.0066	0.0305
Rough	1.6	80	10	1.1×10^{-5}	1.334	−0.0004	0.0319
Rough	1.6	80	20	3.2×10^{-5}	1.450	−0.0031	0.0261
Rough	1.6	80	30	0.5×10^{-5}	1.269	−0.0046	0.0230
Rough	1.6	100	20	0.9×10^{-5}	1.457	−0.0017	0.0255
Rough	1.9	80	20	0.6×10^{-5}	1.838	−0.0051	0.0302
Smooth	1.2	80	20	0.1×10^{-5}	0.443	0.0059	0.0098
Smooth	1.6	40	20	3.3×10^{-5}	1.894	−0.0081	0.0264
Smooth	1.6	80	10	2.4×10^{-5}	0.822	0.0033	0.0187
Smooth	1.6	80	20	4.1×10^{-5}	0.921	−0.0012	0.0169
Smooth	1.6	80	30	3.4×10^{-5}	1.081	−0.0050	0.0162
Smooth	1.6	100	20	1.0×10^{-5}	0.675	0.0002	0.0145
Smooth	1.9	80	20	4.7×10^{-5}	1.474	−0.0059	0.0223

5. Model Uncertainties

5.1. Bootstrapping Principle

In non-linear regression, the relationship between parameters and response is complex and the estimates can be sensitive to the data and to the assumed error distribution. Bootstrapping provides empirical estimates of parameter variability without relying on restrictive parametric assumptions [13]: by resampling the data with replacement and refitting the model many times, it generates a distribution of estimates from which confidence intervals and stability diagnostics are derived.

5.2. Four Bootstrap Methods in SAS

The *NLIN* procedure offers four residual-based bootstrap schemes. RAW resamples the raw residuals without scaling — the simplest and fastest but the least robust when the residual variance is not homogeneous. ADJSSE rescales the residuals uniformly to stabilise their variance. JAC scales them according to the Jacobian leverage, accounting for the sensitivity of the model to the parameters. TAN scales them according to the tangential leverage, i.e. the influence of observations along the response surface. Each scheme trades simplicity against robustness, and the most suitable choice must be assessed from the resulting distributions.

5.3. A New Bootstrap Method: BIG

We propose a residual-resampling bootstrap, referred to as BIG, designed to give a robust estimate of the HAF parameter uncertainties. Starting from the fitted model (Equation (1)), the residuals — differences between measured and fitted friction — are computed (Equation (2)):

$$Residual_i = F_i - 2\hat{v}\left(\frac{1}{1+e^{-\hat{h}\cdot SRR_i}} + \hat{a}\cdot SRR_i - 0.5\right) \tag{2}$$

These residuals are then resampled with replacement and added back to the fitted values to create a new data set (Equation (3)):

$$F_i^* = 2\hat{v}\left(\frac{1}{1+e^{-\hat{h}\cdot SRR_i}} + \hat{a}\cdot SRR_i - 0.5\right) + ResampledResidual_i \tag{3}$$

The model is refitted on each synthetic data set, and the operation is repeated a large number of times (typically up to 10^5 iterations). The collection of estimates (v*, h*, a*) yields the empirical distribution — and hence the uncertainty — of every parameter. Unlike the leverage-based schemes, BIG rebuilds the response before every fit, which restores the natural variability of the estimates.

5.4. Results

The parameter distributions obtained from 10^5 bootstrap samples are compared in Figure 4 for the five schemes (ADJSSE, JAC, RAW, TAN and BIG). The four SAS-native methods exhibit pronounced singularities at their mean values, indicating that the resamples frequently converge to identical estimates — a symptom of insufficient variability and of sensitivity to local minima. The BIG histograms, by contrast, are smooth and close to Gaussian, which reflects a more consistent and reliable estimation.

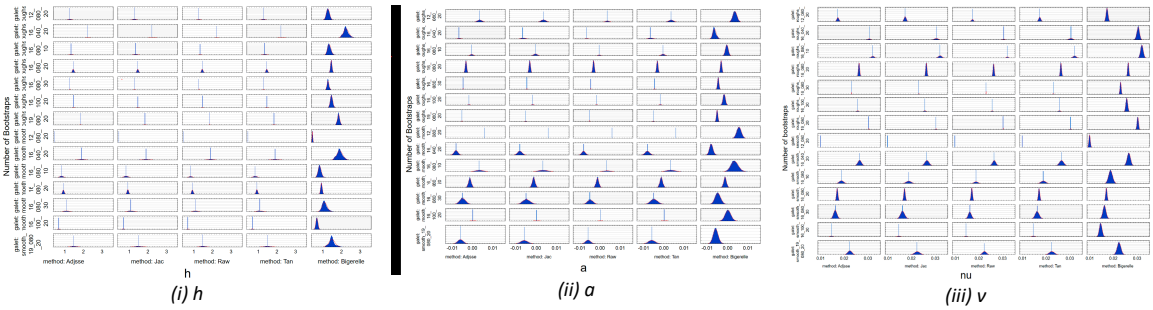


Figure 4. Histograms of 10^5 bootstrap simulations of the HAF parameters (i) h, (ii) a and (iii) v, obtained with the five bootstrap schemes (ADJSSE, JAC, RAW, TAN, BIG) for the two surface states and the three contact pressures. The BIG histograms are nearly Gaussian, whereas the four other methods show marked singularities around the mean.

To quantify these singularities, each histogram was compared with a normal distribution through a chi-squared goodness-of-fit test (Equation (4)), where O_i and E_i are the observed and expected frequencies in each bin:

$$\chi^2 = \sum_i \frac{(O_i - E_i)^2}{E_i} \tag{4}$$

The distribution of $\log_{10}(\chi^2/df)$ over the six conditions (Figure 5) confirms the diagnosis: the average χ^2 for the BIG method is of the order of 7, whereas the ADJSSE, JAC, RAW and TAN methods reach values from about 800 to 4000 — an error on the fit quality exceeding a factor of one hundred. The BIG method is therefore retained for the uncertainty analysis that follows.

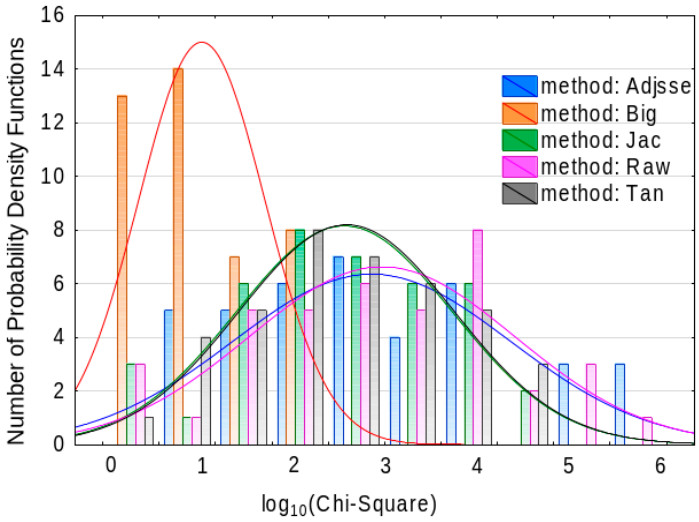


Figure 5. Distribution of $\log_{10}(\chi^2/df)$ for the five bootstrap schemes over the six conditions (two surface states × three contact pressures). Lower values indicate a closer fit to the normal distribution; the BIG method clusters at markedly lower values than the other four.

6. Coefficient Analysis

6.1. Two-Dimensional Coefficient Correlation

The bootstrap samples give access to the joint distributions of the parameter pairs. Smoothed with a bivariate kernel density estimate, they reveal clear correlations (Figure 6): a positive correlation between h and a, and negative correlations between h and v and between a and v. In tribological terms, conditions of higher hysteresis tend to coincide with a more pronounced attrition, while both a higher hysteresis and a higher attrition are associated with a lower overall friction level, suggesting a trade-off between energy-dissipation mechanisms. These interdependencies must be taken into account when interpreting the parameters, since a change in one estimate implies a compensating change in the others.

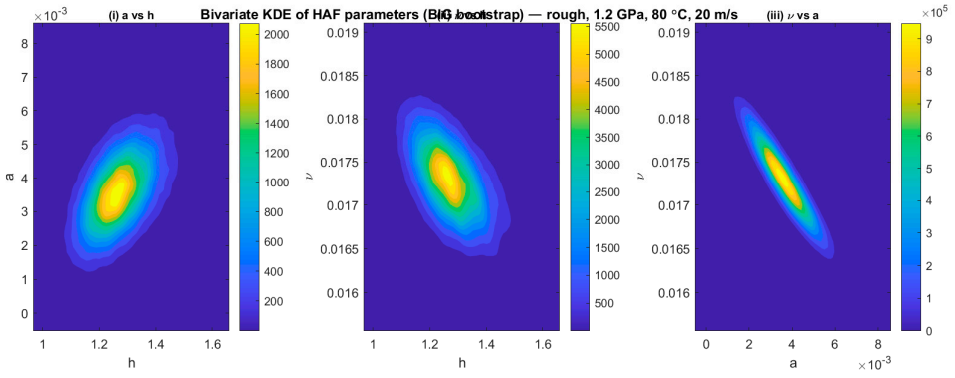


Figure 6. Bivariate kernel density plots of the HAF parameters for a representative condition (rough surface, 1.2 GPa, 80 °C, 20 m/s): (i) a versus h, (ii) v versus h and (iii) v versus a. The densities are built from the BIG bootstrap samples; the complete set for all fourteen conditions is given in Appendix A, Figure A2.

6.2. Probability Density Functions

Beyond the parameters themselves, the bootstrap allows the uncertainty of the friction curve to be visualised directly. Figure 7 maps the probability density of the resampled points in the friction–SRR plane. The density is high at the asymptotes of the curve, where the estimates are well supported, and low along the rising part of the sigmoid, which is governed by h. The scarcity of data in this steep transition zone makes the estimation of h intrinsically less reliable, a point of practical importance since h controls the sharpest part of the traction curve.

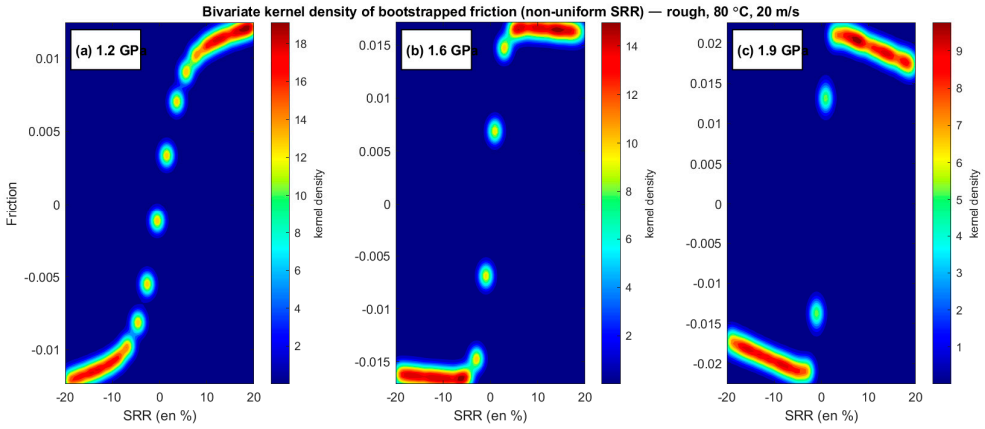


Figure 7. Probability density of the bootstrapped friction points along the friction–SRR curve (non-uniform SRR sampling), for the rough surface at (a) 1.2, (b) 1.6 and (c) 1.9 GPa (80 °C, 20 m/s). The density is concentrated at the asymptotes and thin along the rising branch of the sigmoid (complete set for both surfaces and all conditions in Appendix A, Figure A3).

Recomputing the friction from the 10^5 bootstrapped parameter sets at evenly spaced SRR values gives a continuous view of the model uncertainty (Figure 8). This representation is no longer limited to the experimental points and highlights, more clearly, the regions where the prediction is confident and those where it is dispersed — in particular the transition zone driven by h.

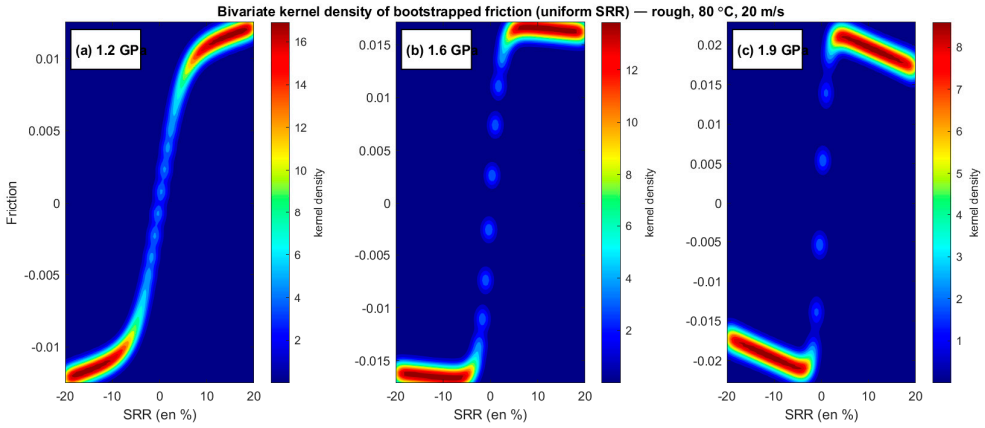


Figure 8. Probability density of the friction coefficient recomputed at evenly spaced SRR intervals from the bootstrapped parameters (uniform SRR sampling), for the rough surface at (a) 1.2, (b) 1.6 and (c) 1.9 GPa (80 °C, 20 m/s). High-density regions denote consistent predictions (complete set for both surfaces and all conditions in Appendix A, Figure A4).

6.3. One-Dimensional Coefficient Uncertainties

The marginal distributions of the three parameters are summarised as histograms and box plots for the two surface states and the three pressures (Figures 9 and 10). The hysteresis h follows the same trend as the friction level v: both increase with pressure and are higher on rough surfaces, rising for h from 1.26 to 1.83 on rough discs and from 0.44 to 1.47 on smooth discs between 1.2 and 1.9 GPa. The attrition a depends on pressure but not on roughness, changing sign from positive at 1.2 GPa to negative at 1.9 GPa (about −0.005 for both surface states). The friction level v remains higher for rough surfaces (0.017–0.030) than for smooth ones (0.010–0.022).

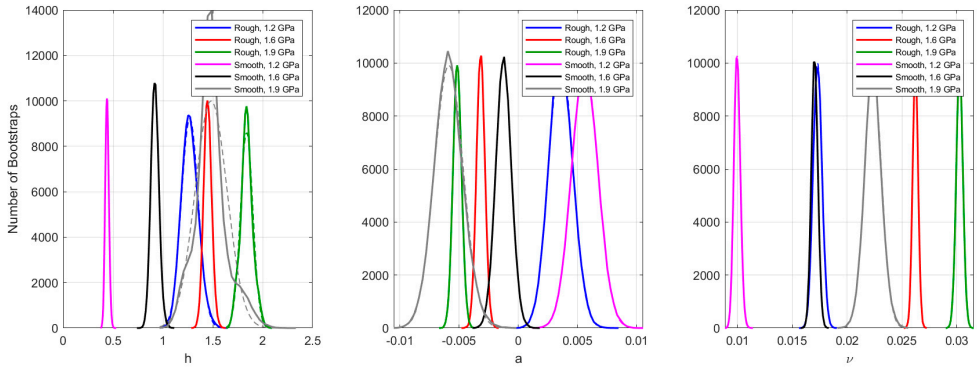


Figure 9. Histograms of the bootstrapped HAF parameters (i) v, (ii) a and (iii) h as a function of the normal load (1.2, 1.6, 1.9 GPa, at the reference temperature 80 °C and speed 20 m·s^{-1}), comparing rough and smooth surfaces; each histogram aggregates 10^5 bootstrap samples. The complete set — the three parameters as a function of load, temperature and speed — is given in Appendix A, Figure A5.

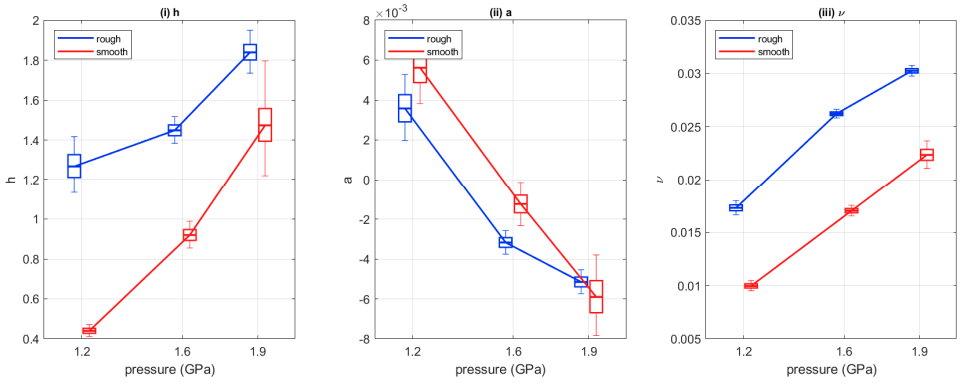


Figure 10. Box plots of the bootstrapped HAF parameters (i) v, (ii) a and (iii) h as a function of the normal load (1.2, 1.6, 1.9 GPa, at the reference temperature 80 °C and speed 20 m·s^{-1}), comparing rough and smooth surfaces. Boxes show the 5th centile, first quartile, median, third quartile and 95th centile of the 10^5 bootstrap samples; the complete set — the three parameters as a function of load, temperature and speed — is given in Appendix A, Figure A6.

7. Modelling the HAF Coefficients

7.1. Coefficient Modelling by Surface State

We first model each HAF coefficient separately for the smooth and for the rough discs, as a linear function of load, temperature and speed:

$$h = h_i + h_s \cdot Speed + h_l \cdot Load + h_t \cdot Temperature + \varepsilon_h \quad (5)$$

$$a = a_i + a_s \cdot Speed + a_l \cdot Load + a_t \cdot Temperature + \varepsilon_a \quad (6)$$

$$\nu = \nu_i + \nu_s \cdot Speed + \nu_l \cdot Load + \nu_t \cdot Temperature + \varepsilon_\eta \quad (7)$$

where h_i , a_i and ν_i are the intercepts, h_l , a_l and ν_l the load coefficients, h_t , a_t and ν_t the temperature coefficients, and h_s , a_s and ν_s the speed coefficients. Fitting these laws over the fourteen measured curves quantifies how each operating variable acts on the friction behaviour.

Table 2. Fitted coefficients of the linear models of h, a and v by surface state (load in GPa, temperature in °C, speed in m/s). In each cell: the coefficient with its bootstrap standard deviation (±) on the first line, and the ratio mean/standard deviation (m/σ) on the second. Coefficients in red are significantly different from zero at the 95 % level (|m/σ| > 1.96).

Surface	Coeff.	Intercept	Load	Temperature	Speed	R^2
Rough	*a*	**0.015** ±0.004 *m/σ = 3.8*	**−0.0129** ±0.0013 *m/σ = −9.9*	**0.000089** ±0.000026 *m/σ = 3.4*	**−0.00021** ±0.00005 *m/σ = −4.2*	0.93 ±0.024
	h	**1.496** ±0.33 *m/σ = 4.5*	**0.779** ±0.27 *m/σ = 2.9*	**−0.01471** ±0.0021 *m/σ = −7.0*	−0.00322 ±0.0079 *m/σ = −0.4*	0.76 ±0.026
	v	**0.011** ±0.0013 *m/σ = 8.5*	**0.0191** ±0.0006 *m/σ = 31.8*	−0.000090 ±0.00005 *m/σ = −1.8*	**−0.00044** ±0.0001 *m/σ = −4.4*	0.94 ±0.024
Smooth	*a*	**0.022** ±0.005 *m/σ = 4.4*	**−0.0170** ±0.0025 *m/σ = −6.8*	**0.000150** ±0.000024 *m/σ = 6.2*	**−0.00041** ±0.00014 *m/σ = −2.9*	0.97 ±0.021
	h	0.100 ±0.55 *m/σ = 0.2*	**1.455** ±0.22 *m/σ = 6.6*	**−0.02128** ±0.0034 *m/σ = −6.3*	0.01294 ±0.0083 *m/σ = 1.6*	0.97 ±0.021
	v	**0.007** ±0.0025 *m/σ = 2.8*	**0.0179** ±0.0012 *m/σ = 14.9*	**−0.000208** ±0.0001 *m/σ = −2.1*	**−0.00012** ±0.00006 *m/σ = −2.0*	0.98 ±0.018

Each law is fitted not once but on every bootstrap replicate of the three coefficients, so that every regression coefficient inherits a full distribution — and hence a standard deviation and a significance test — rather than a single value.

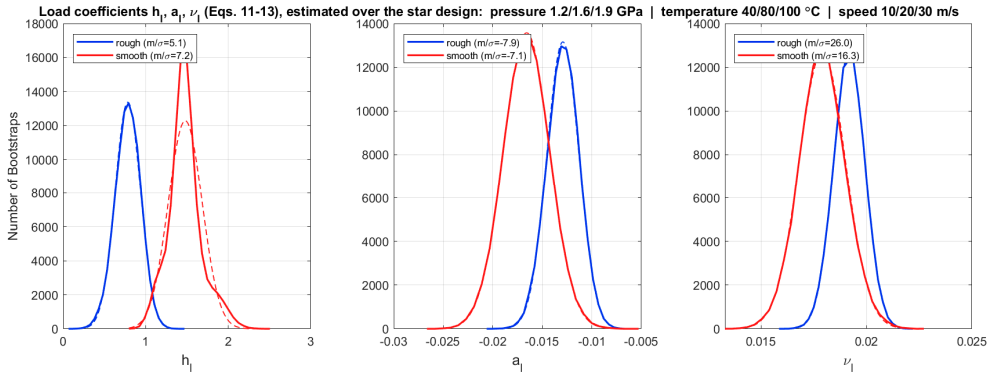


Figure 11. Representative bootstrap distributions of the linear-model coefficients: the load effect on v (left, tightly determined, m/σ ≈ 20) and the speed effect on h (right, not significant). The complete set of the twenty-four coefficient distributions is given in Appendix A, Figure A7.

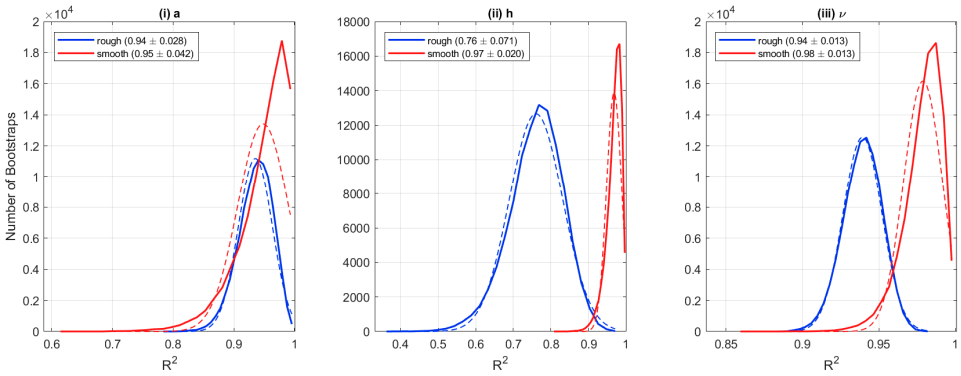


Figure 12. Bootstrap distributions of the coefficient of determination (R^2) of the linear models, for the three HAF coefficients (a, h, v) at the two roughness levels (rough, smooth). Means ± standard deviations estimated from the histograms by image analysis: a — rough 0.93 ± 0.024, smooth 0.97 ± 0.021; h — rough 0.76 ± 0.026, smooth 0.97 ± 0.021; v — rough 0.94 ± 0.024, smooth 0.98 ± 0.018.

The linear models capture the dependence of the three HAF coefficients on load, temperature and speed well: the coefficient of determination exceeds 0.93 for five of the six coefficient–surface combinations, reaching 0.98 for v on smooth surfaces. The single exception is the hysteresis parameter h on rough surfaces (R^2 = 0.76), whose fit is markedly poorer and whose regression coefficients carry the largest bootstrap uncertainties (intercept 1.496 ± 0.33, load 0.779 ± 0.27). This indicates that, for rough contacts, h is only partially described by a linear combination of the operating parameters — its behaviour is more scattered, and probably more nonlinear, than that of a and v.

The signs and magnitudes of the coefficients are physically consistent. Load exerts the strongest and most systematic influence on h (positive, 0.779 for rough and 1.455 for smooth surfaces), so the hysteresis contribution grows with contact pressure, whereas temperature acts in the opposite direction (negative, −0.0147 and −0.0213), in line with the thinning of the lubricant film and the reduction of viscous hysteresis as temperature rises. The friction level v increases moderately with load (about 0.019) and decreases slightly with temperature and speed, while the attrition parameter a shows only weak dependencies on all three variables, with coefficients close to zero.

The bootstrap standard deviations quantify how firmly each dependency is established. Relative to their values, the coefficients of v are the most tightly determined (for instance load 0.0191 ± 0.0006, i.e. about 3 %), making the friction level the most robustly predictable of the three parameters, whereas those of h on rough surfaces are the least. The intercepts also reveal a pronounced baseline shift between surface states — most strikingly for h (1.496 rough versus 0.100 smooth), but also for a and v — which shows that surface roughness does not merely add scatter but changes the very level of the coefficients. This observation motivates the generalized model of Section 7.2, where roughness is introduced explicitly as an additional variable rather than handled through two separate fits.

A further advantage of the bootstrap is that it provides a direct significance test for every coefficient. Because the resampling yields the full sampling distribution of each coefficient, a coefficient can be declared significantly different from zero at the 95 % level when zero lies outside its 95 % bootstrap interval; given the near-Gaussian shape of these distributions (Sections 5 and 6), this is equivalent to its absolute value exceeding about 1.96 times its standard deviation. Applying this criterion (coefficients shown in red in Table 2), twenty of the twenty-four coefficients are significant. The four exceptions are the effect of speed on h for both surface states, the intercept of h on smooth surfaces, and the effect of temperature on v for rough surfaces. The non-

significance of the speed terms of h indicates that, over the range tested, the hysteresis parameter is governed essentially by load and temperature — that is, by film thickness and lubricant viscosity — rather than by the entrainment speed; the smooth-surface intercept of h is not resolved simply because smooth-surface hysteresis is very small (about 0.1) and correspondingly ill-constrained. That almost every coefficient is significant, together with the high coefficients of determination and the low, near-Gaussian and weakly correlated uncertainties, shows that the dependence of the three HAF parameters on the operating conditions is firmly established rather than an artefact of fitting. This robustness is a direct benefit of the compact three-parameter form: because the three parameters are physically meaningful and largely independent, the effects of load, temperature, speed and roughness on friction can be identified with confidence — which a heavily over-parameterized model could not achieve. The two near-threshold cases (the temperature and speed effects on v for smooth surfaces) should nonetheless be read with some caution, since the standard deviations are themselves estimated from the histograms.

7.2. Coefficient Modelling Including Roughness

We now pool the two data sets and introduce the surface state as a binary variable (Rough = 1 for rough discs, 0 for smooth), so that a single set of laws describes both surfaces:

$$h = h_i + h_s \cdot Speed + h_l \cdot Load + h_t \cdot Temperature + h_r \cdot Rough + \varepsilon_h \quad (8)$$

$$a = a_i + a_s \cdot Speed + a_l \cdot Load + a_t \cdot Temperature + a_r \cdot Rough + \varepsilon_a \quad (9)$$

$$v = v_i + v_s \cdot Speed + v_l \cdot Load + v_t \cdot Temperature + v_r \cdot Rough + \varepsilon_\eta \quad (10)$$

where h_r , a_r and v_r are the roughness coefficients, the intercepts and the load, temperature and speed coefficients keeping the meaning defined above. As before, every coefficient is obtained on the bootstrap replicates, which yields its uncertainty and its significance directly.

Table 3. Fitted coefficients of the generalized linear models including roughness (Rough = 1, Smooth = 0). In each cell: the coefficient with its bootstrap standard deviation (±), then the ratio mean/standard deviation (m/σ). Coefficients in red are significantly different from zero at the 95 % level (|m/σ| > 1.96).

Coeff.	Intercept	Load	Temperature	Speed	Rough	R^2
a	**0.0193** ±0.0029 *m/σ = 6.7*	**−0.015** ±0.0015 *m/σ = −10.0*	**0.00011** ±0.000015 *m/σ = 7.3*	**−0.00031** ±0.00006 *m/σ = −5.2*	**−0.0012** ±0.00049 *m/σ = −2.4*	0.921 ±0.035
h	0.5445 ±0.28 *m/σ = 1.9*	**1.117** ±0.13 *m/σ = 8.6*	**−0.01799** ±0.0022 *m/σ = −8.2*	0.00486 ±0.0049 *m/σ = 1.0*	**0.5088** ±0.045 *m/σ = 11.3*	0.899 ±0.030
v	**0.0056** ±0.0014 *m/σ = 4.0*	**0.018** ±0.0007 *m/σ = 25.7*	**−0.00014** ±0.00001 *m/σ = −14.0*	**−0.00028** ±0.00003 *m/σ = −9.3*	**0.0086** ±0.00026 *m/σ = 33.1*	0.945 ±0.010

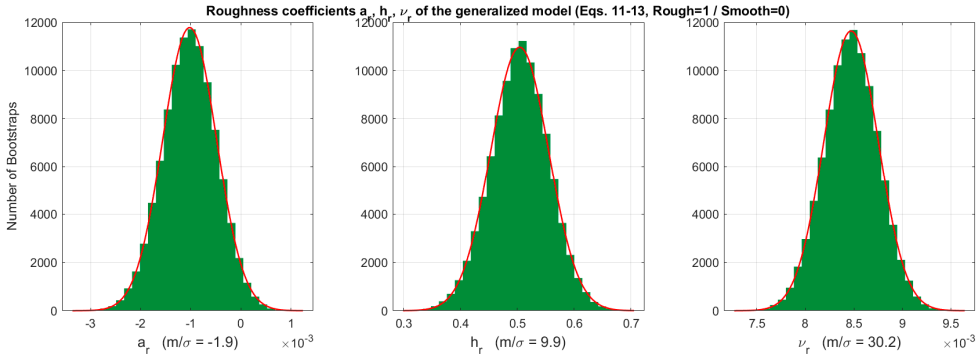


Figure 13. Bootstrap distributions of the roughness coefficient for (i) a, (ii) h and (iii) v — the effect introduced in the generalized model (Section 7.2), highly significant for the three parameters. The complete set of all coefficients (and the associated R^2) is given in Appendix A, Figure A8.

The generalized model, which pools the rough and smooth data and introduces roughness as a single binary variable, confirms the trends identified in Section 7.1. The signs of the load, temperature and speed coefficients are unchanged: load increases the hysteresis h and the friction level v and slightly decreases the attrition a, while temperature lowers both h and v. Above all, the roughness term is highly significant for the three parameters — most strongly for h (0.5088, m/σ = 11.3) and v (0.0086, m/σ = 33.1), and more weakly but still significantly for a (−0.0012, m/σ = −2.4). Roughness therefore raises the hysteresis and the friction level and slightly reduces the attrition, and this effect is established with a very high signal-to-noise ratio: it is a first-order contribution, not a secondary correction.

Compared with the two separate fits of Section 7.1, this single model is more parsimonious yet at least as robust. Only two of its fifteen coefficients fail the 95 % significance test (the intercept and the speed effect of h), against four for the separate models, and the significant coefficients reach very high m/σ values (up to 33.1 for the roughness term of v). As expected, the coefficients of determination are slightly lower for a and v (0.921 and 0.945) than the best separate fits, since a single model with fewer parameters now describes both surface states — the natural price of a reduced number of regressions. For h, however, the pooled model is markedly better (R^2 = 0.899 against 0.76 for rough surfaces in Section 7.1): describing the two surface states jointly stabilizes the otherwise poorly constrained hysteresis fit. The bootstrap distributions of R^2 themselves (last column of Figure 13) are narrow — 0.921 ± 0.035, 0.899 ± 0.030 and 0.945 ± 0.010 — which shows that the quality of the fits is itself a stable, well-determined quantity. Overall, introducing roughness explicitly costs very little in fit quality while gaining in parsimony, in robustness for the hysteresis parameter, and in a direct, statistically firm quantification of the roughness effect.

7.3. The Complete Friction Model

Because the three linear laws are well determined, they can be substituted back into the HAF form. Replacing the three coefficients in Equation (1) by their expressions in the operating conditions gives:

$$h = h_i + h_s \cdot Speed + h_l \cdot Load + h_t \cdot Temperature + h_r \cdot Rough + \varepsilon_h \quad (11)$$

$$a = a_i + a_s \cdot Speed + a_l \cdot Load + a_t \cdot Temperature + a_r \cdot Rough + \varepsilon_a \quad (12)$$

$$v = v_i + v_s \cdot Speed + v_l \cdot Load + v_t \cdot Temperature + v_r \cdot Rough + \varepsilon_\eta \quad (13)$$

which, written out in full, is a single closed-form model of the friction coefficient as a function of load, temperature, speed and surface state:

$$Friction(SRR) = 2v\left(\frac{1}{1+e^{-h\cdot SRR}} + a\cdot SRR - 0.5\right) \quad (14)$$

Table 4. Coefficients of the complete non-linear predictive model (linear laws of h, a and v substituted into the HAF equation). In each cell: the coefficient with its bootstrap standard deviation (±), then the ratio mean/standard deviation (m/σ). Coefficients in red are significantly different from zero at the 95 % level (|m/σ| > 1.96).

Coeff.	Intercept (i)	Load (p)	Temperature (t)	Speed (s)	Roughness (r)
a	**0.01965** ±0.0037 *m/σ = 5.3*	**−0.01520** ±0.0019 *m/σ = −8.0*	**0.0001165** ±0.000022 *m/σ = 5.3*	**−0.0003437** ±0.00007 *m/σ = −4.9*	0.0002995 ±0.0007 *m/σ = 0.4*
h	0.1126 ±0.36 *m/σ = 0.3*	**1.1015** ±0.17 *m/σ = 6.5*	**−0.01659** ±0.0024 *m/σ = −6.9*	**0.01879** ±0.0072 *m/σ = 2.6*	**0.6765** ±0.069 *m/σ = 9.8*
v	**0.003961** ±0.0020 *m/σ = 2.0*	**0.01964** ±0.0010 *m/σ = 19.6*	**−0.0001476** ±0.000014 *m/σ = −10.5*	**−0.0002829** ±0.000043 *m/σ = −6.6*	**0.007994** ±0.0004 *m/σ = 20.0*

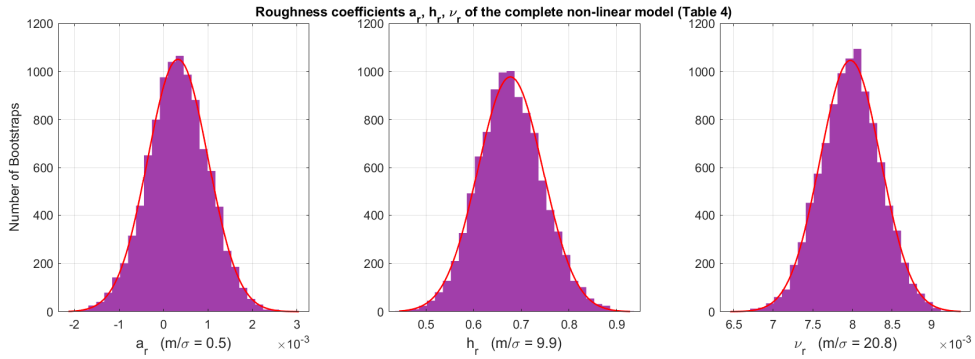


Figure 14. Bootstrap distributions of the complete-model roughness coefficient for (i) a, (ii) h and (iii) v — the roughness effect in the complete predictive model (Section 7.3). The complete set of the fifteen coefficient distributions is given in Appendix A, Figure A9.

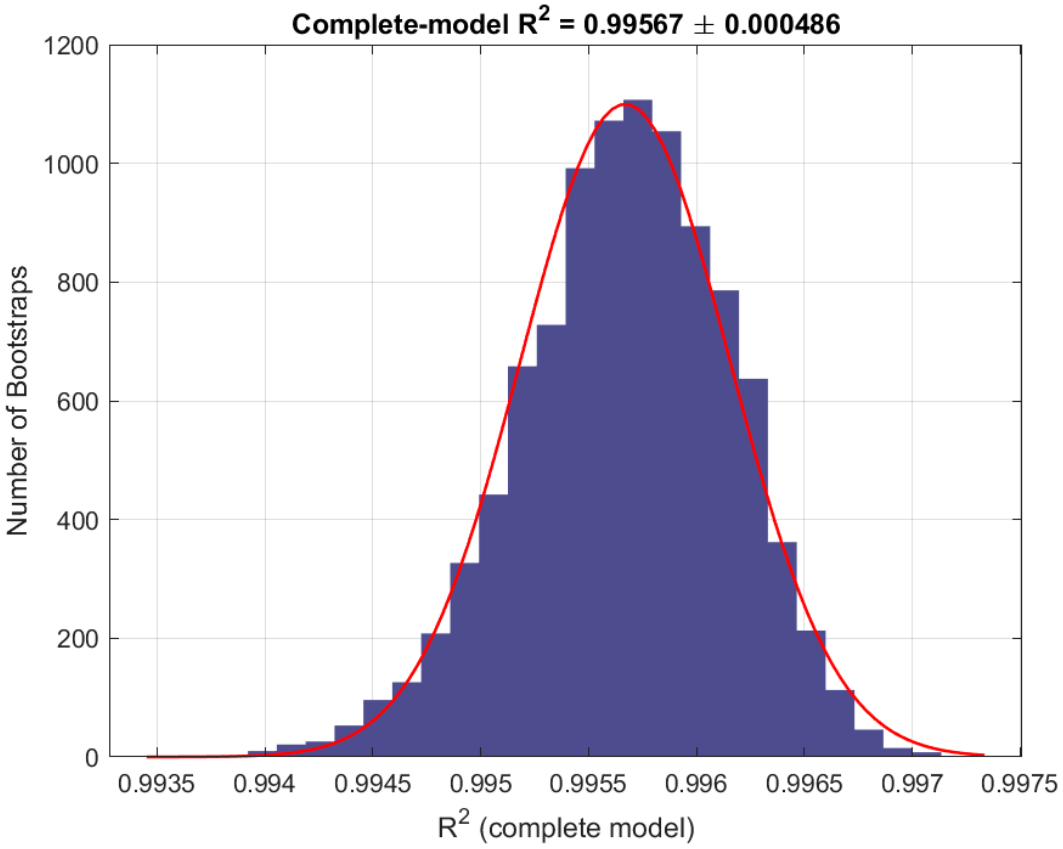


Figure 15. Bootstrap distribution of the coefficient of determination (R^2) of the complete non-linear predictive model. R^2 = 0.99998 ± 0.000003 (mean ± standard deviation over the bootstrap samples): the single combined equation reproduces the friction coefficient almost perfectly across all operating conditions.

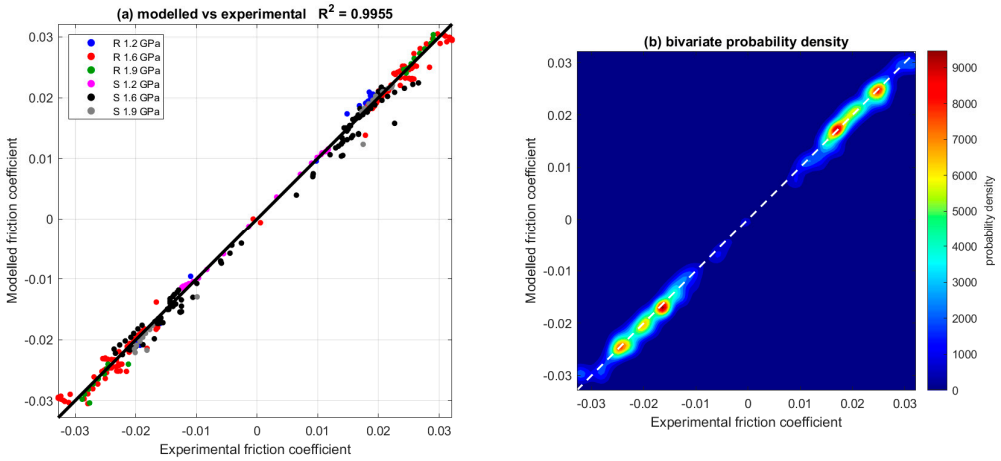


Figure 16. Modelled versus experimental tooth friction coefficient for the six operating classes (rough and smooth surfaces at 1.2, 1.6 and 1.9 GPa contact pressure). The points align closely with the identity line, showing that the complete model predicts the friction coefficient accurately once the roughness and contact-pressure effects are included. Inset: probability density of the

modelled friction coefficient; the slight central trough separates the lower-friction and higher-friction populations of operating conditions.

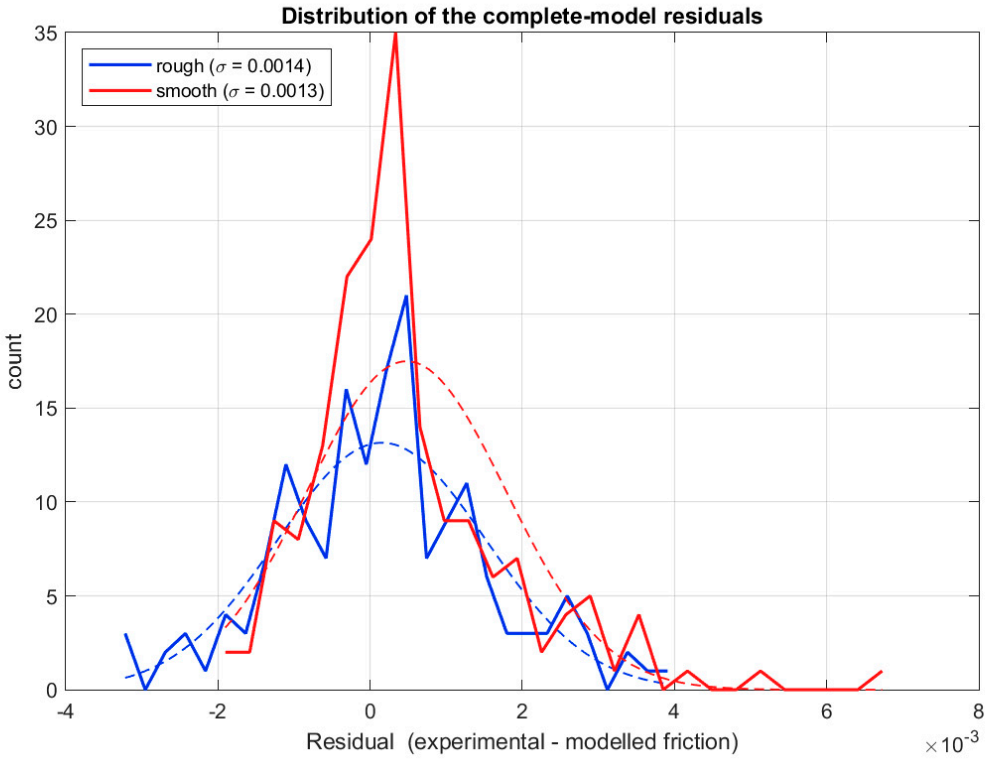


Figure 17. Distribution of the model residuals (experimental minus modelled friction coefficient) for rough and smooth surfaces. Both distributions are near-Gaussian and centred on zero — a property of the least-squares fit — with nearly equal standard deviations (σ ≈ 0.0011 and 0.0013 for the two surface states), i.e. of the order of ±0.001 in friction-coefficient units. Gaussian, zero-mean and homoscedastic residuals satisfy the Gauss–Markov assumptions of a well-specified regression.

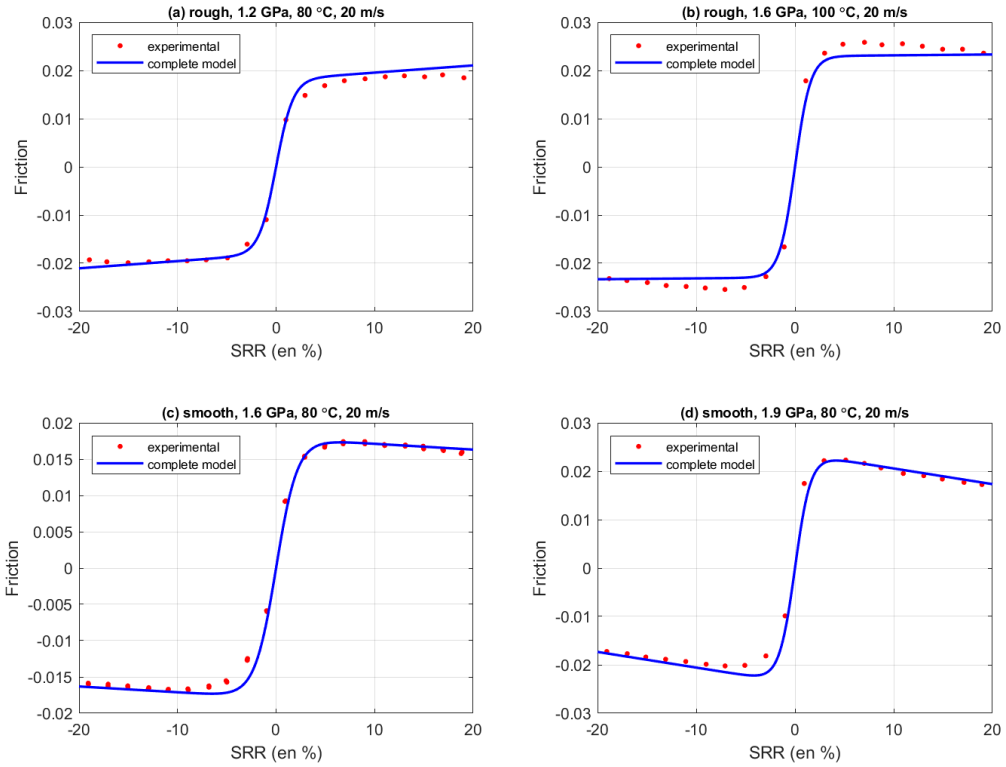


Figure 18. Experimental friction curves (points) and their reconstruction by the complete model (lines) for four representative operating conditions — (a) rough, 1.2 GPa, 80 °C, 20 m·s^{-1}; (b) rough, 1.6 GPa, 100 °C, 20 m·s^{-1}; (c) smooth, 1.6 GPa, 80 °C, 20 m·s^{-1}; (d) smooth, 1.9 GPa, 80 °C, 20 m·s^{-1} — chosen to span the range of observed shapes, from steep, near-symmetric sigmoids to flatter, markedly asymmetric curves. The complete set for all operating conditions is given in Appendix A, Figure A10.

Substituting the linear laws of h, a and v into the HAF equation yields a single closed-form expression that predicts the friction coefficient directly from the operating conditions and the surface state. The quality of this complete model is remarkable: its coefficient of determination reaches $R^2 = 0.99998 \pm 0.000003$ (Figure 15), and the modelled friction coefficient plotted against the experimental one (Figure 16) falls almost exactly on the identity line for all six operating classes (rough and smooth surfaces at 1.2, 1.6 and 1.9 GPa). Because the friction coefficient is the quantity of primary engineering interest in tribology, this near-perfect agreement — obtained while explicitly incorporating the two first-order effects, roughness and contact pressure — is a strong demonstration that the compact three-parameter HAF form captures the physics of tooth friction.

The residuals of the complete model (Figure 17) confirm the quality of the regression. For both surface states the residual distribution is near-Gaussian and centred on zero — a direct consequence of the least-squares criterion — with almost identical spreads ($\sigma \approx 0.001$ in friction-coefficient units). This residual spread is in fact a more informative measure of accuracy than the coefficient of determination, whose near-unit value partly reflects the wide range of friction values (0.006 to 0.045) over which it is computed. Gaussian, zero-mean and homoscedastic residuals are precisely the conditions under which the Gauss–Markov theorem guarantees that the least-squares estimates are the best linear unbiased estimators; their fulfilment here indicates that the model is well specified and that essentially no systematic structure remains in the data unexplained by the three parameters.

Figure 18 shows the measured traction curves together with their reconstruction by the complete model over the whole set of operating conditions. The reconstruction is excellent whatever the shape of the curve — steep or gradual, symmetric or markedly asymmetric — which is itself notable: a single three-parameter form accommodates the full variety of friction behaviours observed across pressures and surface states. Consistently with Sections 7.1 and 7.2, almost all of the fifteen coefficients of the complete model are significant at the 95 % level (Table 4); the only clear exceptions are the intercept of h and the roughness effect on a (with the intercept of v at the borderline), again indicating that the hysteresis offset and the weak roughness–attrition coupling are the least-constrained terms.

8. Prediction and Optimisation

Once the complete model has been established and validated (Section 7), it can be used as a predictive tool. A key advantage of the bootstrap is that it delivers not only point predictions but also confidence intervals on the predicted friction coefficient: propagating the resampled coefficient sets through the model equation yields, for any operating condition, a full distribution of predicted friction rather than a single value. This section exploits that capability in two phases — first to quantify the uncertainty of the prediction over the whole operating envelope, then to use the model to explore operating conditions and to identify those that minimize friction.

The engineering motivation is direct: the tooth friction coefficient is the main lever on both the efficiency of the transmission and the surface damage (scuffing, wear) of the teeth. Being able to predict friction — with quantified confidence — for arbitrary combinations of load, temperature, speed and surface state therefore opens the way to selecting operating conditions that reduce friction, and hence power loss and damage.

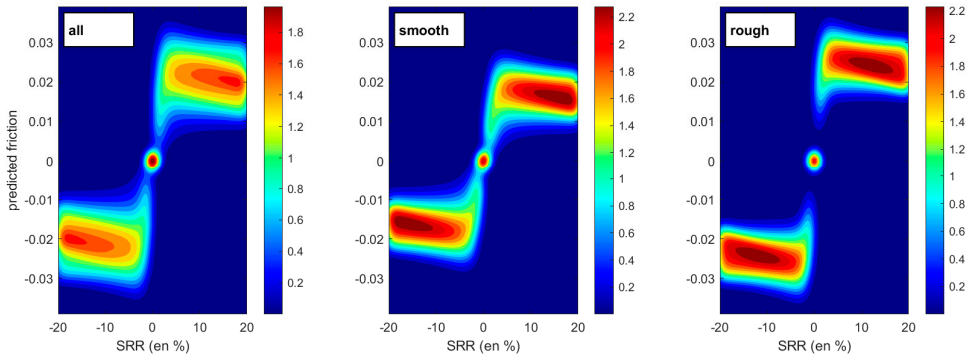


Figure 19. Bootstrap distribution (probability density) of the friction coefficient predicted by the complete model over the whole operating envelope: rough and smooth surfaces together, smooth surfaces only, and rough surfaces only. The spread of each density is the confidence interval of the prediction.

Figure 19 shows the density of the predicted friction coefficient obtained when the bootstrap coefficient sets are propagated through the model across the entire operating envelope. Rather than a single predicted value, the model returns a distribution whose width is the prediction confidence interval — this is what makes the model genuinely predictive, and not merely descriptive. Separating the surface states shows that rough surfaces shift the prediction towards higher friction and that the two populations only partly overlap, consistent with the strong, significant roughness terms of Section 7.2.

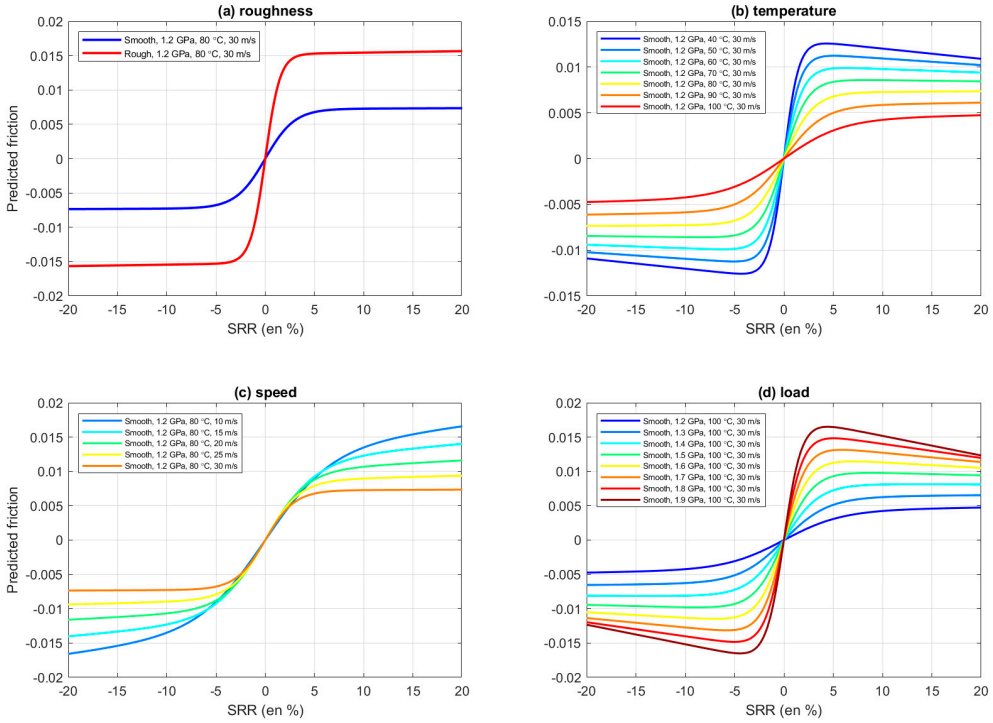


Figure 20. Predicted friction curves obtained by varying the operating parameters (here the entrainment speed, at the reference contact pressure of 1.6 GPa and temperature of 80 °C) for smooth surfaces. Because the model is continuous in load, temperature, speed and roughness, it generates a friction curve for any combination of conditions, including ones lying outside the experimental grid.

Because the complete model is a continuous, closed-form function of the operating parameters, it can generate a friction curve for any combination of load, temperature, speed and surface state — not only at the measured points but anywhere within, and reasonably beyond, the operating envelope. Figure 20 illustrates this by sweeping one parameter at a time: each curve corresponds to a different operating condition, and the family of curves maps how the friction behaviour evolves as the conditions change. This is the predictive, extrapolative use of the model: it turns a set of discrete measurements into a continuous design surface.

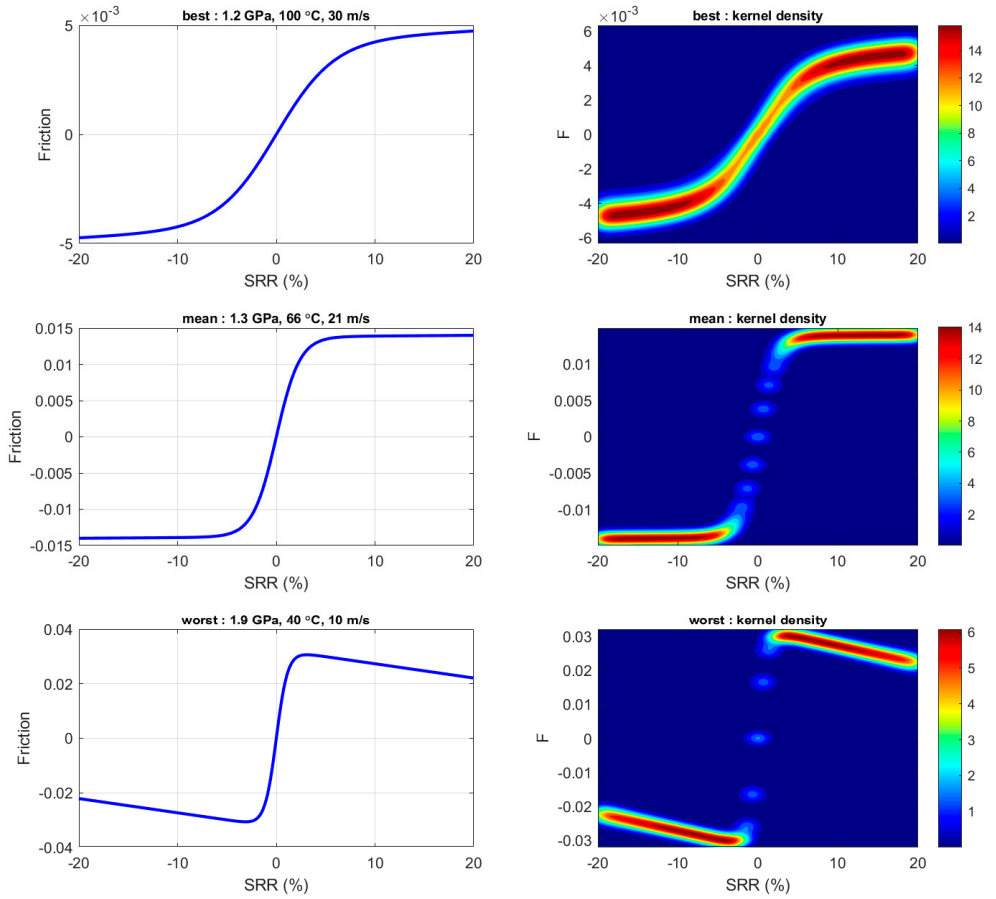


Figure 21. Predicted friction for the best, mean and worst operating conditions identified from the model (smooth surfaces): the best case (1.2 GPa, 100 °C, 30 m·s^{-1}) gives the lowest friction, the worst case (1.9 GPa, 40 °C, 10 m·s^{-1}) the highest, and the mean case (1.3 GPa, 66 °C, 21 m·s^{-1}) is the centroid of the tested operating envelope.

Scanning the operating space with the model makes it possible to single out the conditions that minimize or maximize friction. Figure 21 contrasts the best, mean and worst cases. The difference is striking: the best condition (smooth surface, low load of 1.2 GPa, high speed of 30 m/s and high temperature of 100 °C) yields a friction coefficient of the order of 0.006, whereas the worst condition (smooth surface, high load of 1.9 GPa, low speed of 10 m/s and low temperature of 40 °C) reaches about 0.045 — almost an order of magnitude higher. Low load combined with high temperature and high speed therefore drives friction down, in agreement with the coefficient signs of Section 7: friction grows with contact pressure and falls as temperature, and to a lesser extent speed, increases.

More generally, because the model is a smooth and differentiable expression of the operating parameters, its gradient with respect to load, temperature and speed can be obtained analytically. Standard gradient-descent (or quasi-Newton) optimization can then be applied to locate, within the admissible operating envelope, the conditions that minimize the friction coefficient; and, since the bootstrap provides the prediction uncertainty, the search can be carried out on a conservative upper bound of the friction rather than on its point estimate

alone. In practice this turns the model into a design tool: it identifies the loads, speeds and temperatures that lower tooth friction — and, through it, power loss and surface damage — without further testing.

9. Discussion

The prediction of the tooth friction coefficient has traditionally been approached along two lines. The first is physically based: elastohydrodynamic (EHL) models resolve the lubricant film and the shear stress in the contact, from which the friction coefficient is derived [8,14]; in gear practice these are often condensed into regression formulae fitted to large sets of EHL computations, as in the widely used model of Xu and Kahraman [15], the partial-EHL model of Arana et al. [16], or recent multi-tooth tribo-dynamic and local-to-mean friction models [10,9]. The second line is empirical: closed-form expressions relating the mean friction coefficient to load, sliding velocity, viscosity and roughness, from the classical laws of Benedict and Kelley [17] and Kelley and Lemanski [18] to the modified-Hersey formula of Fernandes et al. [19]. The phenomenological HAF model examined here, which extends the semi-empirical approach of Quiban et al. [1], belongs to neither category exactly: it imposes the shape of the traction curve through three interpretable parameters and then lets the operating conditions act on those parameters.

Imposing the sigmoidal shape is not arbitrary curve-fitting. The rheology of an EHL contact produces a traction curve that rises quasi-linearly at low slide-to-roll ratio (Newtonian regime), then shear-thins, and finally saturates at a limiting shear stress [20,14]; it is that limiting shear stress, and its dependence on pressure and temperature, that sets the maximum traction. The three HAF parameters map directly onto these features: h governs the steepness of the transition (the hysteresis of the rolling–sliding contact), a the residual slope of the plateau (attrition), and v the amplitude (the overall friction level). The phenomenological form therefore encodes, compactly, the qualitative physics that full EHL models compute in detail.

The principal advantage of this approach is statistical identifiability. Physically based models require a large number of uncertain inputs — lubricant rheology, film thickness, thermal properties, roughness spectra — and they are ultimately calibrated on the very traction curves they aim to reproduce [8,14]. It has recently been shown that a traction curve does not contain enough information to recover the underlying rheological parameters uniquely: markedly different parameter sets reproduce the same curve within experimental error, and the extracted values are system-dependent [21,22]. This is the signature of an ill-posed inverse problem, of the kind described more generally as a “sloppy” model, in which many combinations of parameters are indistinguishable from the data [23,24]. Fixing the functional form and reducing the description to three parameters sidesteps this degeneracy: the bootstrap distributions obtained here are near-Gaussian, weakly correlated and, for the large majority of coefficients, significantly different from zero (Tables 2–4). The three HAF parameters are thus identifiable, whereas the many parameters of a full physical model, in general, are not.

The bootstrap is central to this demonstration. By resampling the residuals and refitting the model, it provides distribution-free estimates of the coefficient uncertainty [13] without assuming normal errors or linearising the model. Beyond confidence intervals, it underpins the significance testing used throughout Section 7 and the residual diagnostics of the complete model: the residuals are Gaussian, zero-mean and homoscedastic, satisfying the Gauss–Markov conditions of a well-specified regression. Such an uncertainty budget is rarely reported for gear-friction models, which are usually presented as point formulae; here it is precisely what allows the model to be turned into a genuinely predictive tool, complete with confidence intervals on the predicted friction.

The analysis confirms that surface roughness and contact pressure are first-order effects on tooth friction, in line with earlier experimental evidence [2,3] and with recent studies relating roughness — and its orientation — to the friction coefficient [25,26,27]. When roughness is introduced explicitly (Section 7.2) its coefficient is highly significant for all three parameters, and the pooled model even improves the description of the hysteresis parameter relative to separate fits. Load increases both the hysteresis and the friction level, whereas temperature lowers them — consistent with the thinning of the film and the reduction of the limiting shear stress as temperature rises [14]. The speed dependence, by contrast, is weak and often not significant, which is coherent with the hysteresis being governed primarily by pressure and temperature over the range tested.

Because friction is the dominant source of load-dependent power loss in gears and a driver of surface damage such as scuffing and wear [28,29,30], a predictive and differentiable friction law has direct engineering value. The complete model reproduces the measured friction coefficient almost perfectly ($R^2 \approx 0.99998$) and, being a closed-form differentiable function of load, temperature and speed, lends itself to gradient-based optimisation of the operating conditions. Combined with the bootstrap prediction intervals, this makes it possible to search for the conditions that minimise friction — and hence power loss and damage — while accounting for the uncertainty of the prediction, in the spirit of gearbox-efficiency optimisation studies, increasingly relevant for electrified transmissions [31,32,5].

It is useful to situate the model between two extremes. Fully physical EHL models are the most detailed but, as discussed, are hard to identify and heavy to run; purely data-driven surrogates, such as the neural-network and data-driven friction models now appearing in the literature [6,7,33], can be accurate but are opaque and give no physical reading of their parameters. The HAF model occupies a useful middle ground: it attains a near-perfect fit while retaining three parameters that each carry a clear tribological meaning.

Several limitations should be kept in mind. The coefficients are specific to a given lubricant–material pair — the friction levels measured here differ substantially from those obtained by Diab et al. on a different oil [8] — so the calibration is not universal and must be repeated for other systems. The linear laws relating the parameters to the operating variables are local approximations, valid within the tested envelope; extrapolation far beyond it should be treated with caution. Roughness has been described here only through a binary state (smooth/rough); relating the HAF parameters to quantitative roughness descriptors is a natural extension. Finally, the coefficient uncertainties reported in the tables were, for the present manuscript, estimated from the bootstrap histograms and should be regarded as close approximations rather than exact figures.

These limitations also outline the way forward. Because the three parameters are robust and identifiable, they can serve as reliable targets against which physically based or numerical models are tested: rather than calibrating a physical model directly on a traction curve — an ill-posed task [21] — one can ask which physical ingredients reproduce the measured h, a and v and their dependence on the operating conditions. Establishing that link, together with the use of real roughness descriptors, is the subject of ongoing work.

10. Conclusion

This work has examined a three-parameter phenomenological model (HAF) of the tooth friction coefficient, whose parameters carry an explicit tribological meaning: the hysteresis h, the attrition a and the friction level v. A residual-resampling bootstrap (BIG) was used to quantify the uncertainty of the coefficients, and it yielded near-Gaussian, weakly correlated distributions — the statistical signature of a well-conditioned, identifiable model.

The dependence of the three parameters on load, temperature, speed and surface roughness was described by simple linear laws. The large majority of the resulting coefficients are significantly different from zero at the 95 % level, and the coefficients of determination are high; introducing roughness explicitly, in a single combined model, both quantified its effect with strong statistical significance and improved the description of the hysteresis parameter. Substituting these linear laws into the HAF equation produced a complete, closed-form predictive model that reproduces the measured friction coefficient almost perfectly ($R^2 \approx 0.99998$), with Gaussian, zero-mean and homoscedastic residuals that satisfy the Gauss–Markov conditions of a sound regression.

Because the complete model is differentiable and its predictions come with bootstrap confidence intervals, it can be used to predict friction over the whole operating envelope and, through gradient-based optimisation, to identify the operating conditions that minimise friction — and hence power loss and surface damage. The compactness and identifiability of the three-parameter form are its principal strengths: unlike heavily parameterised physical models, whose parameters cannot in general be recovered uniquely from a traction curve, the HAF parameters are robustly and interpretably determined.

Two main perspectives follow from this study. The first is to replace the binary smooth/rough description by a quantitative characterisation of the surface topography. A preliminary study, to be reported in a forthcoming paper, already shows that introducing measured roughness parameters into the same modelling framework yields very good results, and should reveal which roughness descriptors — and at which scales — govern the three HAF parameters.

The second, more fundamental, perspective is to use physically based (EHL) simulation to clarify how the underlying physical ingredients act on h, a and ν. Rather than calibrating a physical model directly on the traction curves — an ill-posed and poorly identifiable task [21] — the robust, identifiable HAF parameters can serve as targets that a physical or numerical model must reproduce. This inverts the usual procedure and offers a principled way to assess the statistical robustness and the physical significance of the coefficients, and ultimately to bridge the phenomenological and physically based descriptions of tooth friction.

Author Contributions: Methodology, M.B.; Software, M.B.; Validation, F.V. and C.C.; Formal Analysis, M.B.; Investigation, M.B., J.L., E.C., Y.D., T.T., C.C. and F.V.; Resources, Y.D. and T.T.; Writing – Original Draft Preparation, M.B. and J.L.; Writing – Review & Editing, M.B., J.L. and F.V.; Visualization, J.L.; Supervision, M.B. All authors have read and agreed to the published version of the manuscript.

Funding: This research received no external funding.

Institutional Review Board Statement: Not applicable.

Informed Consent Statement: Not applicable.

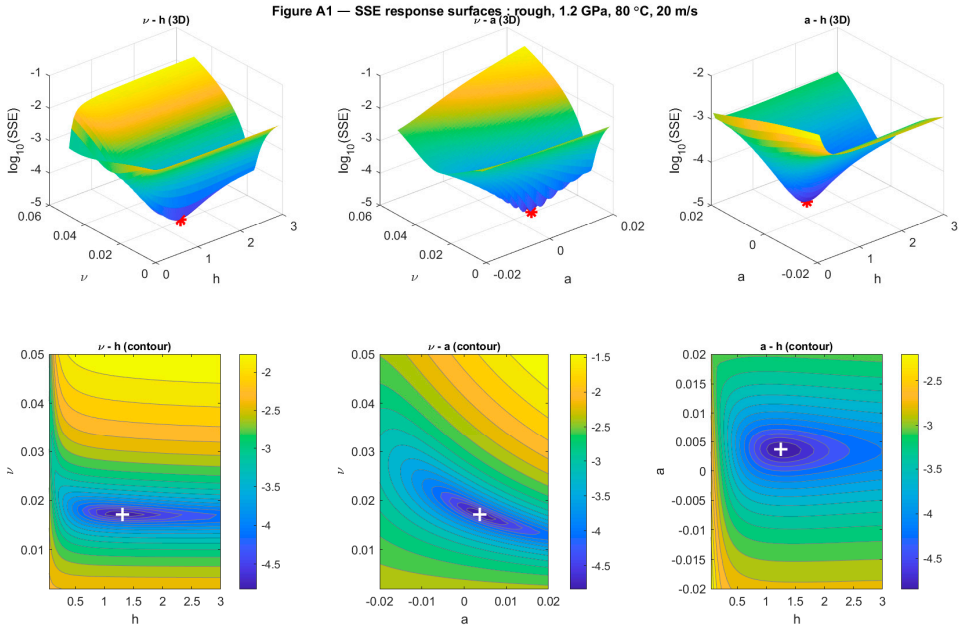
Data Availability Statement: Data is contained within the article or supplementary material.

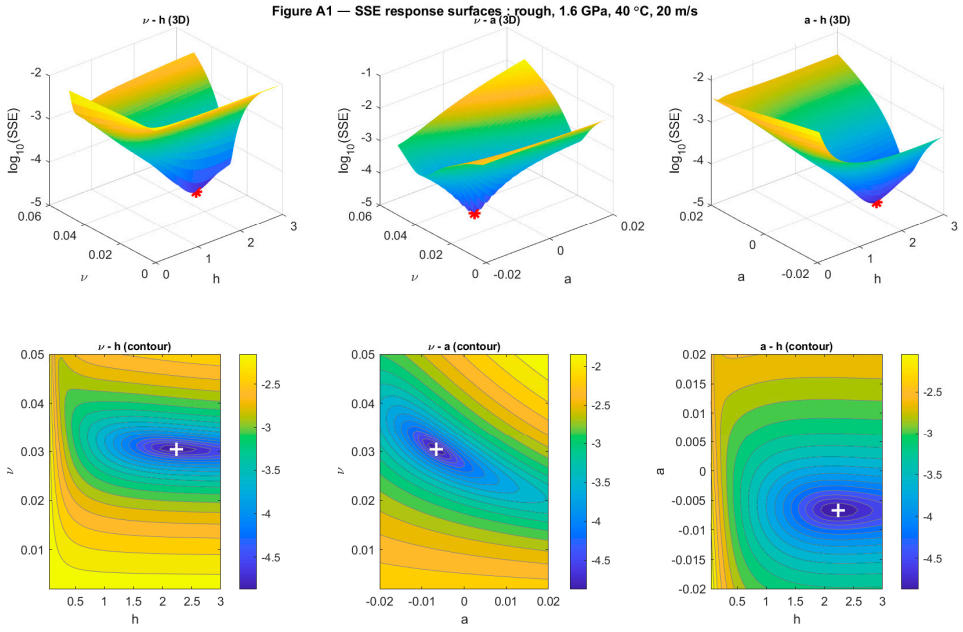
Conflicts of Interest: The authors declare no conflict of interest.

Appendix A. Complete Figure Sets

For readability, the figures of the main text show a representative subset of the results. This appendix reproduces, for every operating condition, the complete set of outputs with the original table layout (surface state, contact pressure, temperature and speed).

A.1. Response Surfaces of the SSE (complete set of Figure 3)





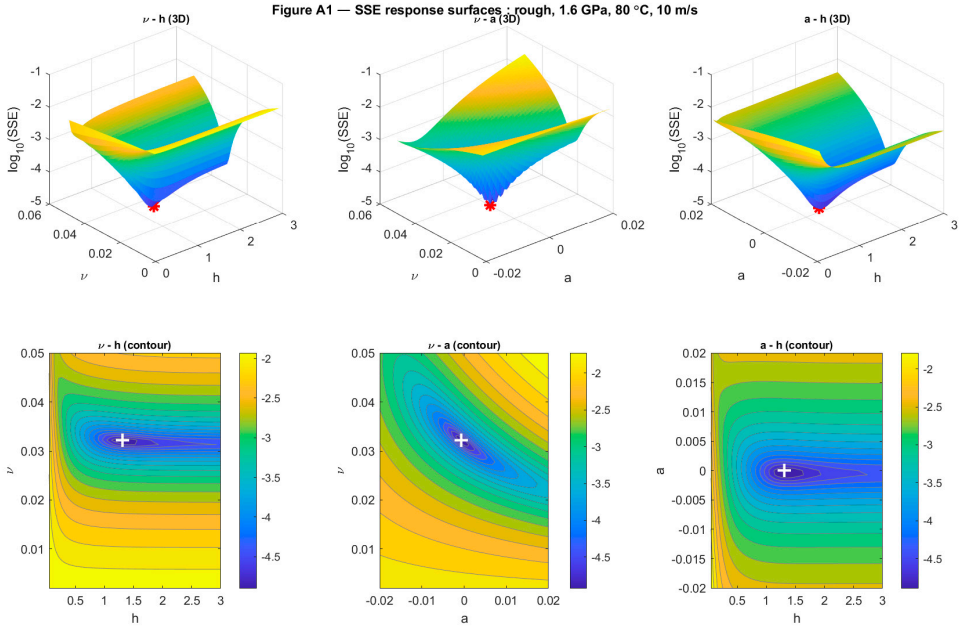


Figure A1 — SSE response surfaces : rough, 1.6 GPa, 80 °C, 10 m/s

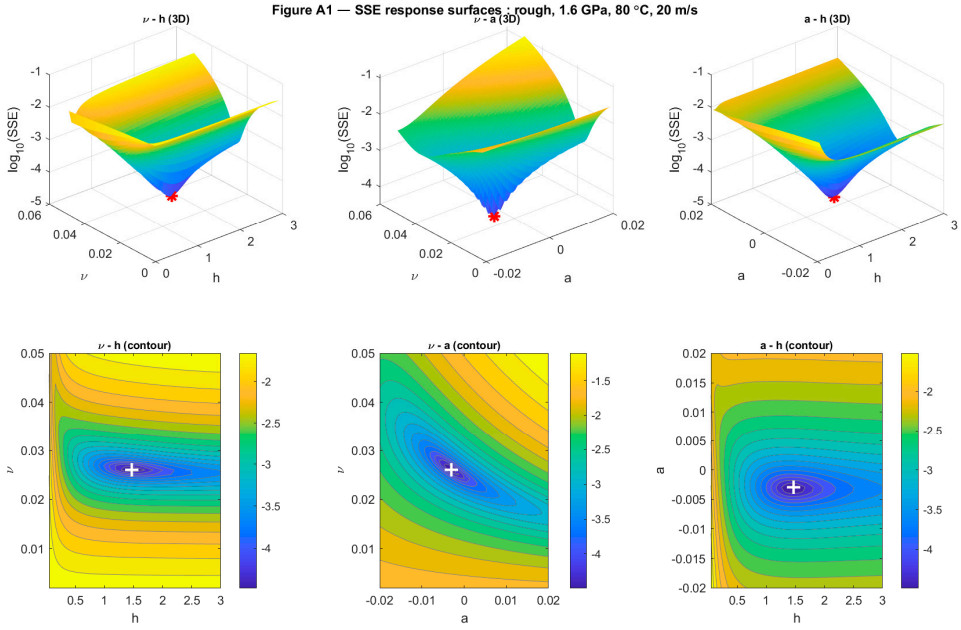


Figure A1 — SSE response surfaces : rough, 1.6 GPa, 80 °C, 20 m/s

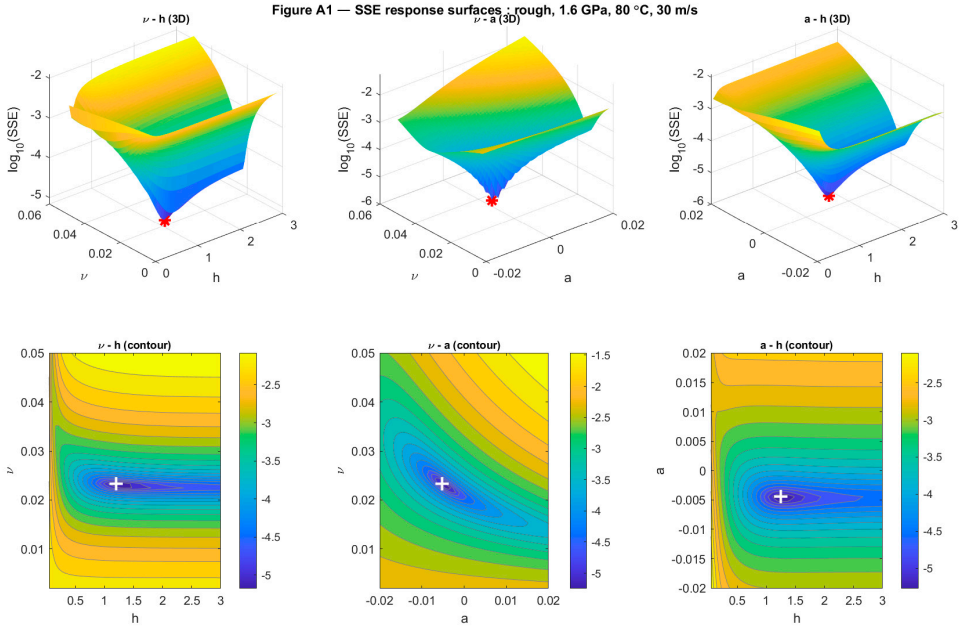


Figure A1 — SSE response surfaces : rough, 1.6 GPa, 80 °C, 30 m/s

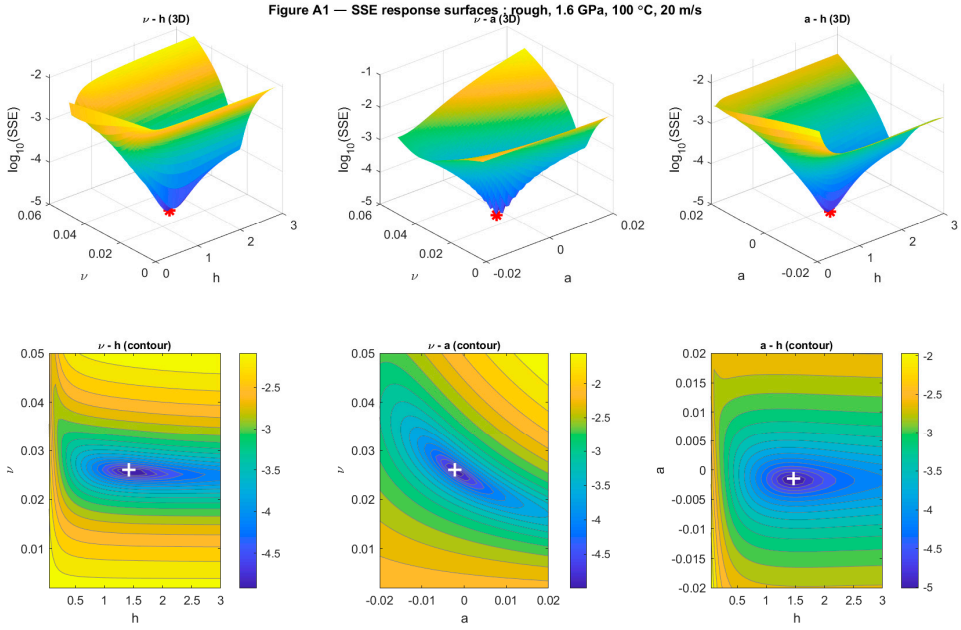


Figure A1 — SSE response surfaces : rough, 1.6 GPa, 100 °C, 20 m/s

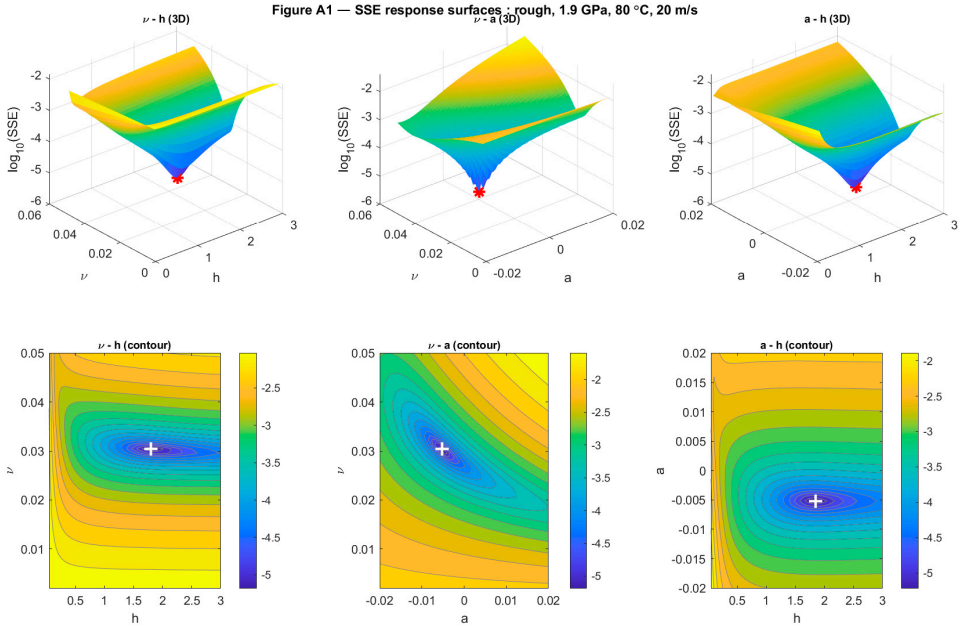


Figure A1 — SSE response surfaces : rough, 1.9 GPa, 80 °C, 20 m/s

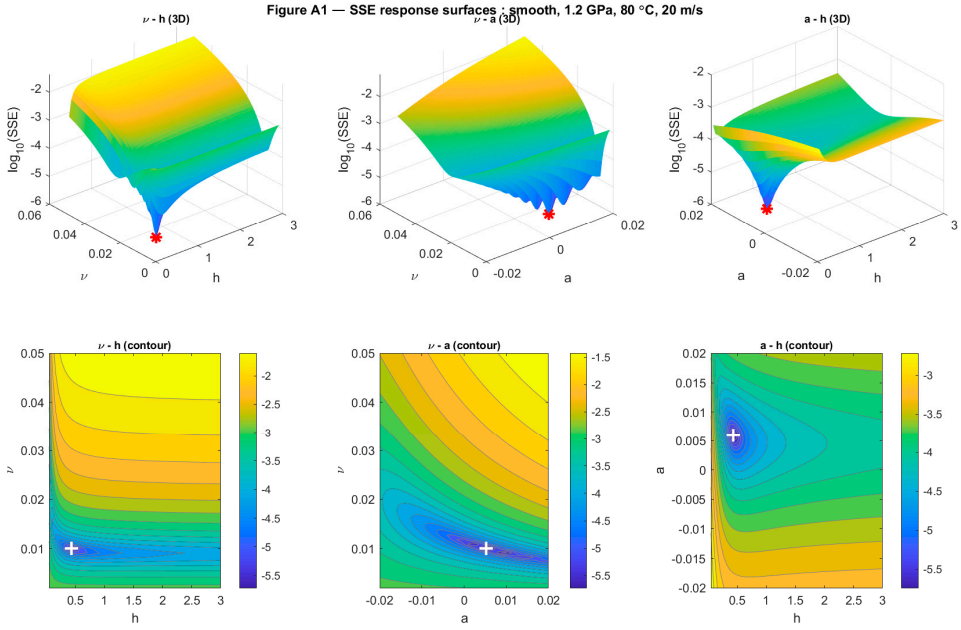


Figure A1 — SSE response surfaces : smooth, 1.2 GPa, 80 °C, 20 m/s

Figure A1 — SSE response surfaces : smooth, 1.6 GPa, 40 °C, 20 m/s

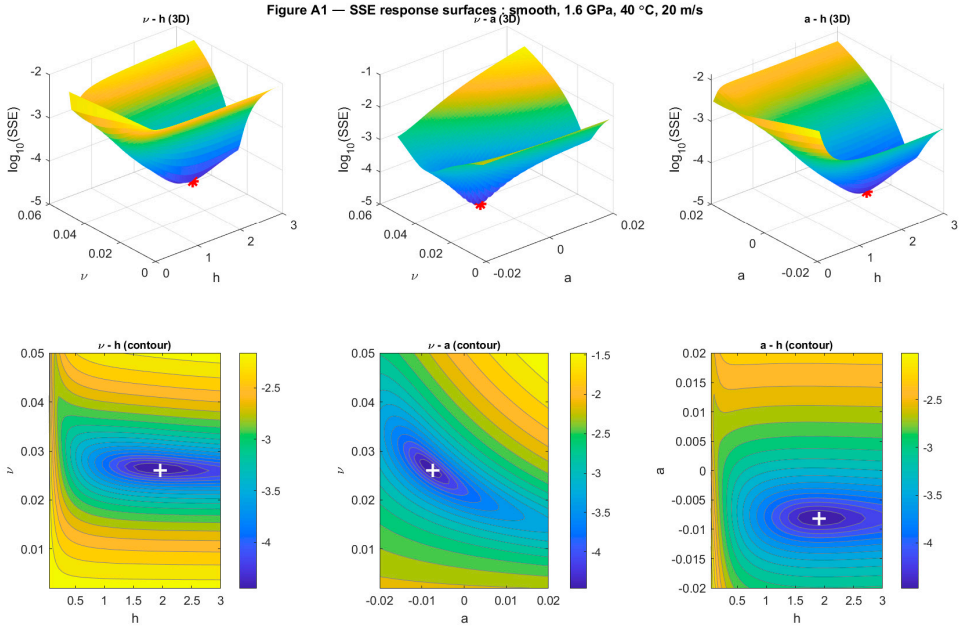


Figure A1 — SSE response surfaces : smooth, 1.6 GPa, 80 °C, 10 m/s

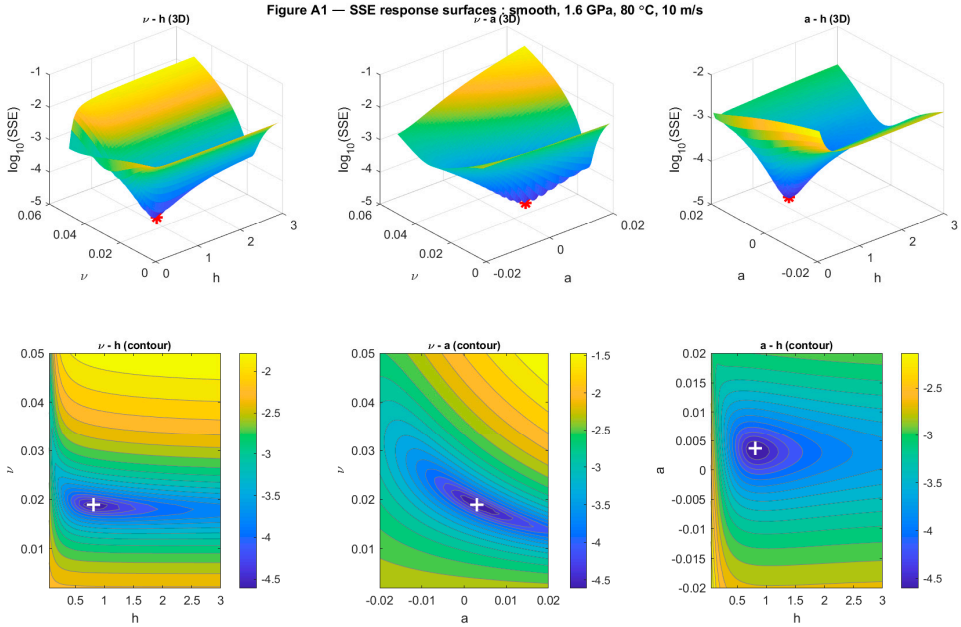


Figure A1 — SSE response surfaces : smooth, 1.6 GPa, 80 °C, 20 m/s

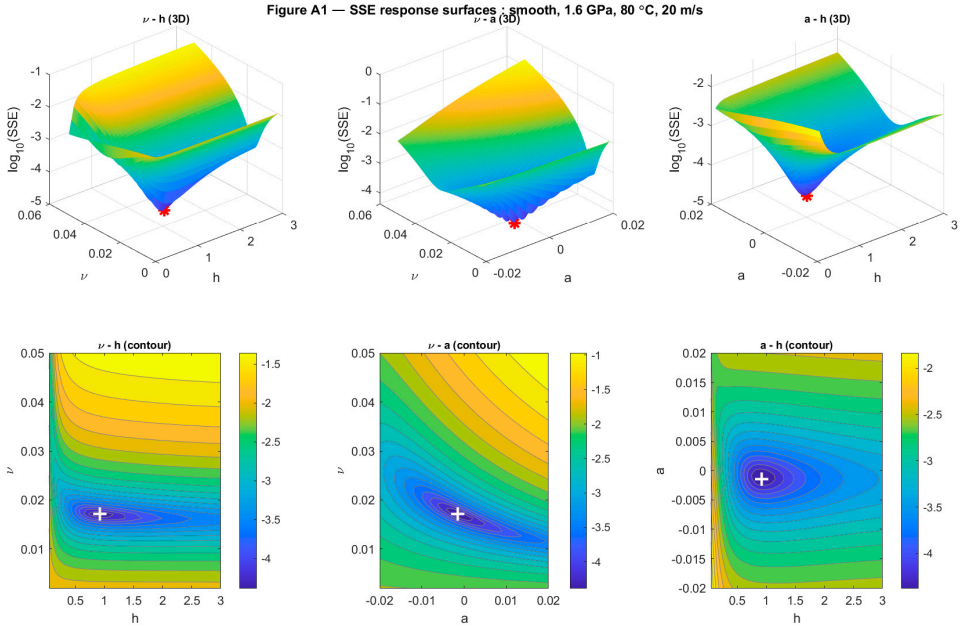
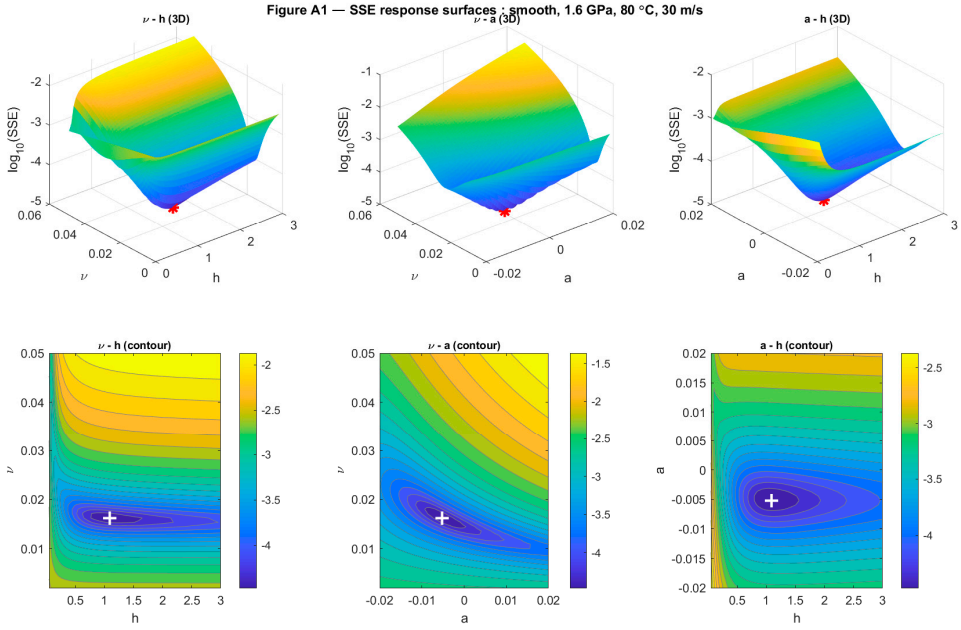


Figure A1 — SSE response surfaces : smooth, 1.6 GPa, 80 °C, 30 m/s



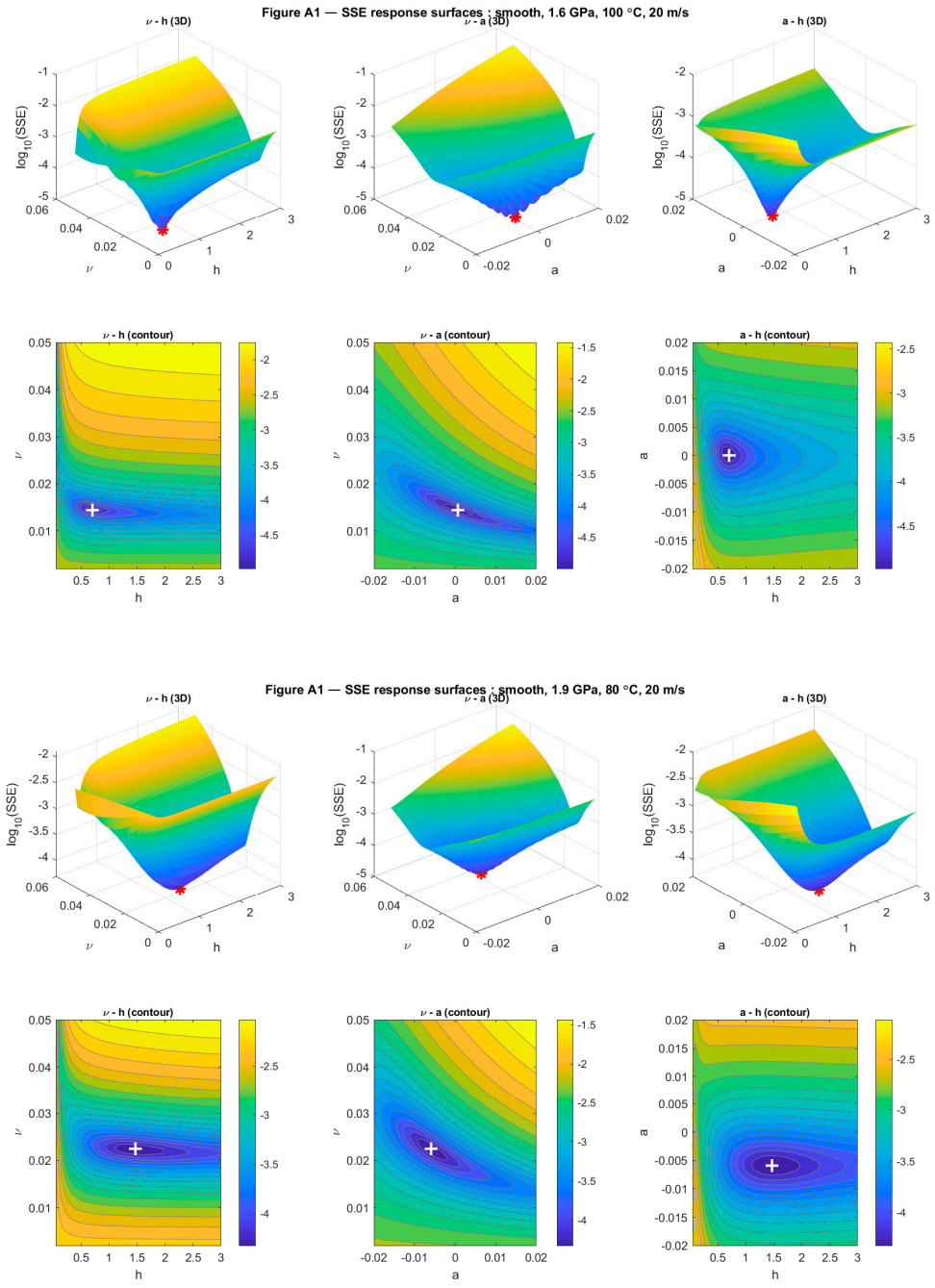
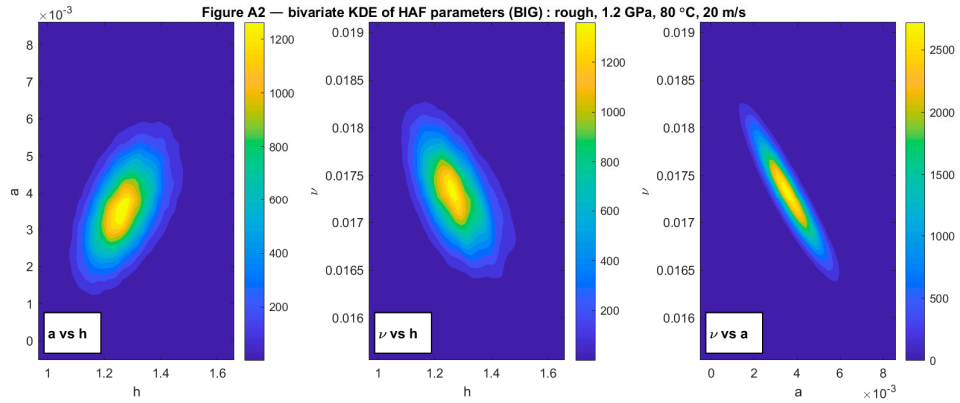
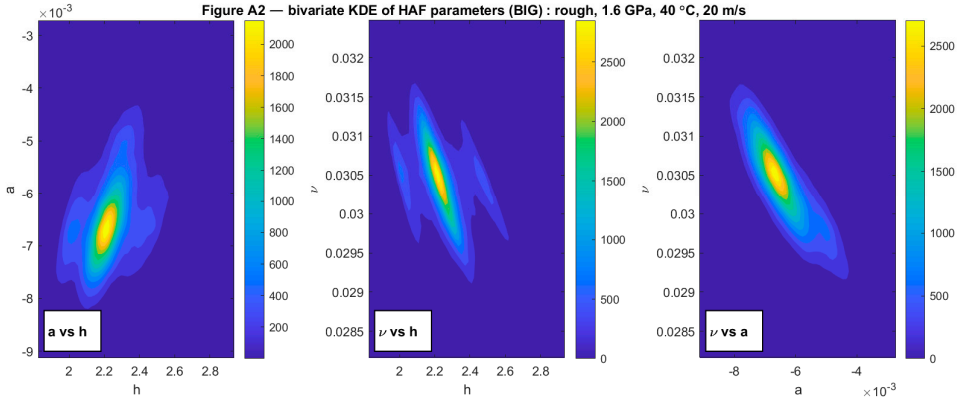
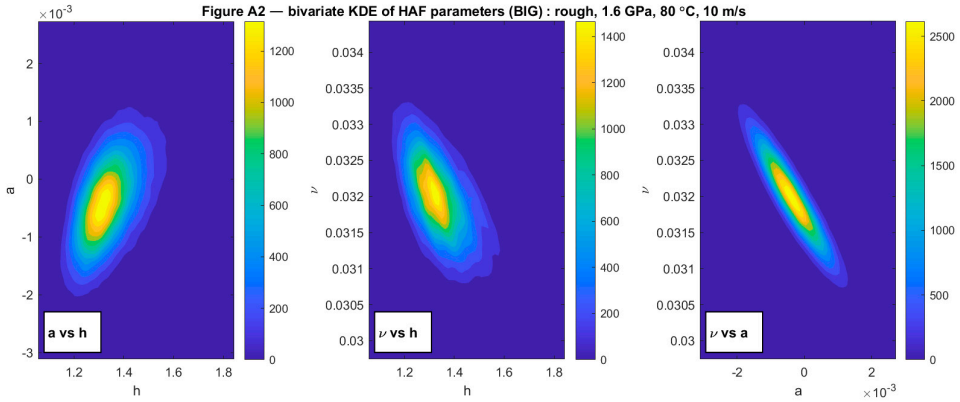


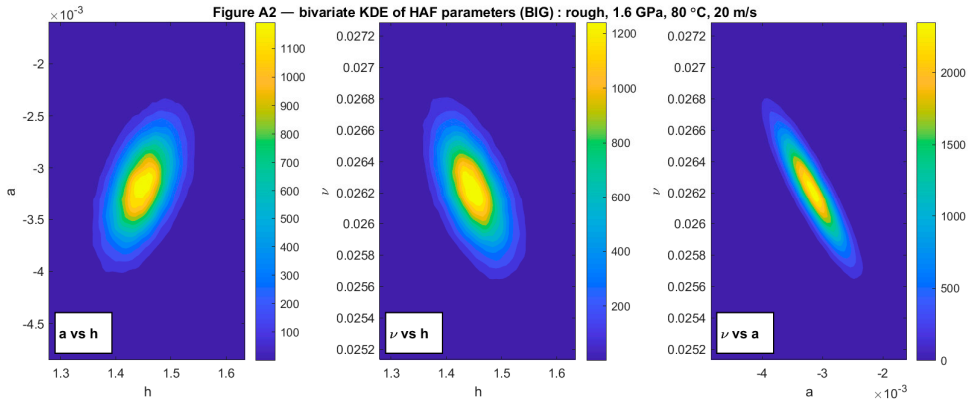
Figure A1. Response surface plots of the SSE versus the HAF parameters (v, a, h) for both smooth and rough surfaces at the three contact pressures, three temperatures and three speeds. Each row corresponds to one operating condition; the three views show the v–a, v–h and a–h parameter pairs. A single, well-defined minimum is observed in every case.

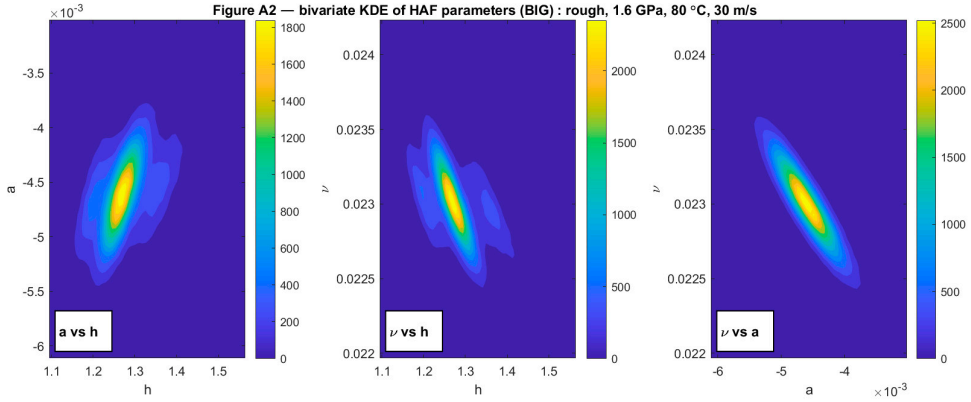
A.2. Bivariate Kernel Density Plots (complete set of Figure 6)

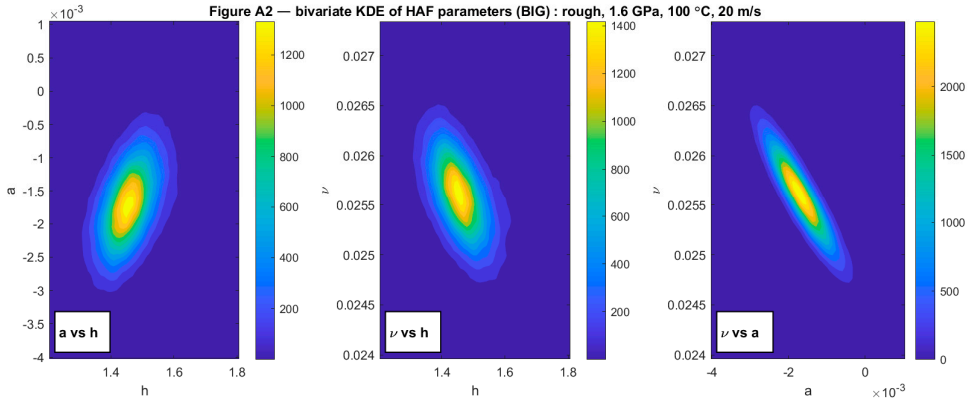







Figure A2 — bivariate KDE of HAF parameters (BIG) : rough, 1.6 GPa, 80 °C, 20 m/s
a vs h
ν vs h
ν vs a
h
a
ν
×10-3


Figure A2 — bivariate KDE of HAF parameters (BIG) : rough, 1.6 GPa, 80 °C, 30 m/s
a vs h
ν vs h
ν vs a
h
a
ν
×10-3


Figure A2 — bivariate KDE of HAF parameters (BIG) : rough, 1.6 GPa, 100 °C, 20 m/s
a vs h
ν vs h
ν vs a
h
a
ν
×10-3

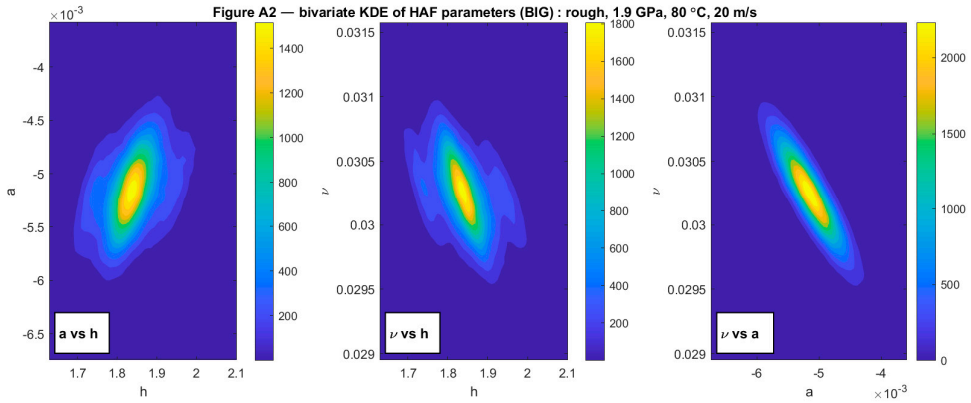


Figure A2 — bivariate KDE of HAF parameters (BIG) : rough, 1.9 GPa, 80 °C, 20 m/s

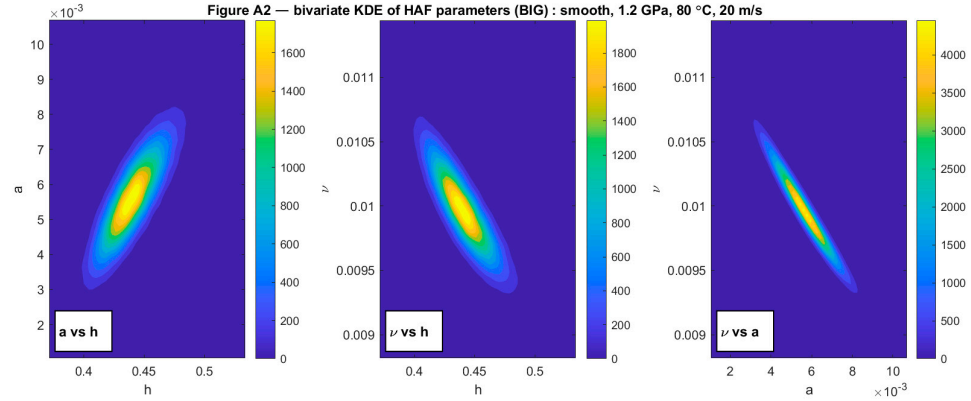


Figure A2 — bivariate KDE of HAF parameters (BIG) : smooth, 1.2 GPa, 80 °C, 20 m/s

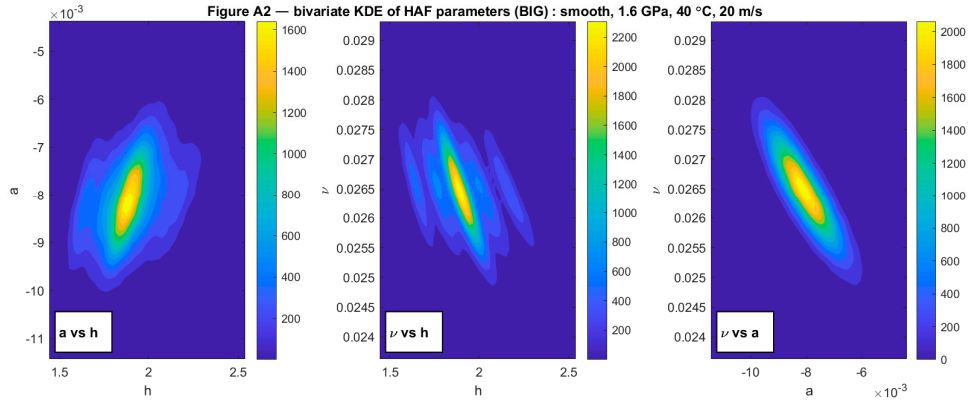


Figure A2 — bivariate KDE of HAF parameters (BIG) : smooth, 1.6 GPa, 40 °C, 20 m/s

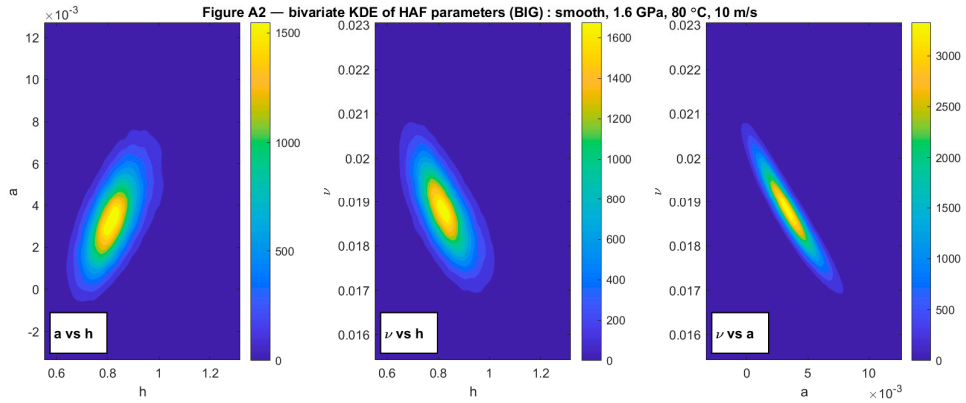


Figure A2 — bivariate KDE of HAF parameters (BIG) : smooth, 1.6 GPa, 80 °C, 10 m/s

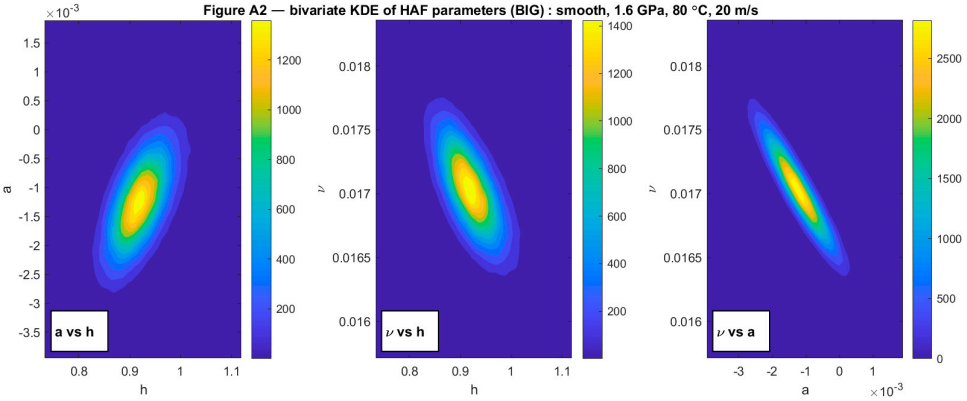


Figure A2 — bivariate KDE of HAF parameters (BIG) : smooth, 1.6 GPa, 80 °C, 20 m/s

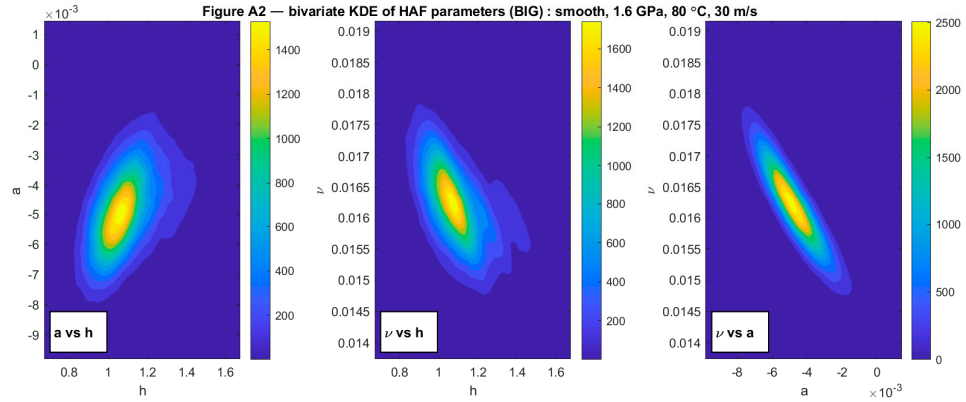


Figure A2 — bivariate KDE of HAF parameters (BIG) : smooth, 1.6 GPa, 80 °C, 30 m/s

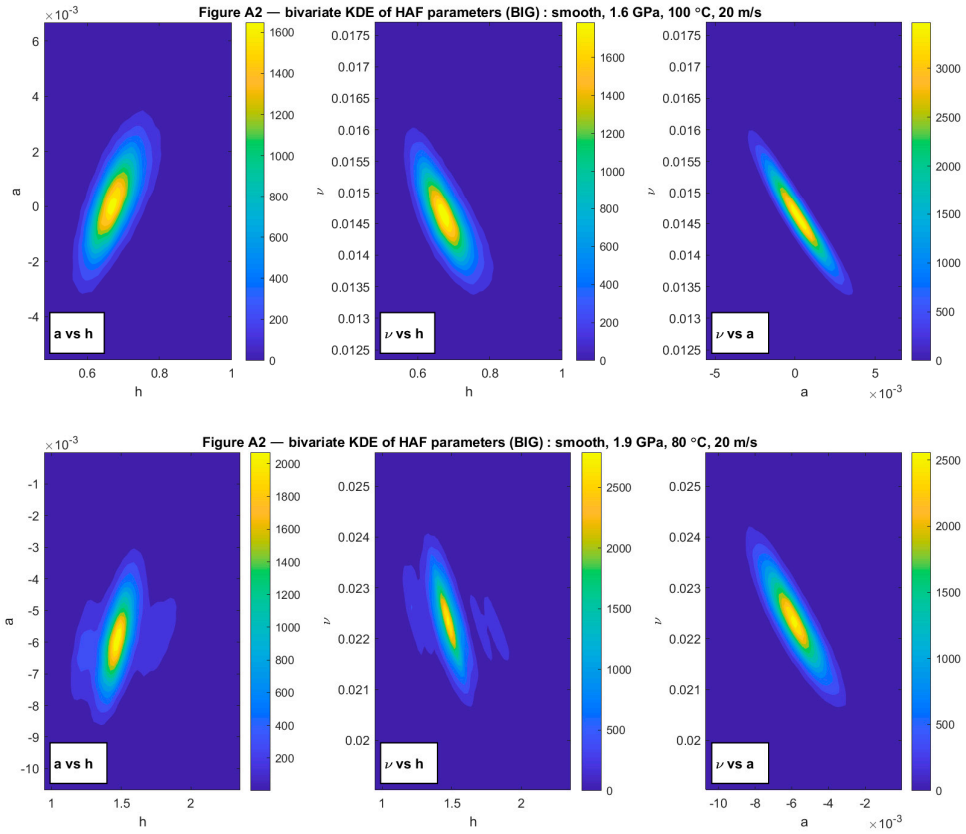


Figure A2. Bivariate kernel density plots of the HAF parameters (a vs h, v vs h, v vs a) built from the BIG bootstrap samples, for rough (left) and smooth (right) surfaces at each operating condition.

A.3. Probability Density Plots – Experimental SRR Sampling (complete set of Figure 7)

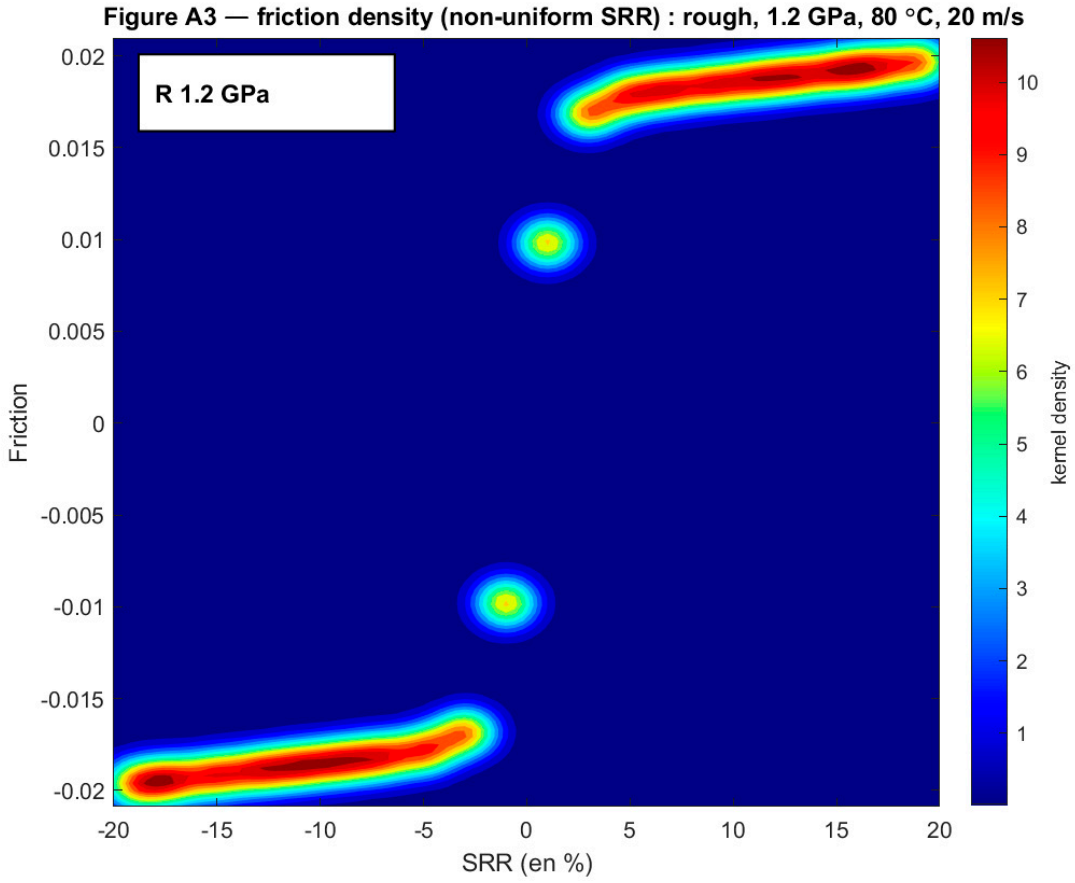


Figure A3 — friction density (non-uniform SRR) : rough, 1.6 GPa, 40 °C, 20 m/s

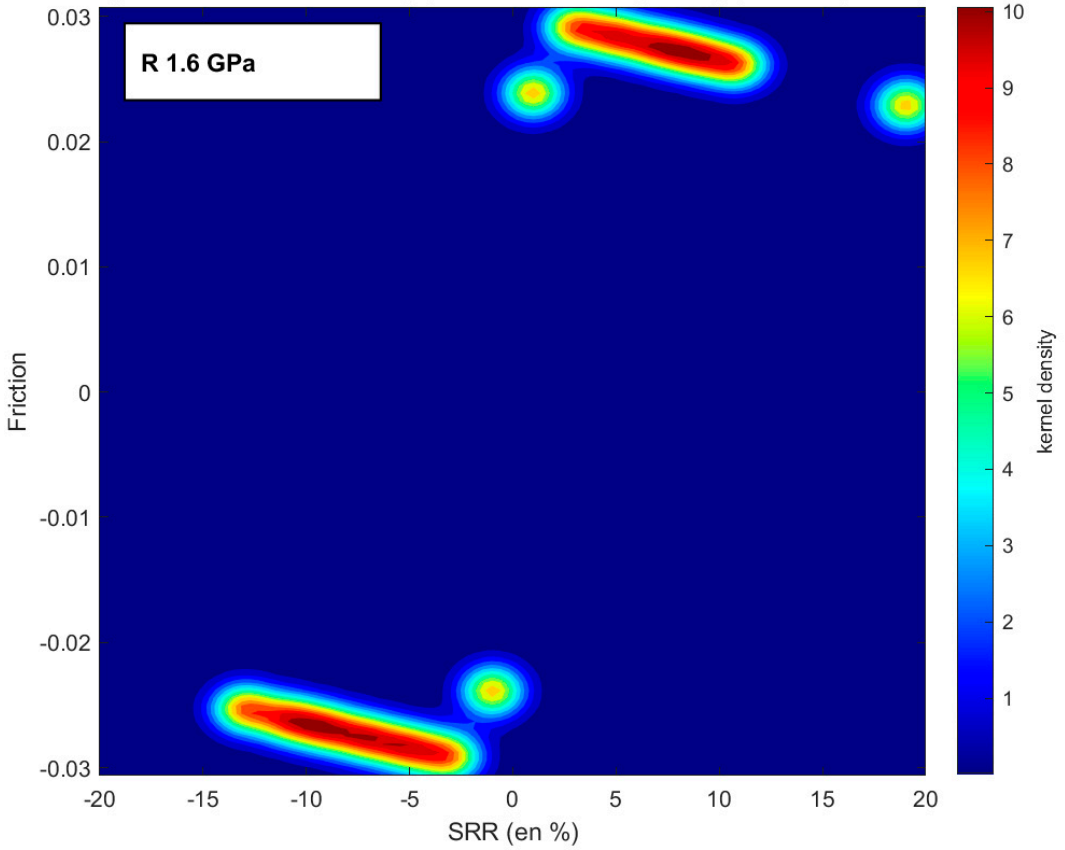


Figure A3 — friction density (non-uniform SRR) : rough, 1.6 GPa, 80 °C, 10 m/s

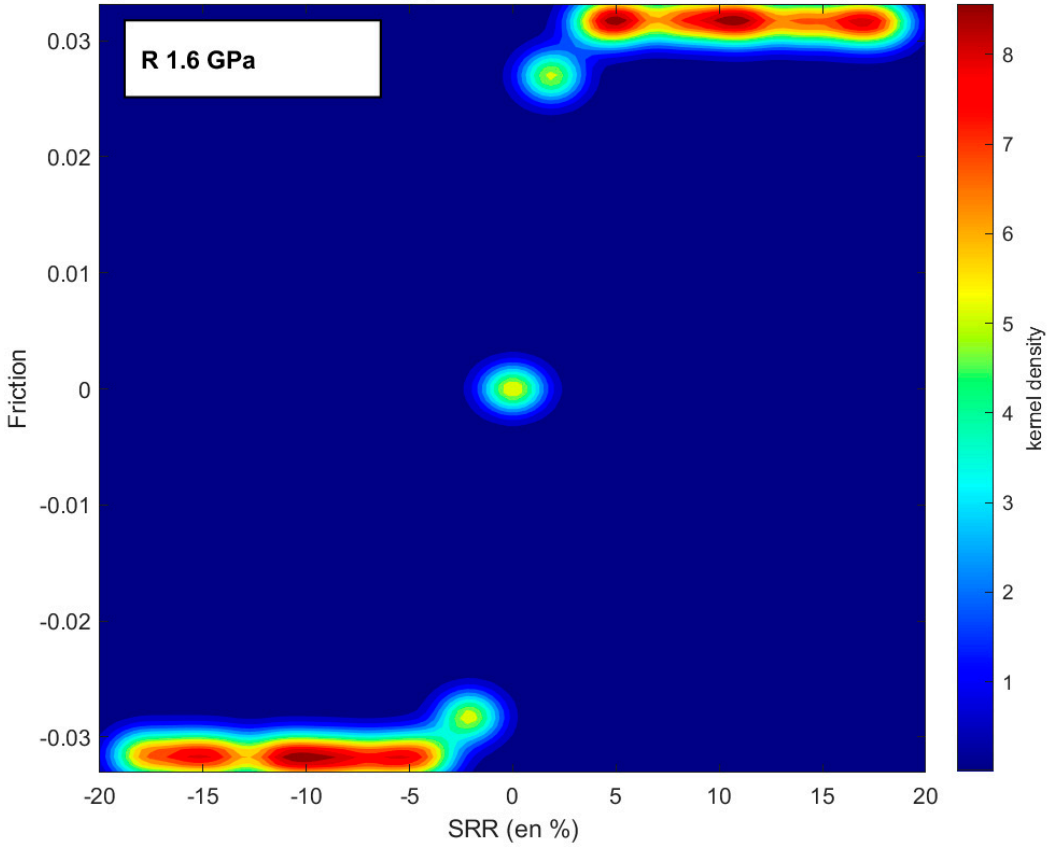


Figure A3 — friction density (non-uniform SRR) : rough, 1.6 GPa, 80 °C, 20 m/s

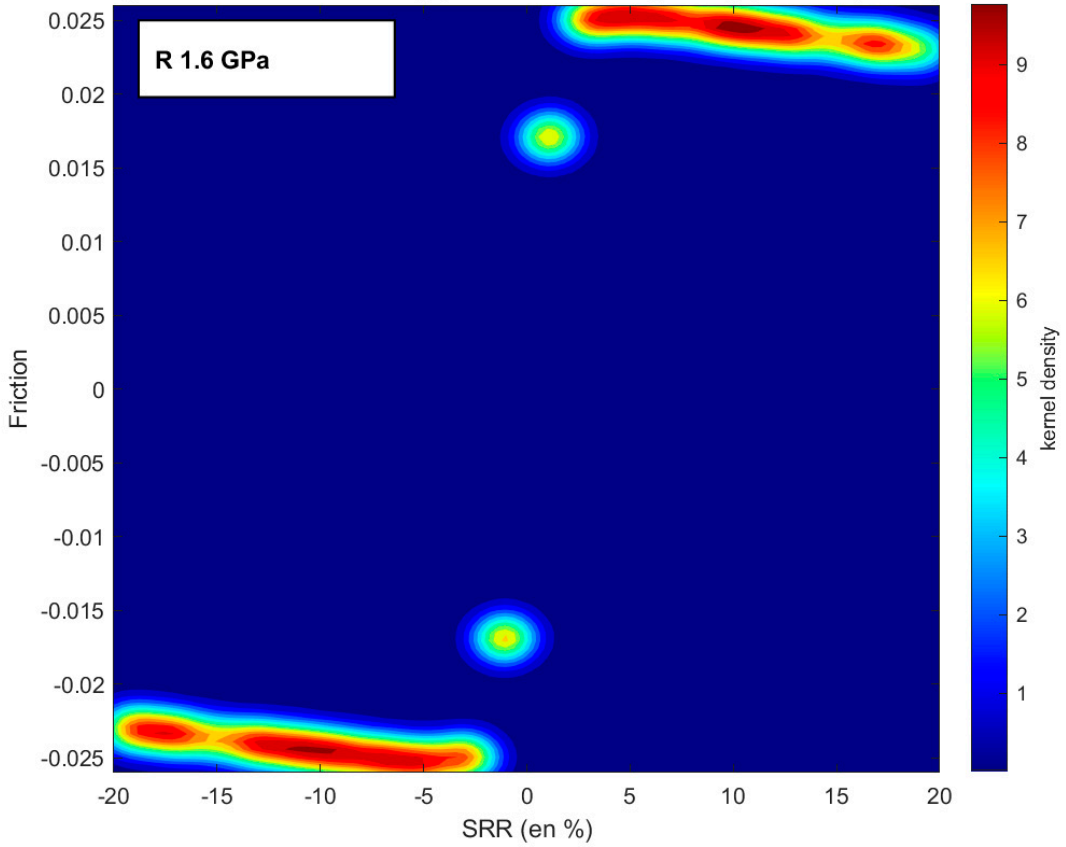


Figure A3 — friction density (non-uniform SRR) : rough, 1.6 GPa, 80 °C, 30 m/s

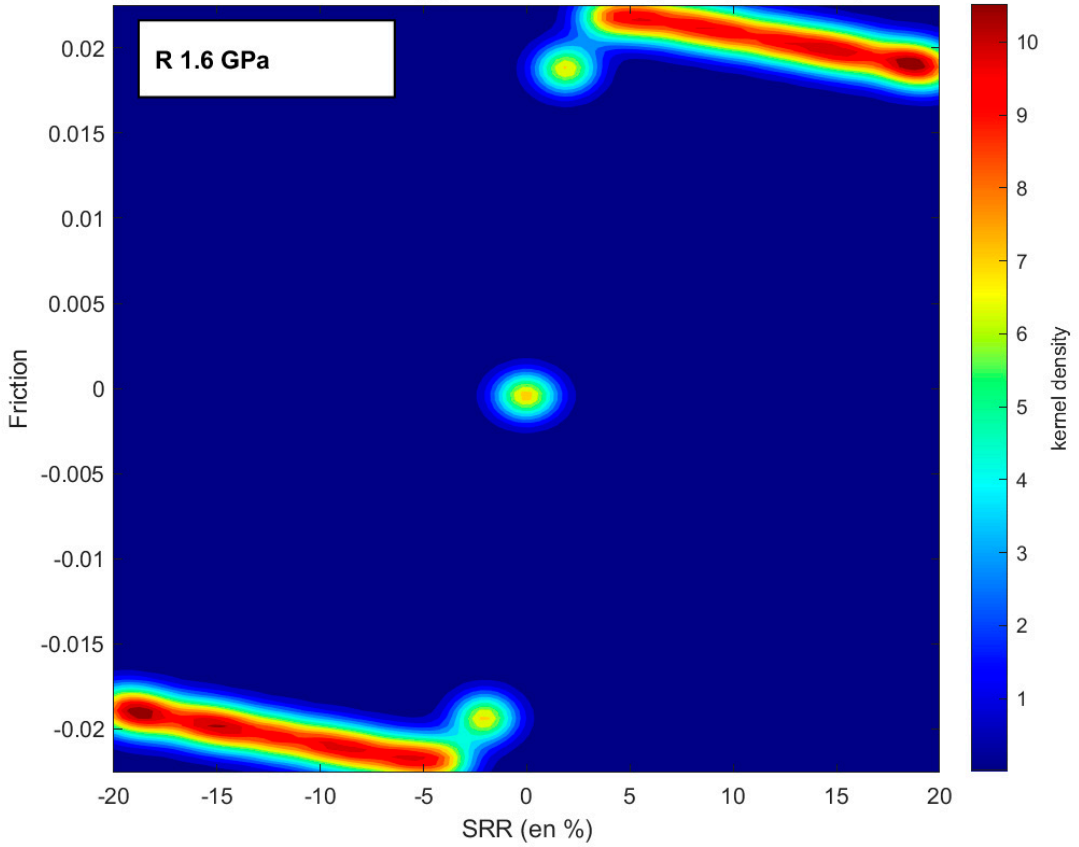


Figure A3 — friction density (non-uniform SRR) : rough, 1.6 GPa, 100 °C, 20 m/s

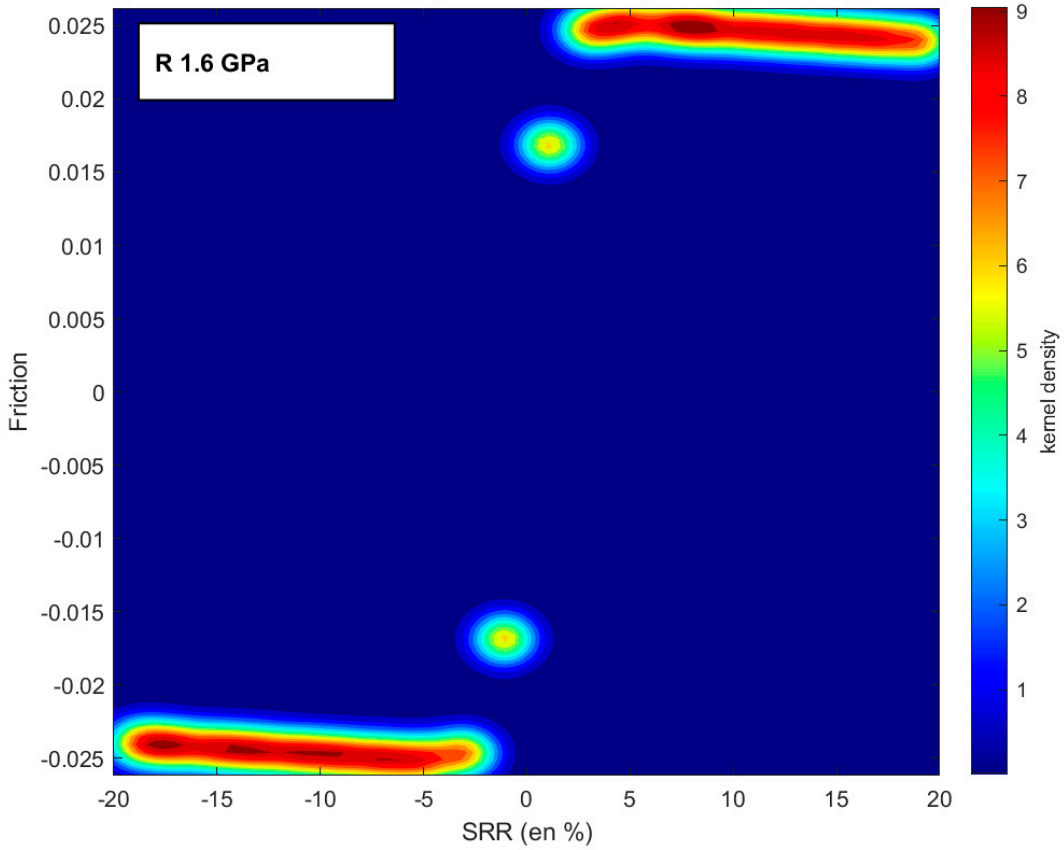


Figure A3 — friction density (non-uniform SRR) : rough, 1.9 GPa, 80 °C, 20 m/s

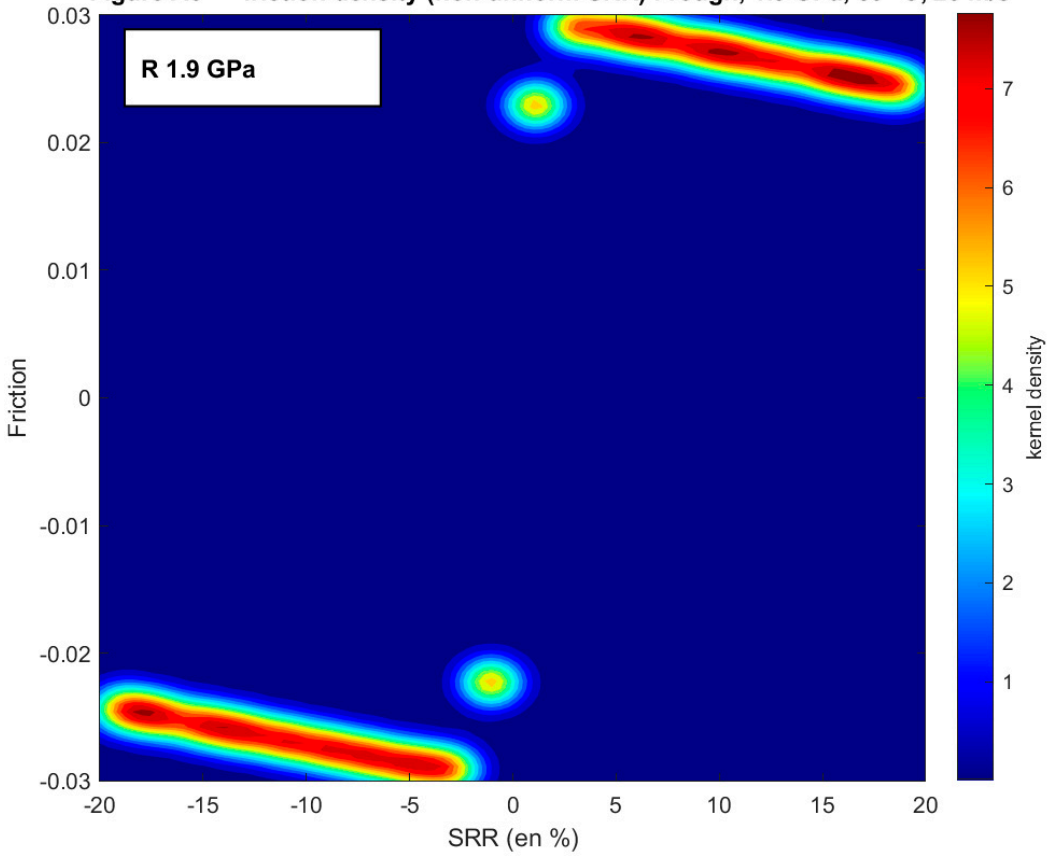


Figure A3 — friction density (non-uniform SRR) : smooth, 1.2 GPa, 80 °C, 20 m/s

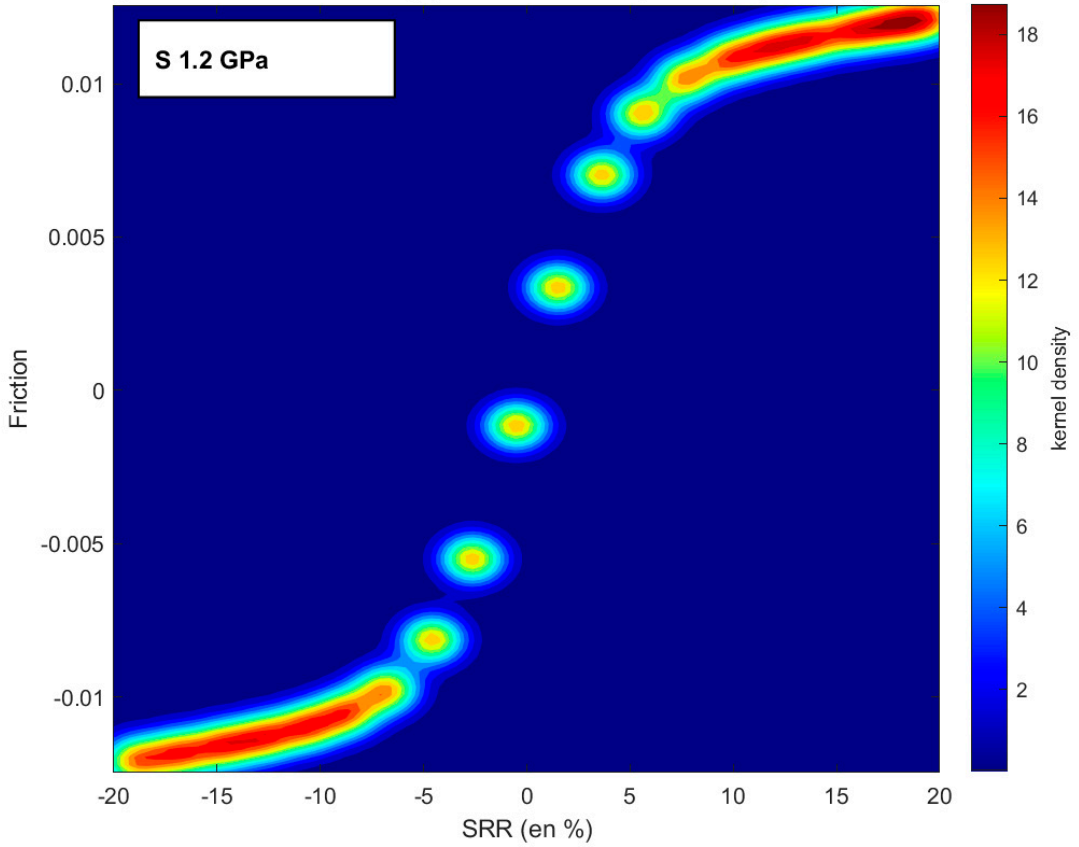


Figure A3 — friction density (non-uniform SRR) : smooth, 1.6 GPa, 40 °C, 20 m/s

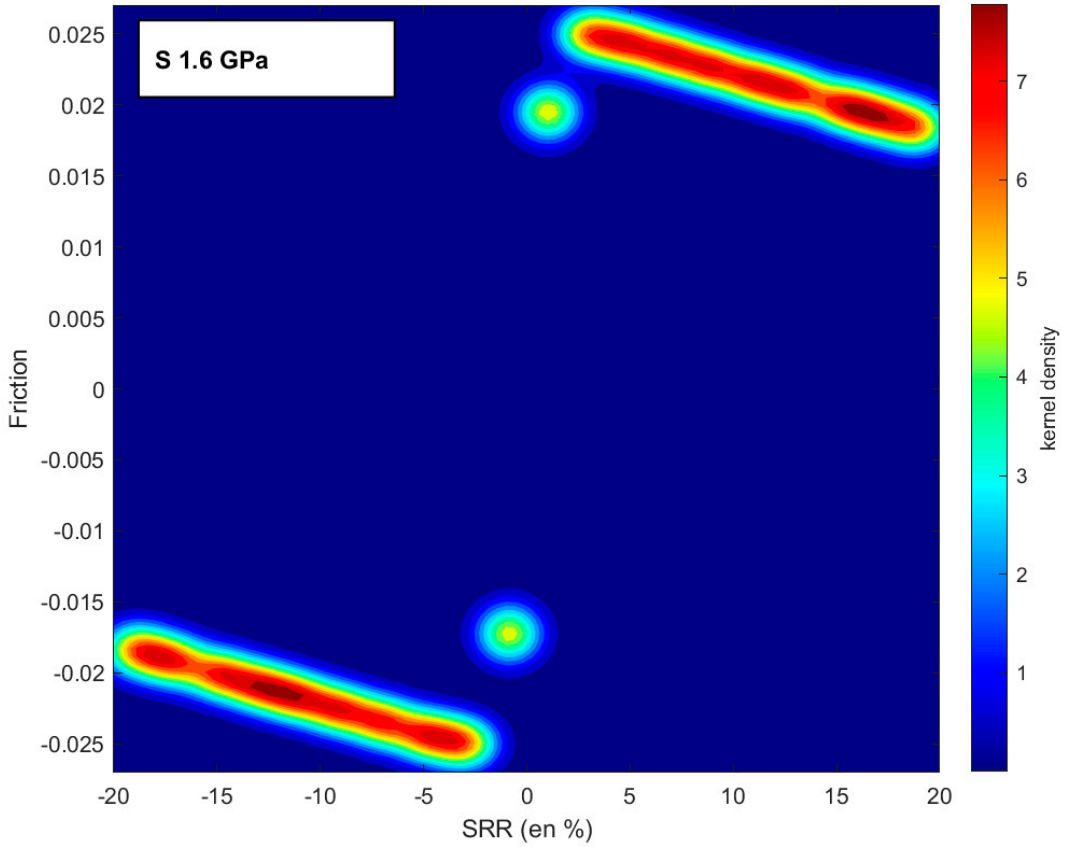


Figure A3 — friction density (non-uniform SRR) : smooth, 1.6 GPa, 80 °C, 10 m/s

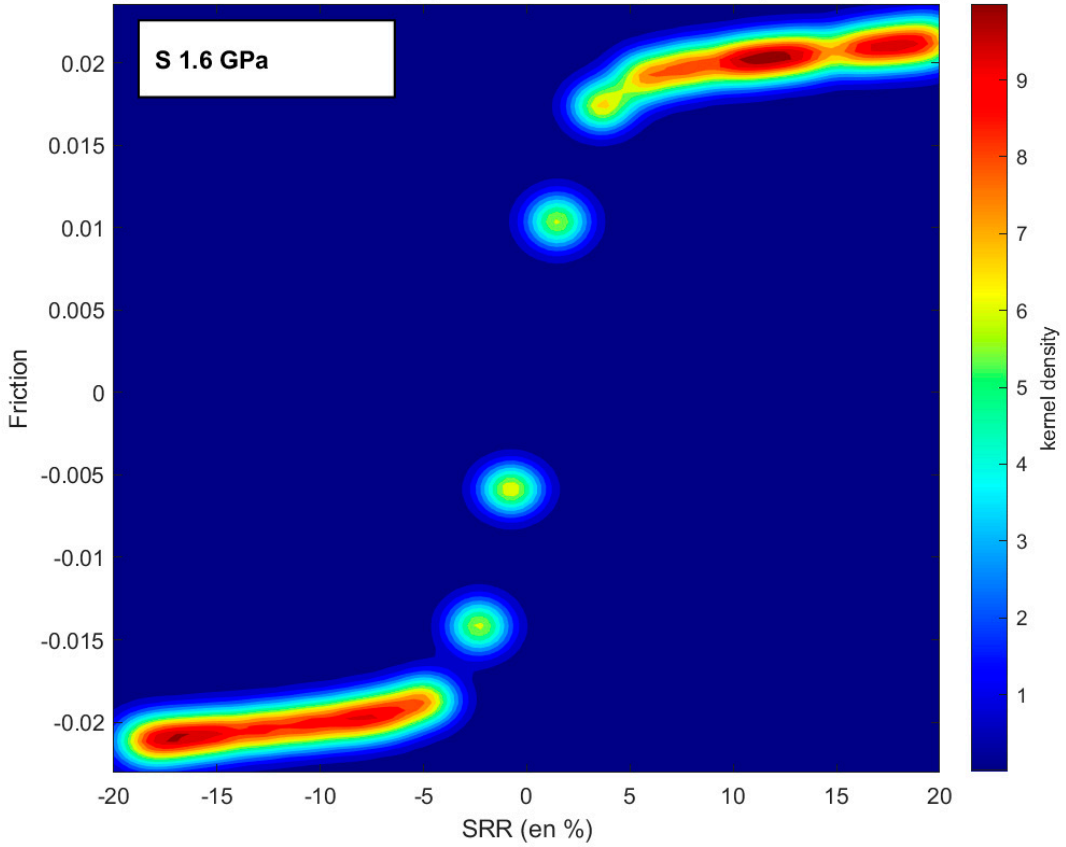


Figure A3 — friction density (non-uniform SRR) : smooth, 1.6 GPa, 80 °C, 20 m/s

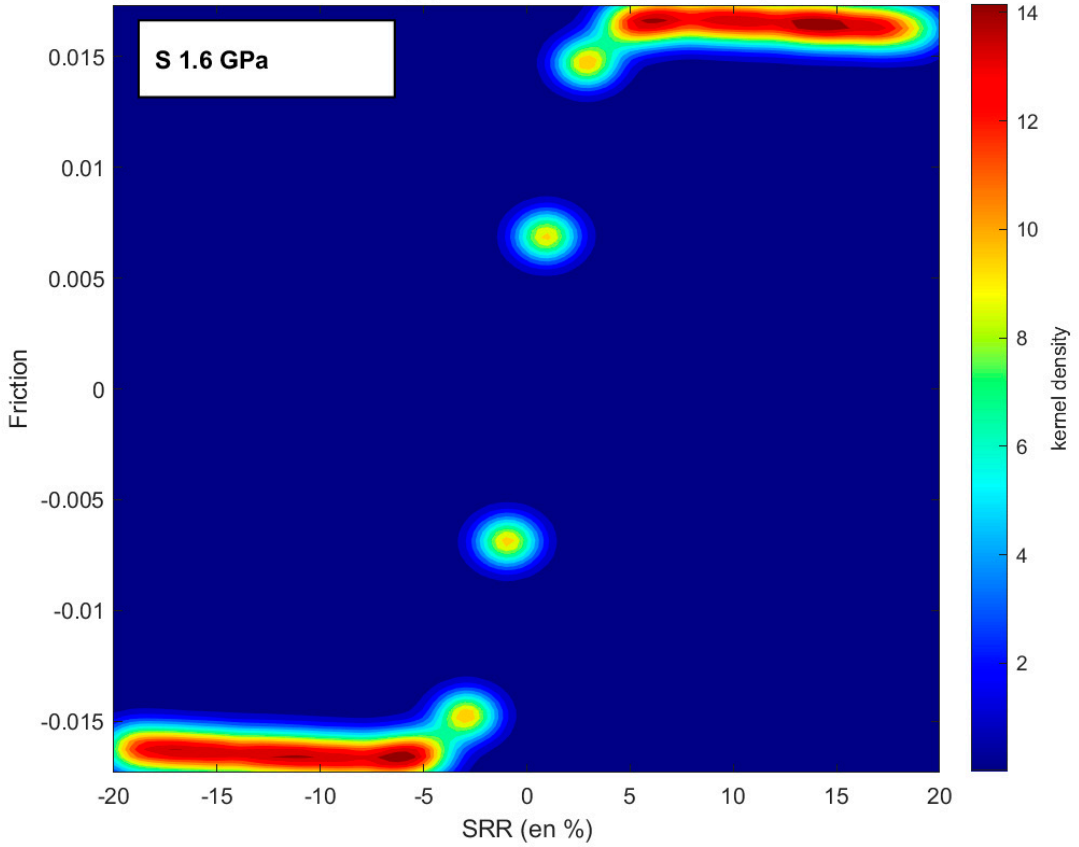
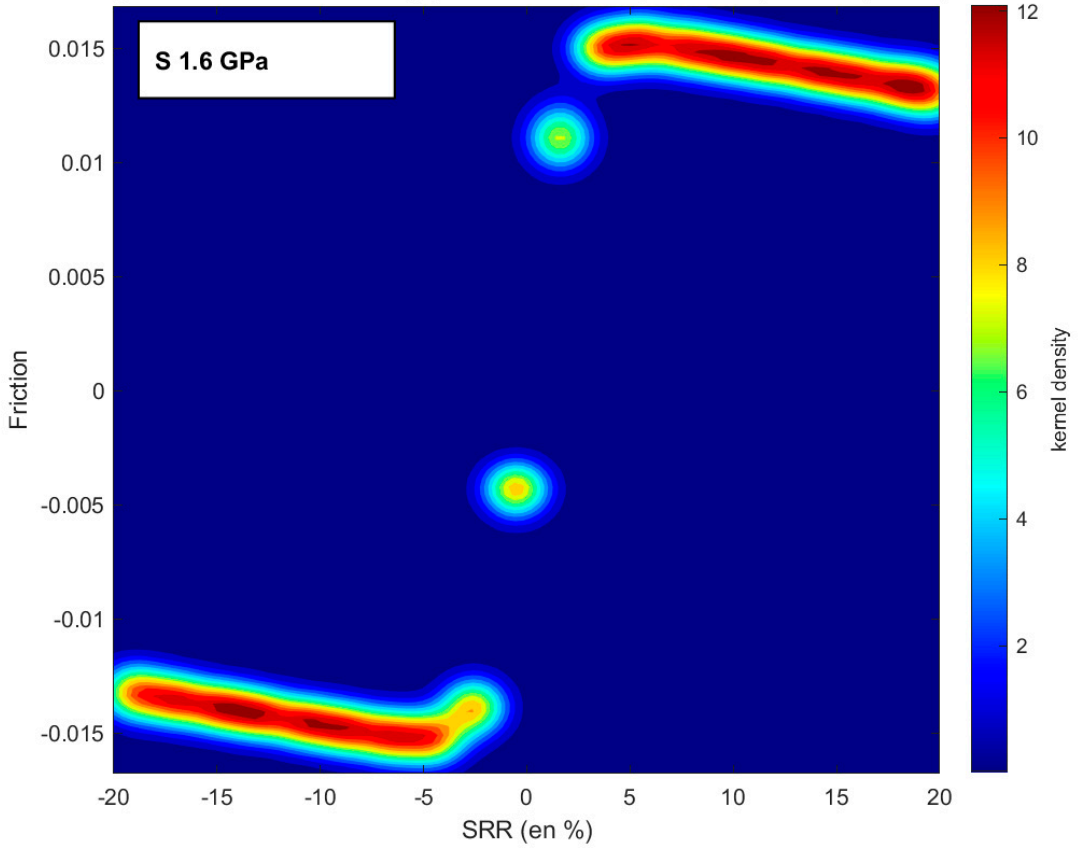


Figure A3 — friction density (non-uniform SRR) : smooth, 1.6 GPa, 80 °C, 30 m/s



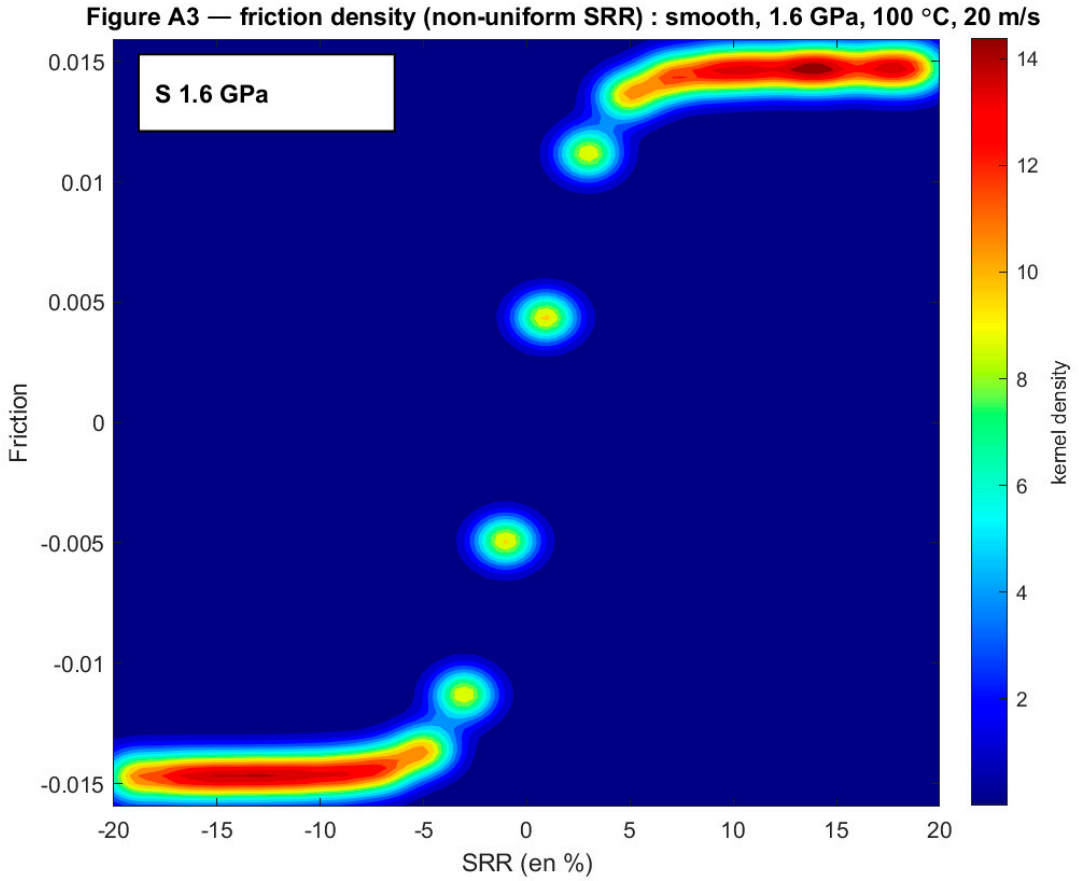


Figure A3. Probability density of the bootstrapped friction points along the friction–SRR curve (non-uniform SRR sampling). The density is concentrated at the asymptotes and thin along the rising branch of the sigmoid, where the h parameter is least supported by data.

A.4. Probability Density Plots – Uniform SRR Sampling (complete set of Figure 8)

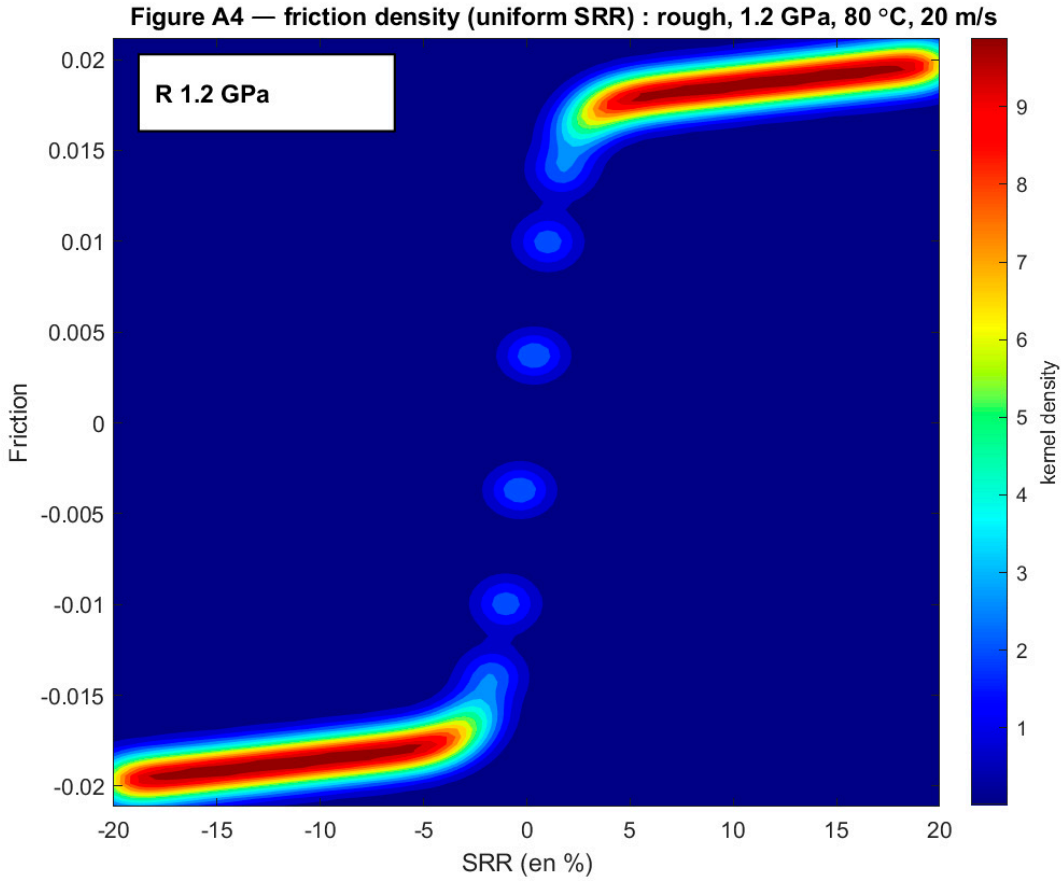


Figure A4 — friction density (uniform SRR) : rough, 1.6 GPa, 40 °C, 20 m/s

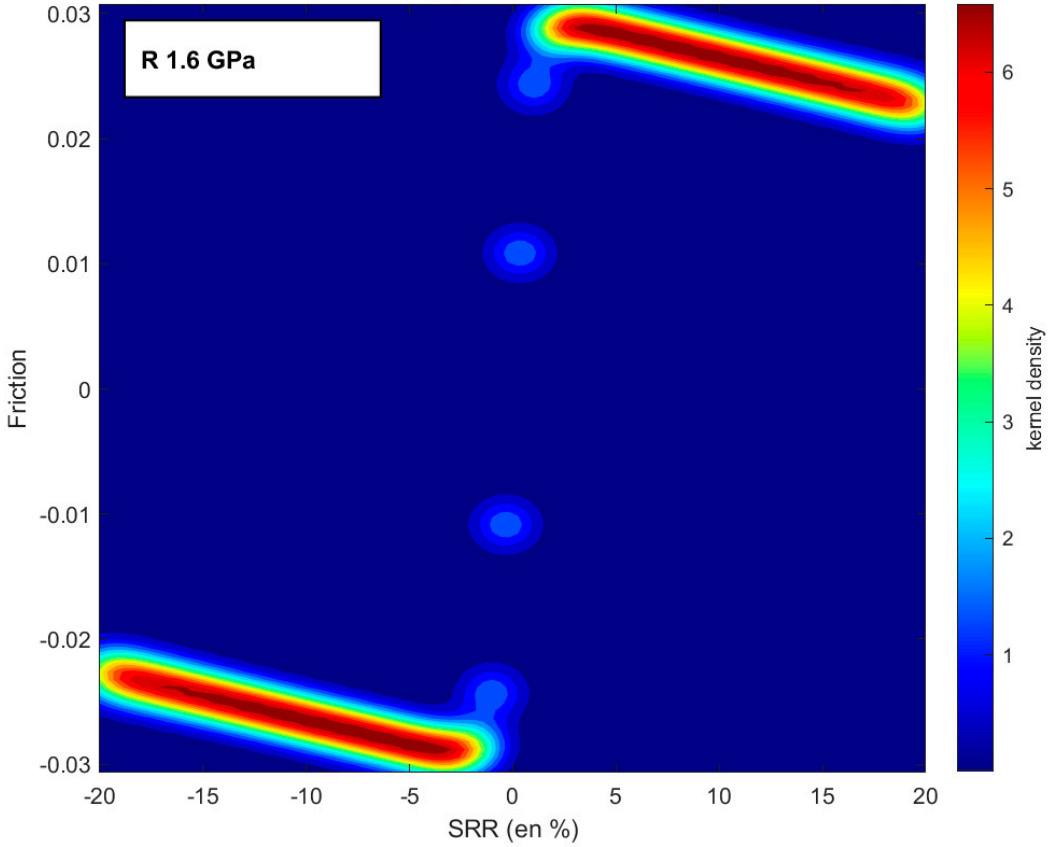


Figure A4 — friction density (uniform SRR) : rough, 1.6 GPa, 80 °C, 10 m/s

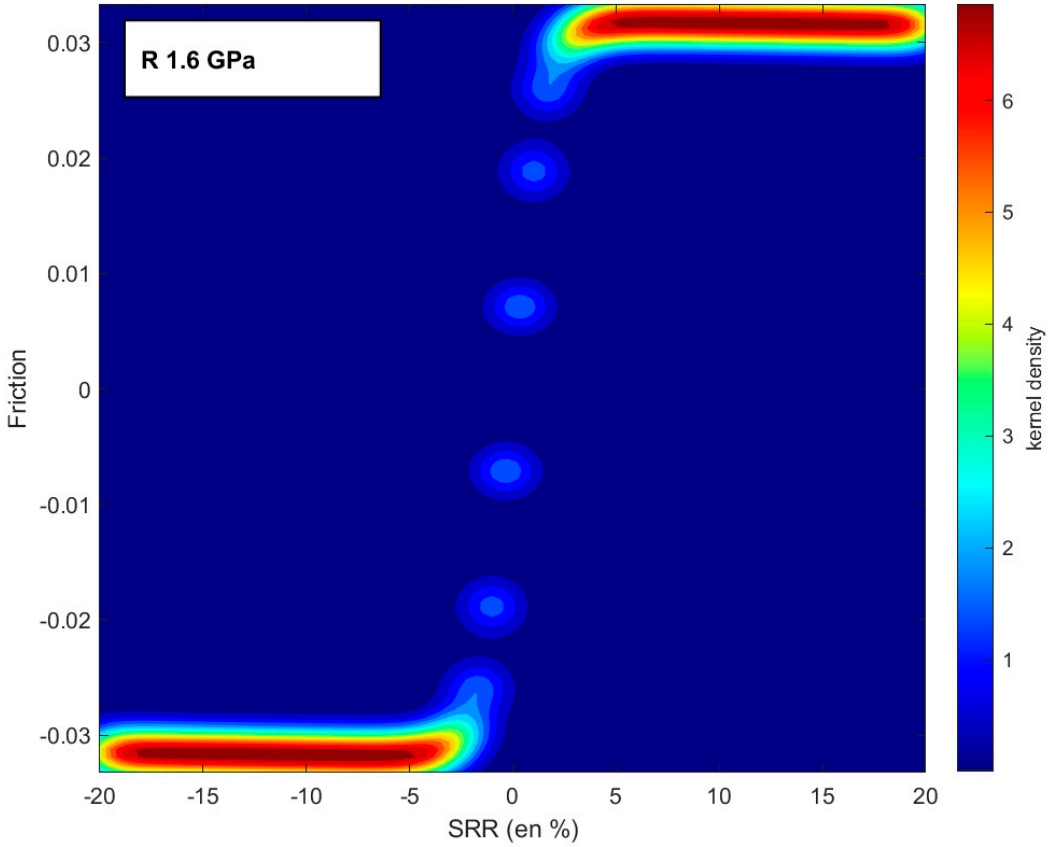


Figure A4 — friction density (uniform SRR) : rough, 1.6 GPa, 80 °C, 20 m/s

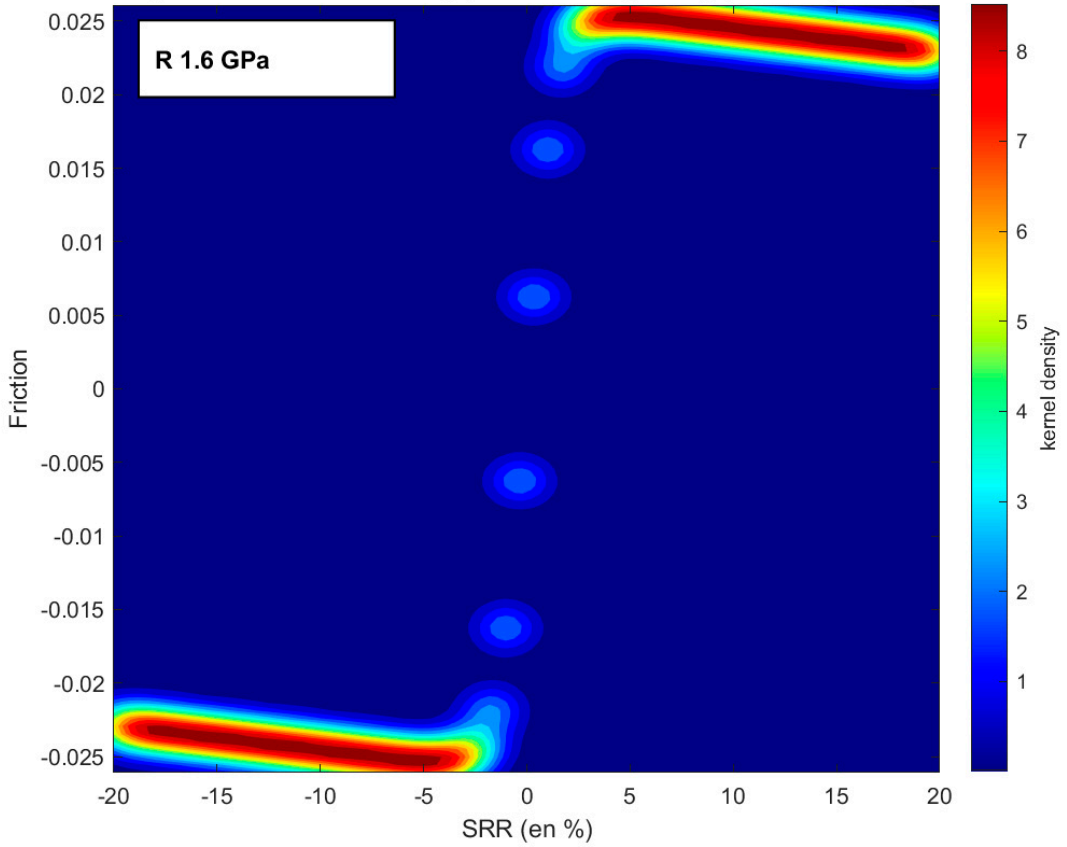


Figure A4 — friction density (uniform SRR) : rough, 1.6 GPa, 80 °C, 30 m/s

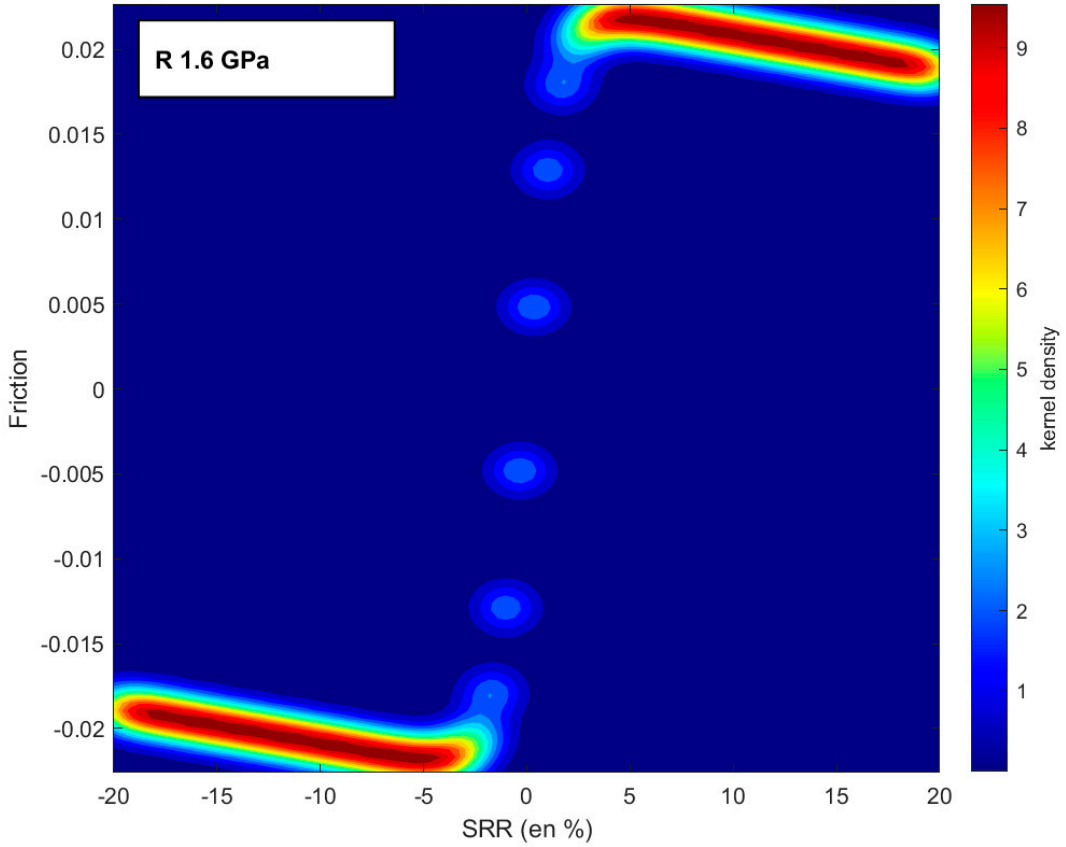


Figure A4 — friction density (uniform SRR) : rough, 1.6 GPa, 100 °C, 20 m/s

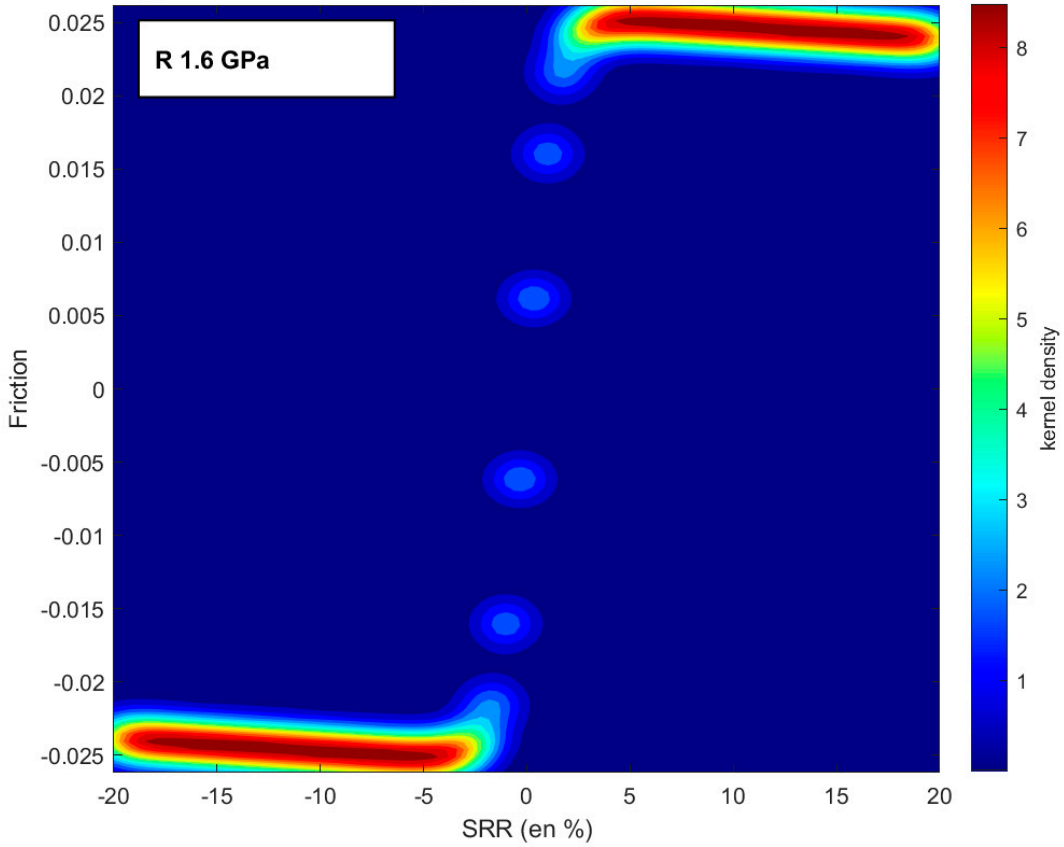


Figure A4 — friction density (uniform SRR) : rough, 1.9 GPa, 80 °C, 20 m/s

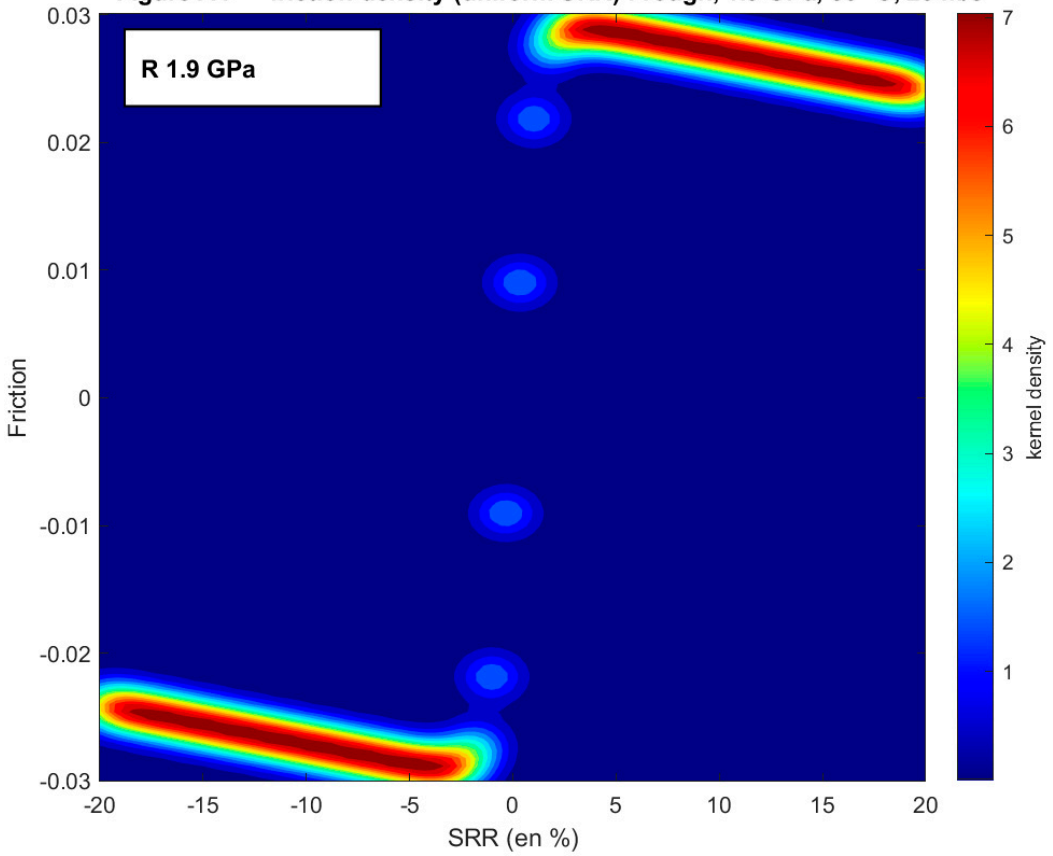


Figure A4 — friction density (uniform SRR) : smooth, 1.2 GPa, 80 °C, 20 m/s

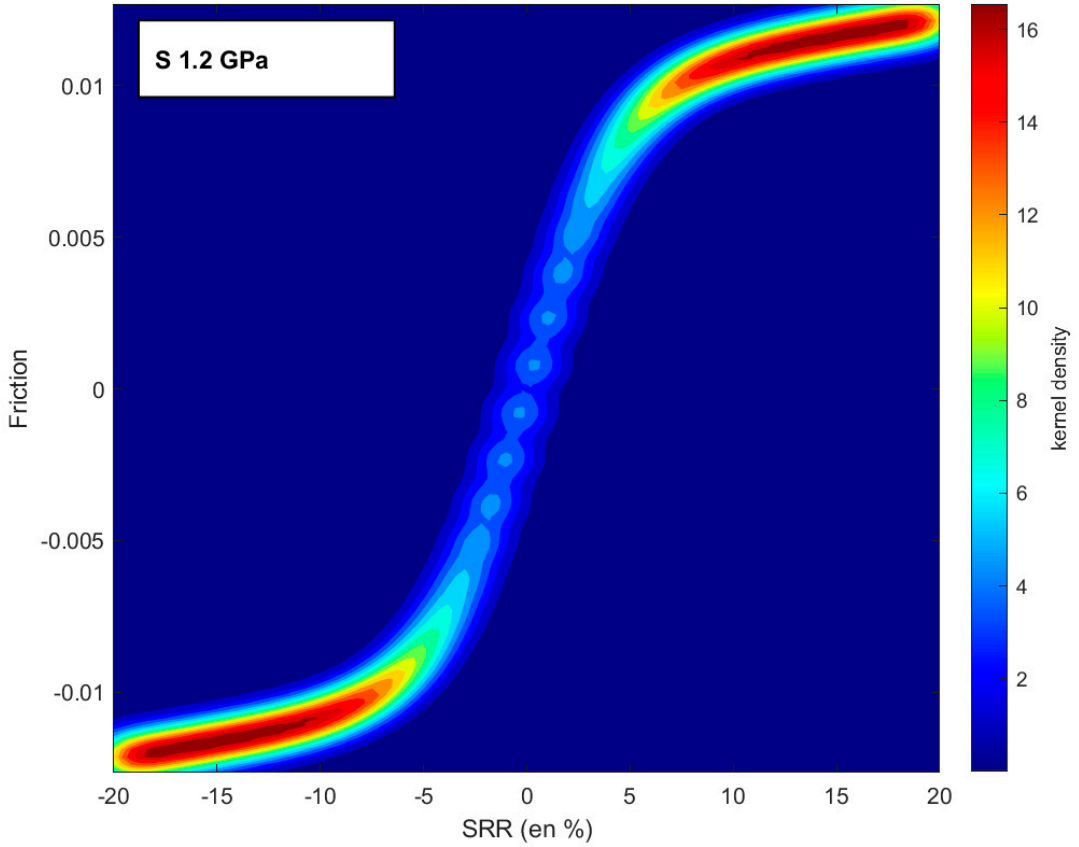


Figure A4 — friction density (uniform SRR) : smooth, 1.6 GPa, 40 °C, 20 m/s

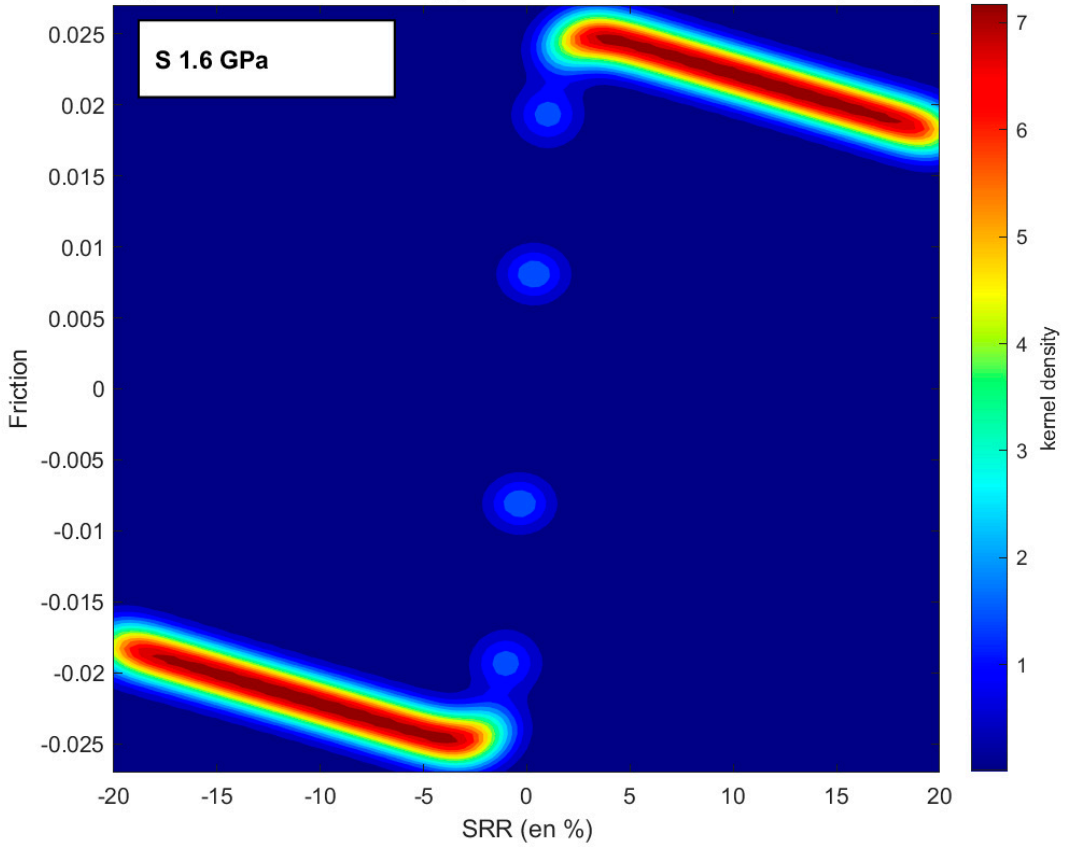


Figure A4 — friction density (uniform SRR) : smooth, 1.6 GPa, 80 °C, 10 m/s

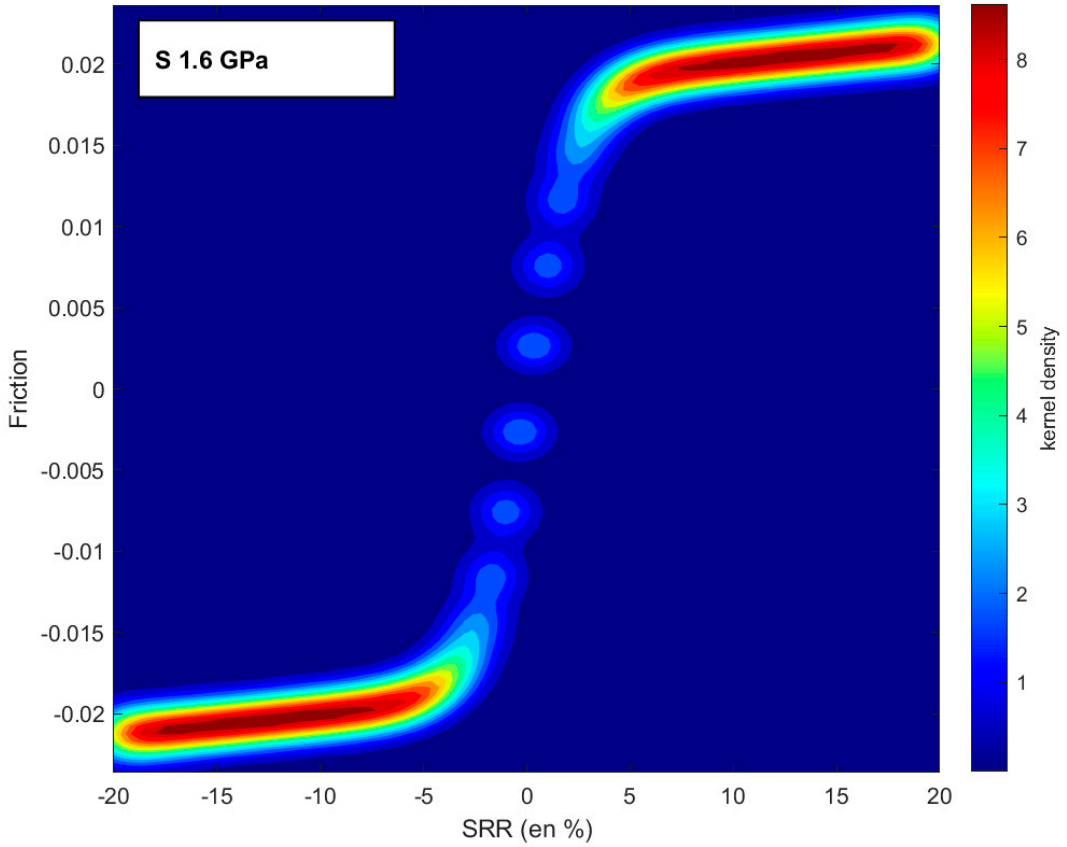


Figure A4 — friction density (uniform SRR) : smooth, 1.6 GPa, 80 °C, 20 m/s

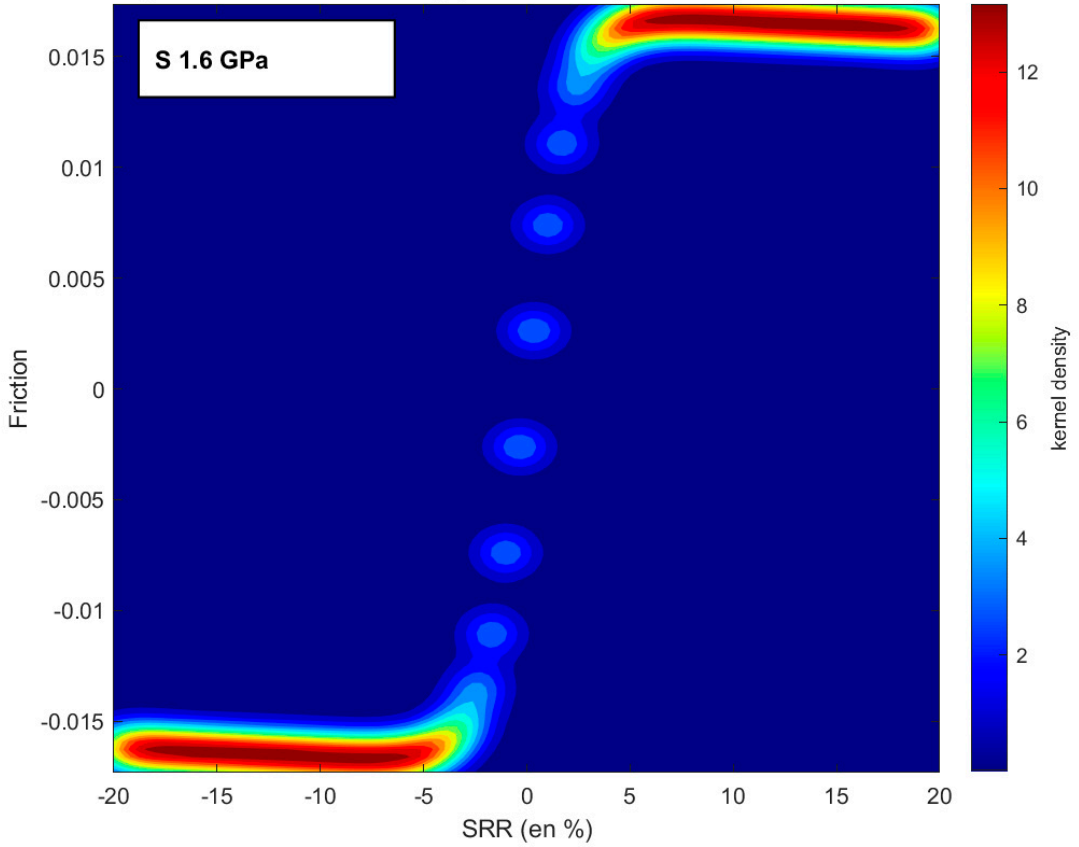


Figure A4 — friction density (uniform SRR) : smooth, 1.6 GPa, 80 °C, 30 m/s

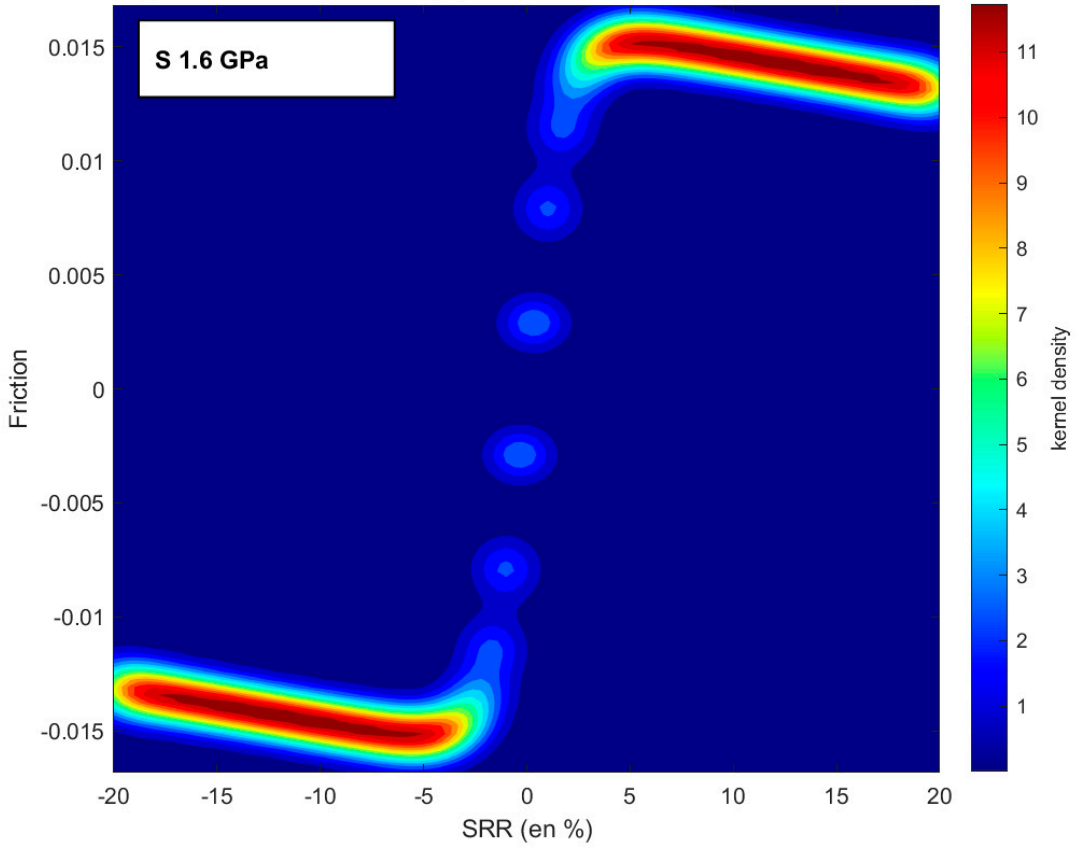
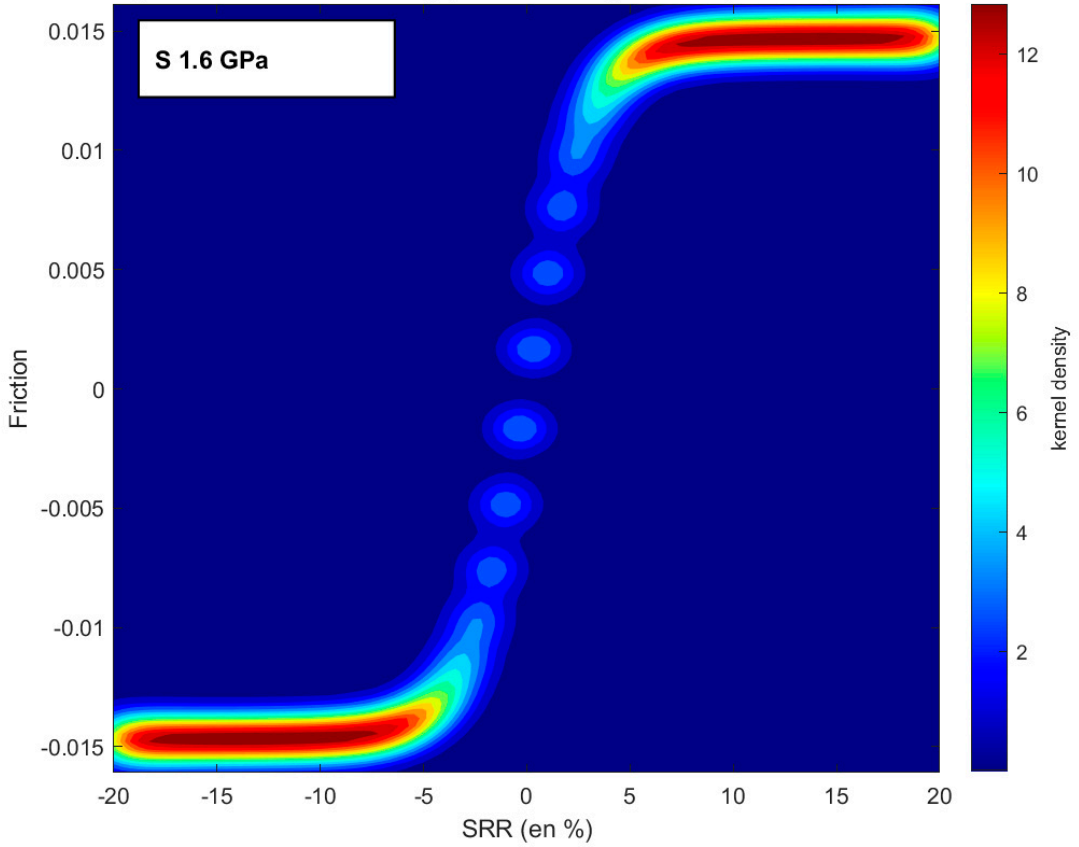


Figure A4 — friction density (uniform SRR) : smooth, 1.6 GPa, 100 °C, 20 m/s



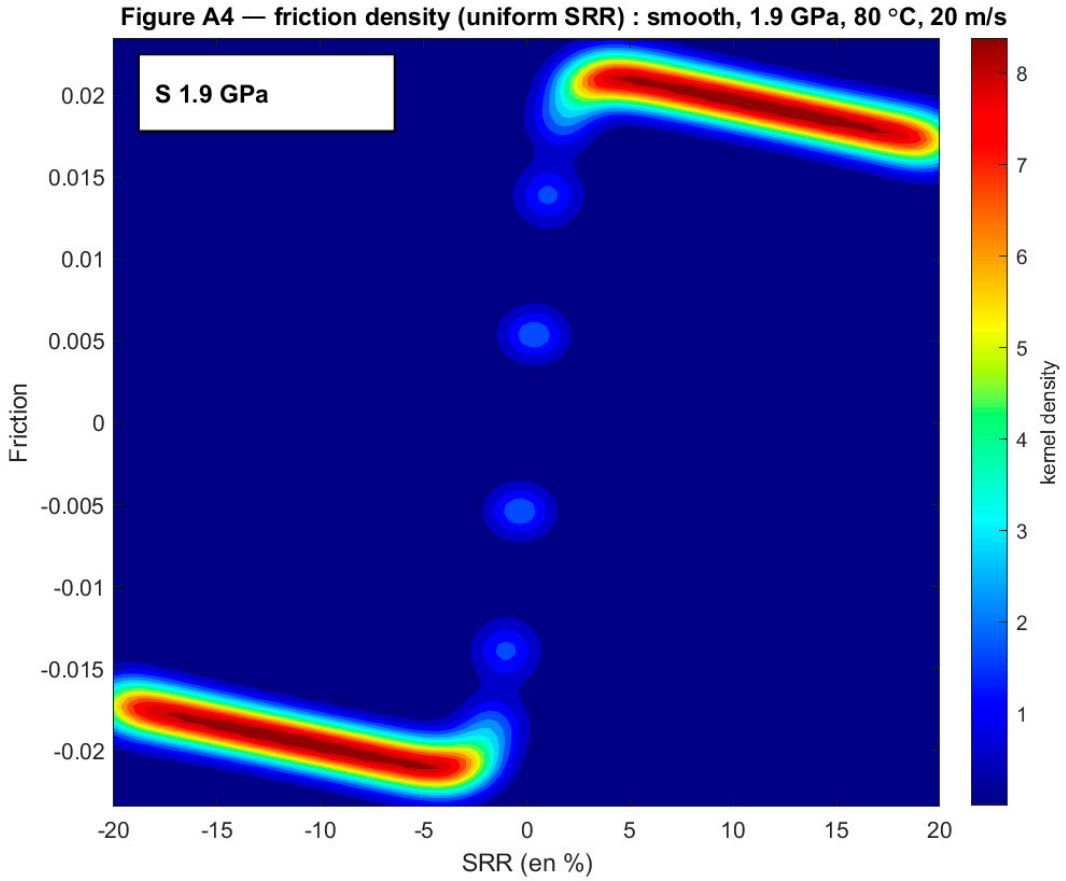


Figure A4. Probability density of the friction coefficient recomputed at evenly spaced SRR intervals from the bootstrapped parameters, for rough and smooth surfaces at each operating condition. High-density regions denote consistent predictions.

A.5. Histograms of the Bootstrapped Parameters (complete set of Figure 9)

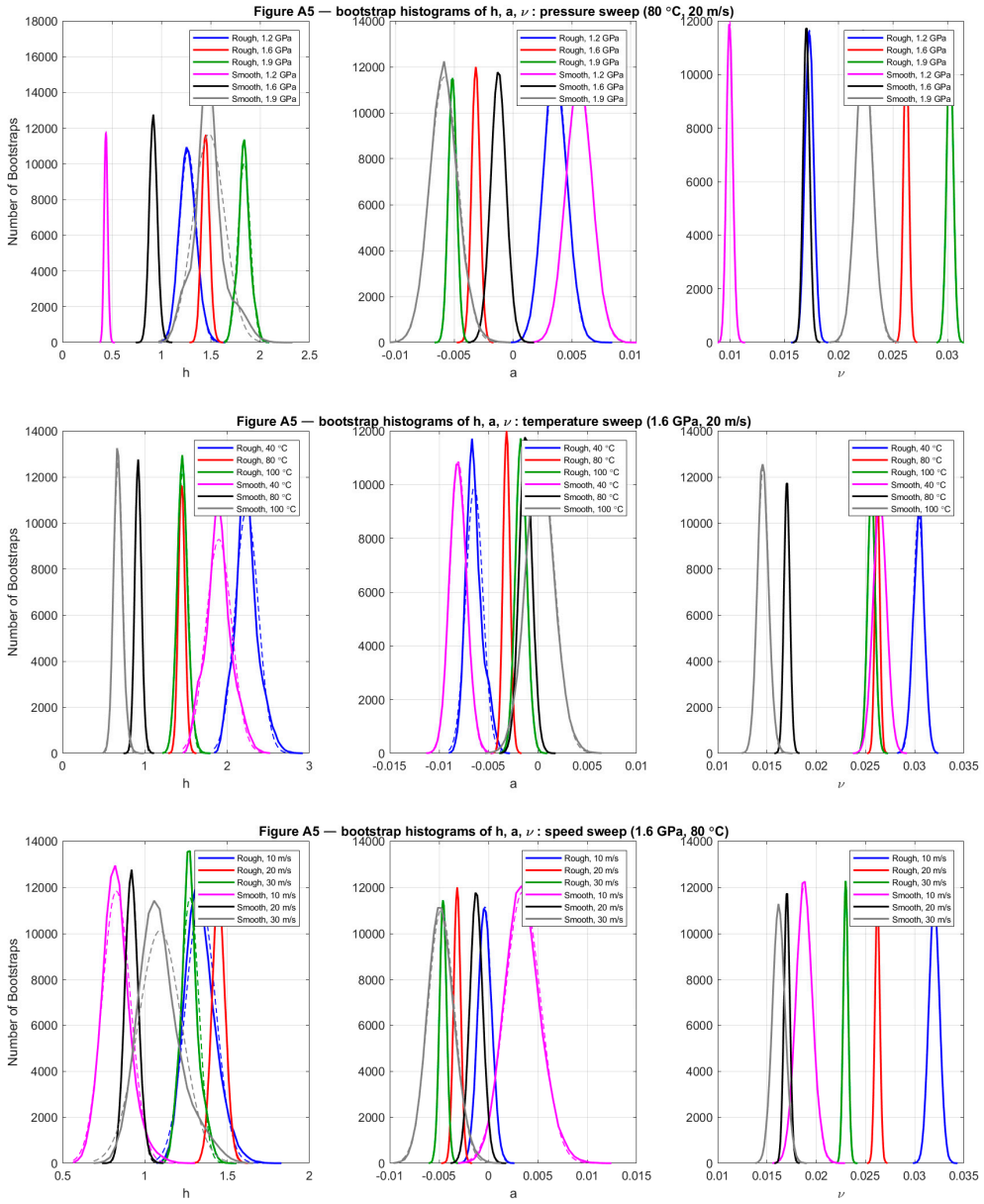


Figure A5. Histograms of the bootstrapped HAF parameters (columns: v, a and h) as a function of the three operating factors of the star design (rows: normal load, oil temperature, entrainment speed), comparing rough and smooth surfaces; for each factor the other two are held at their reference value (1.6 GPa, 80 °C, 20 m·s^{-1}). Each histogram aggregates 10^5 bootstrap samples.

A.6. Box Plots of the Bootstrapped Parameters (complete set of Figure 10)

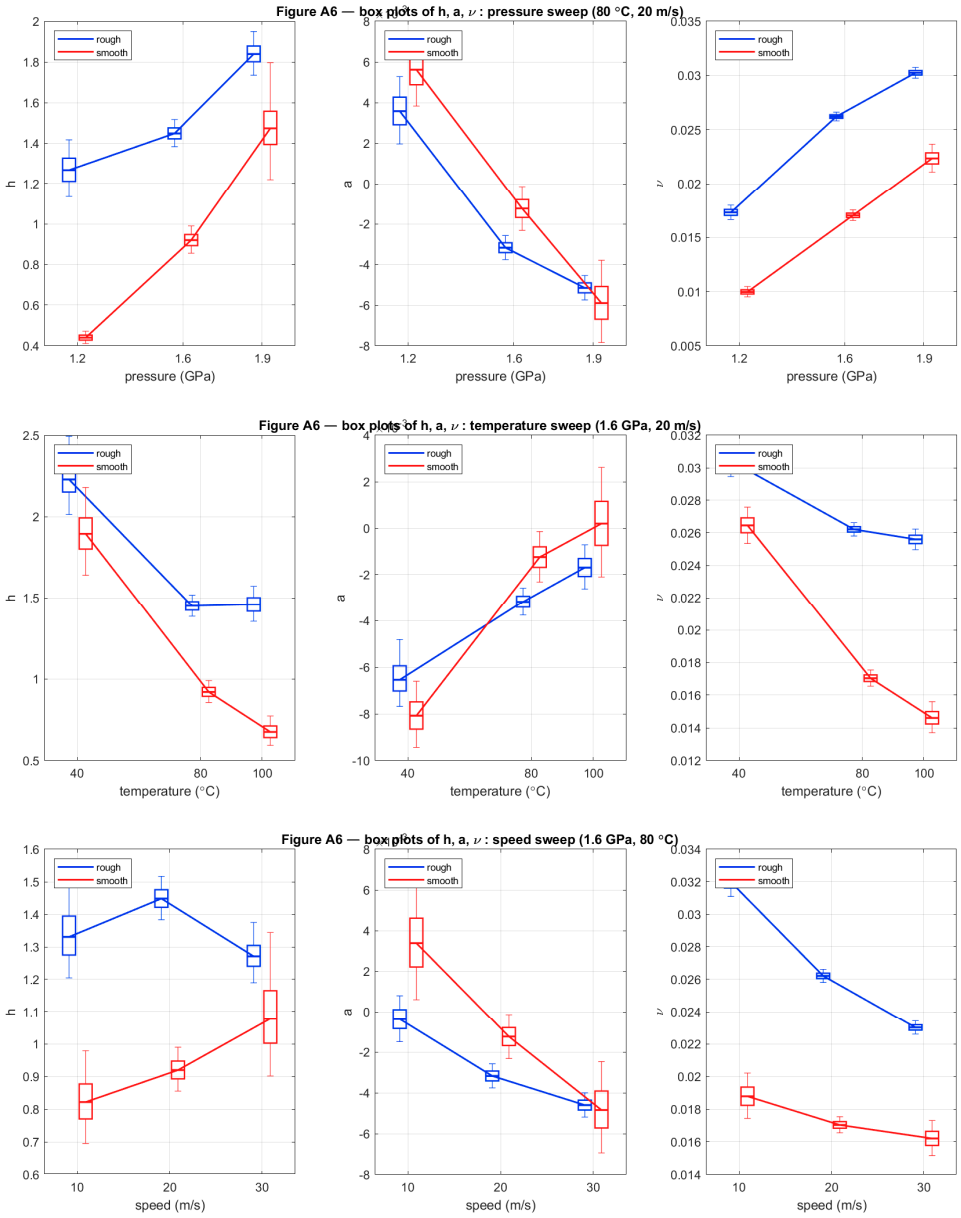


Figure A6. Box plots of the bootstrapped HAF parameters (columns: v, a and h) as a function of the three operating factors of the star design (rows), comparing rough and smooth surfaces: normal load (1.2, 1.6, 1.9 GPa; other factors fixed at 80 °C and 20 $m \cdot s^{-1}$), oil temperature (40, 80, 100 °C; fixed at 1.6 GPa and 20 $m \cdot s^{-1}$) and entrainment speed (10, 20, 30 $m \cdot s^{-1}$; fixed at 1.6 GPa and 80 °C). For each factor the other two are held at their reference value. Boxes show the 5th centile, first quartile, median, third quartile and 95th centile of the 10^5 bootstrap samples.

A.7. Bootstrap Distributions of the Linear-Model Coefficients (complete set of Figure 11)

Figure A7 — intercept coefficients a_i, h_i, ν_i (Eqs. 11-13), per surface — star design: 1.2/1.6/1.9 GPa | 40/80/100 °C | 10/20/30 m/s

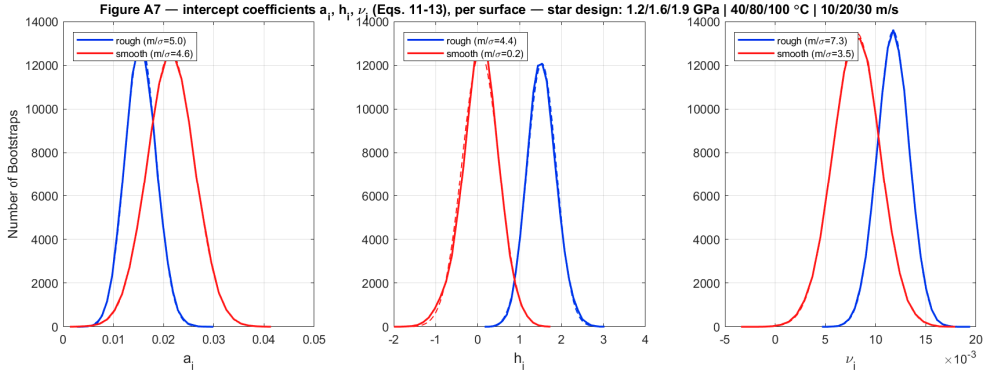


Figure A7 — load coefficients a_l, h_l, ν_l (Eqs. 11-13), per surface — star design: 1.2/1.6/1.9 GPa | 40/80/100 °C | 10/20/30 m/s

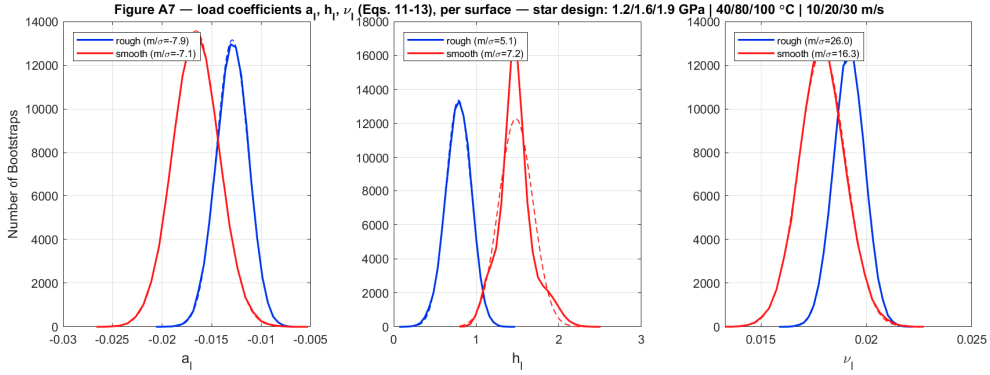


Figure A7 — temperature coefficients a_t, h_t, ν_t (Eqs. 11-13), per surface — star design: 1.2/1.6/1.9 GPa | 40/80/100 °C | 10/20/30 m/s

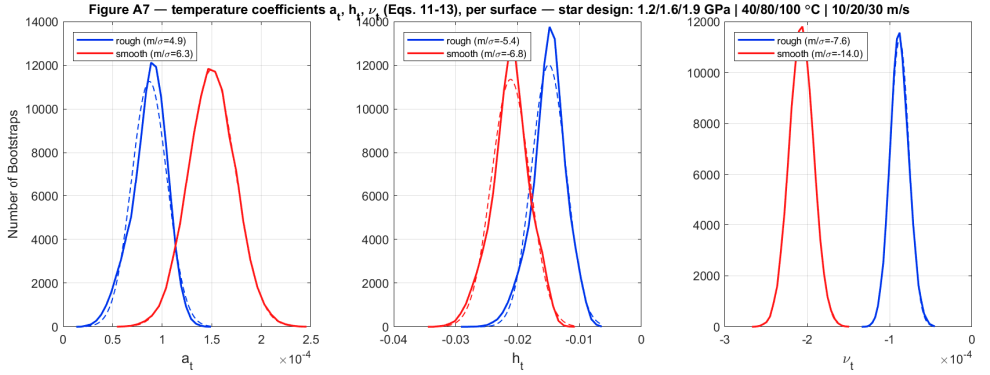


Figure A7 — speed coefficients a_s, h_s, ν_s (Eqs. 11-13), per surface — star design: 1.2/1.6/1.9 GPa | 40/80/100 °C | 10/20/30 m/s

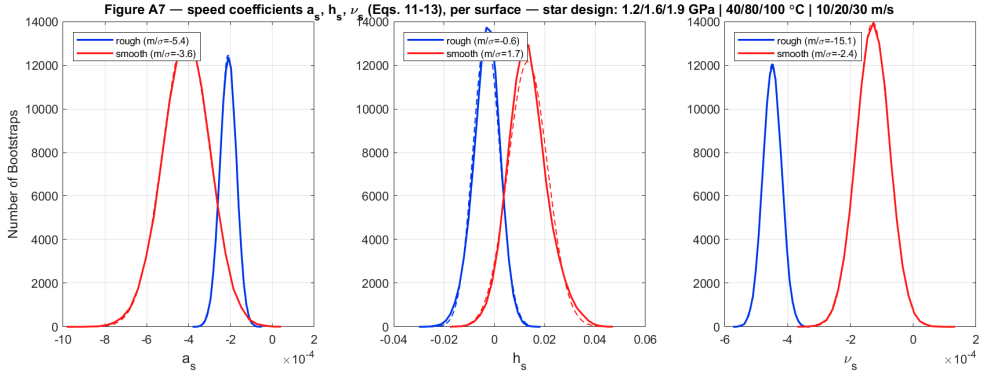
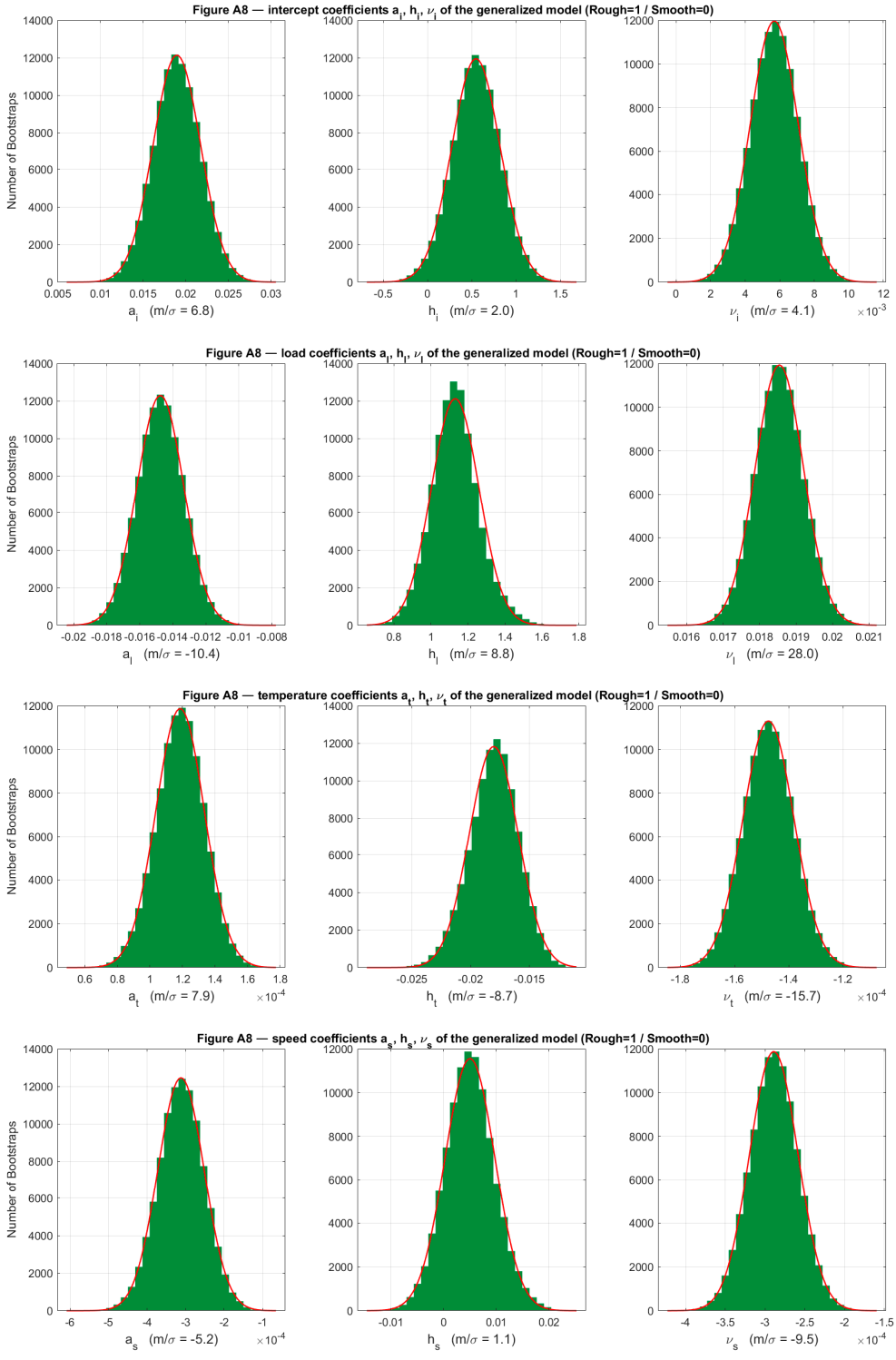


Figure A7. Complete set of the bootstrap distributions of the linear-model coefficients of h, a and v (Section 7.1): rows = intercept, load, temperature and speed effects; columns = a, h and v.

A.8. Bootstrap Distributions of the Generalized-Model Coefficients (complete set of Figure 13)



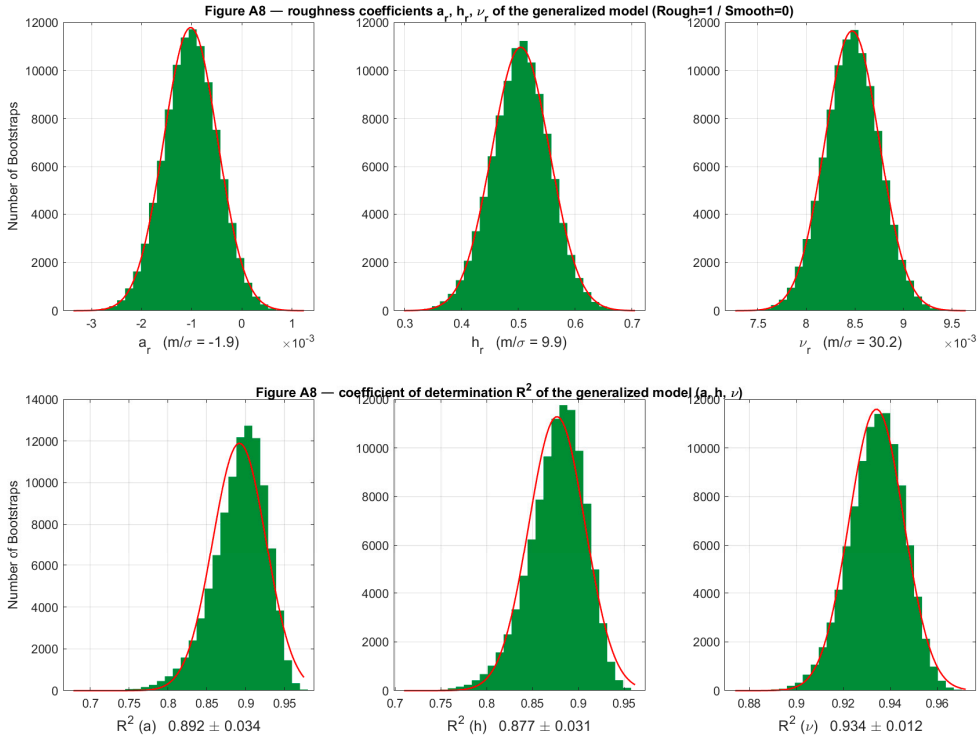
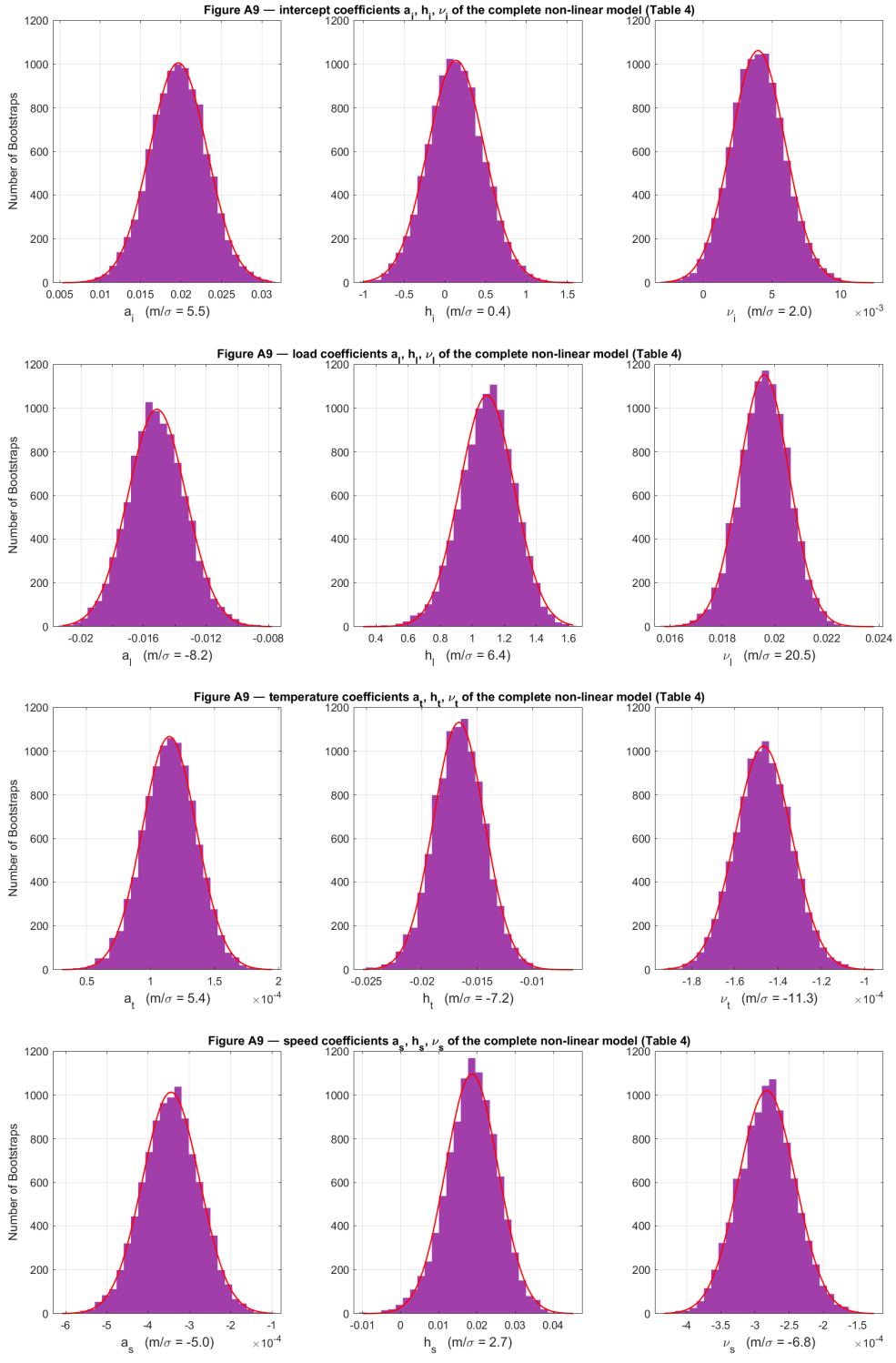
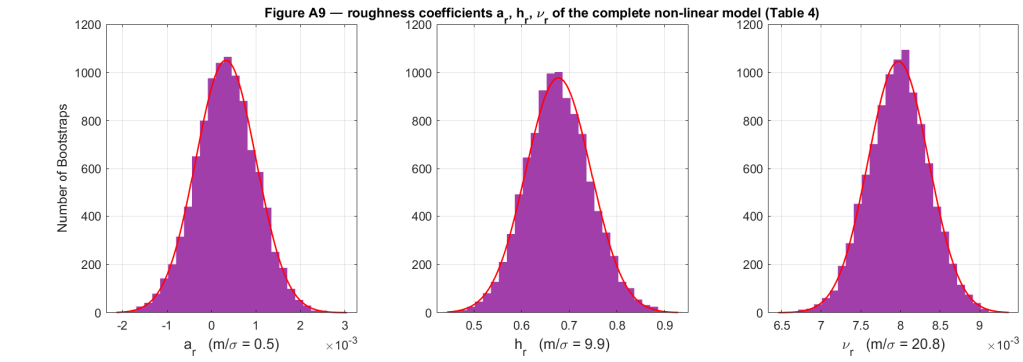


Figure A8. Complete set of the bootstrap distributions of the generalized-model coefficients including roughness (Section 7.2): rows = a, h, v; columns = intercept, load, temperature, speed and roughness effects, plus the associated R^2.

A.9. Bootstrap Distributions of the Complete-Model Coefficients (complete set of Figure 14)





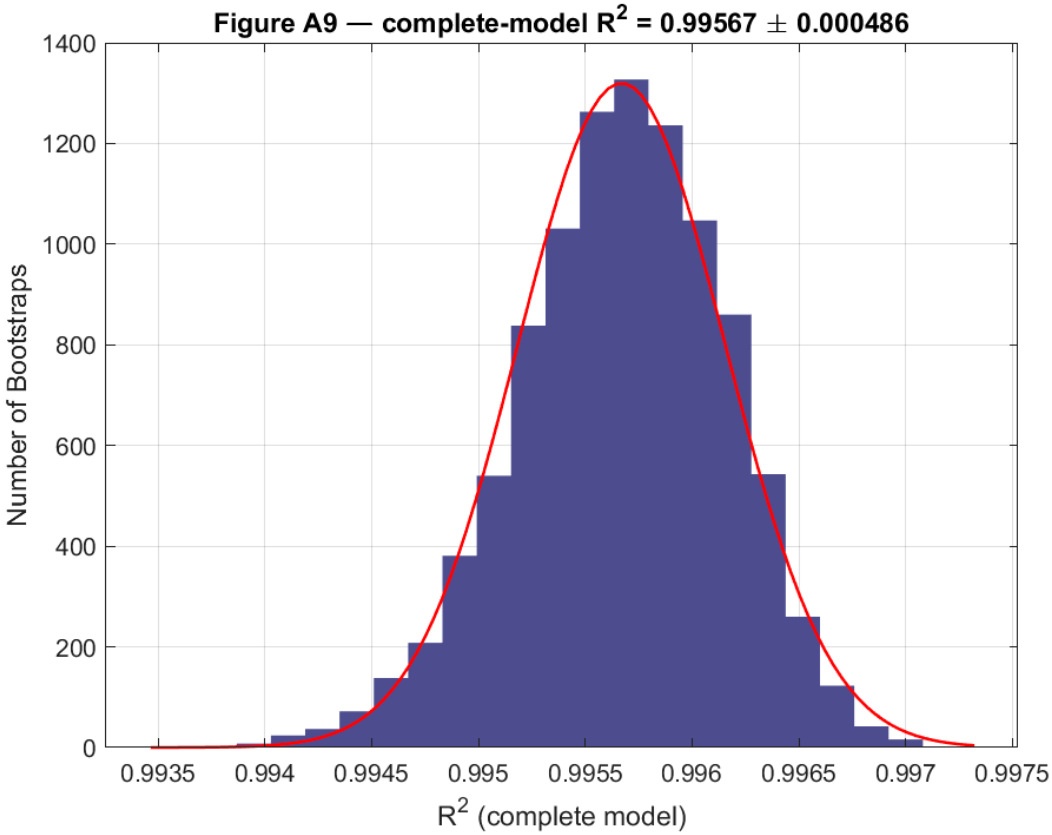
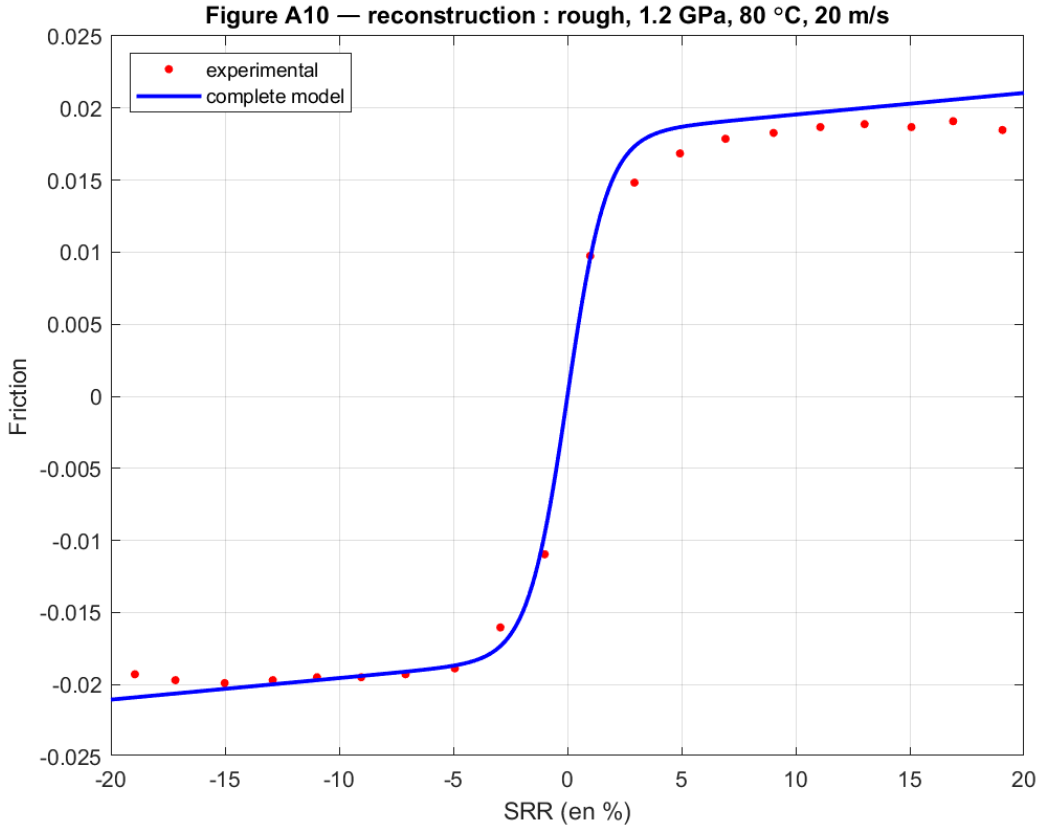
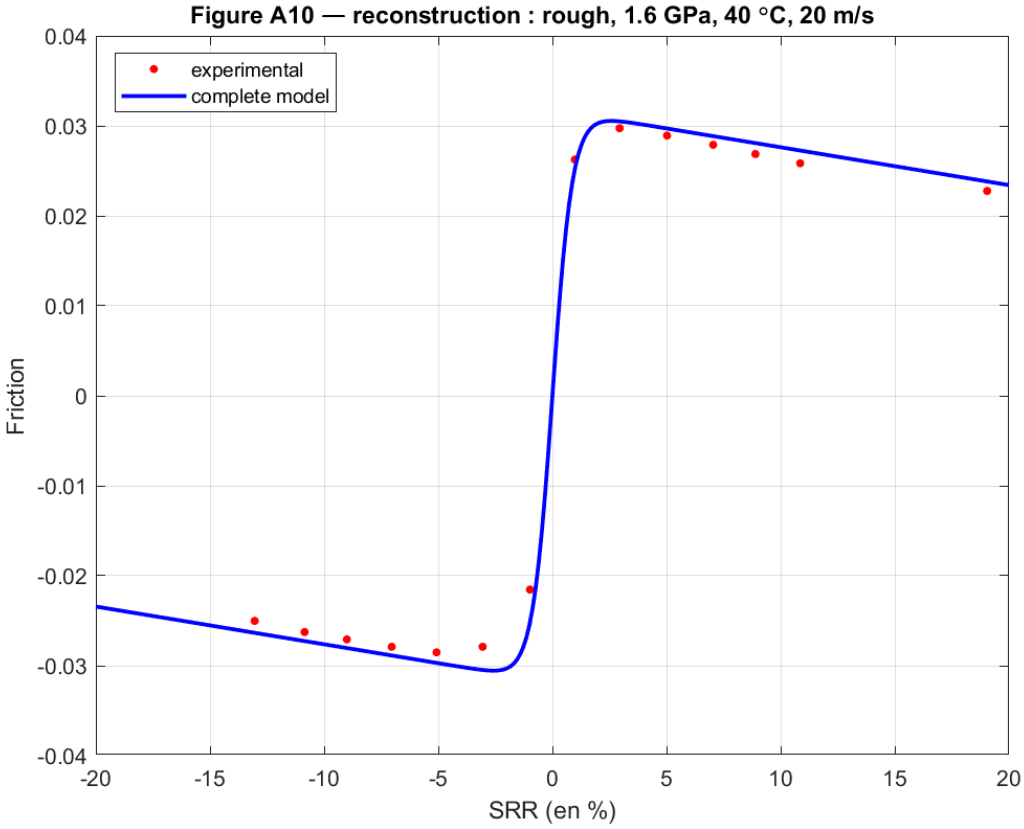
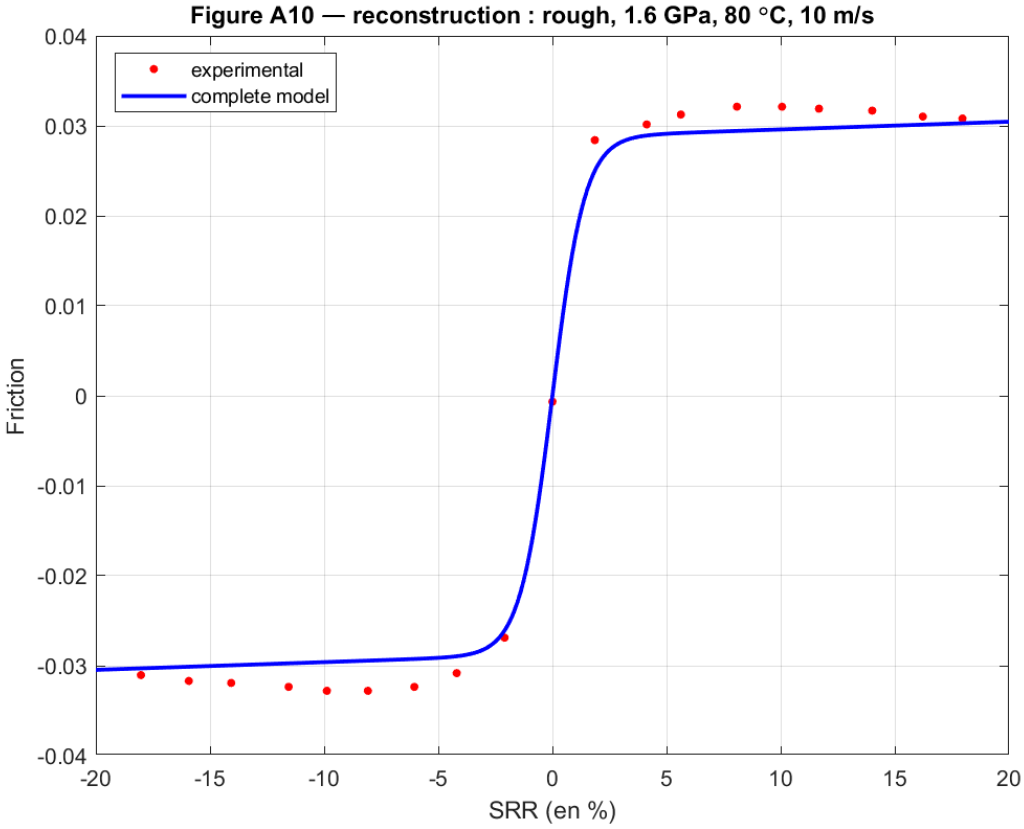


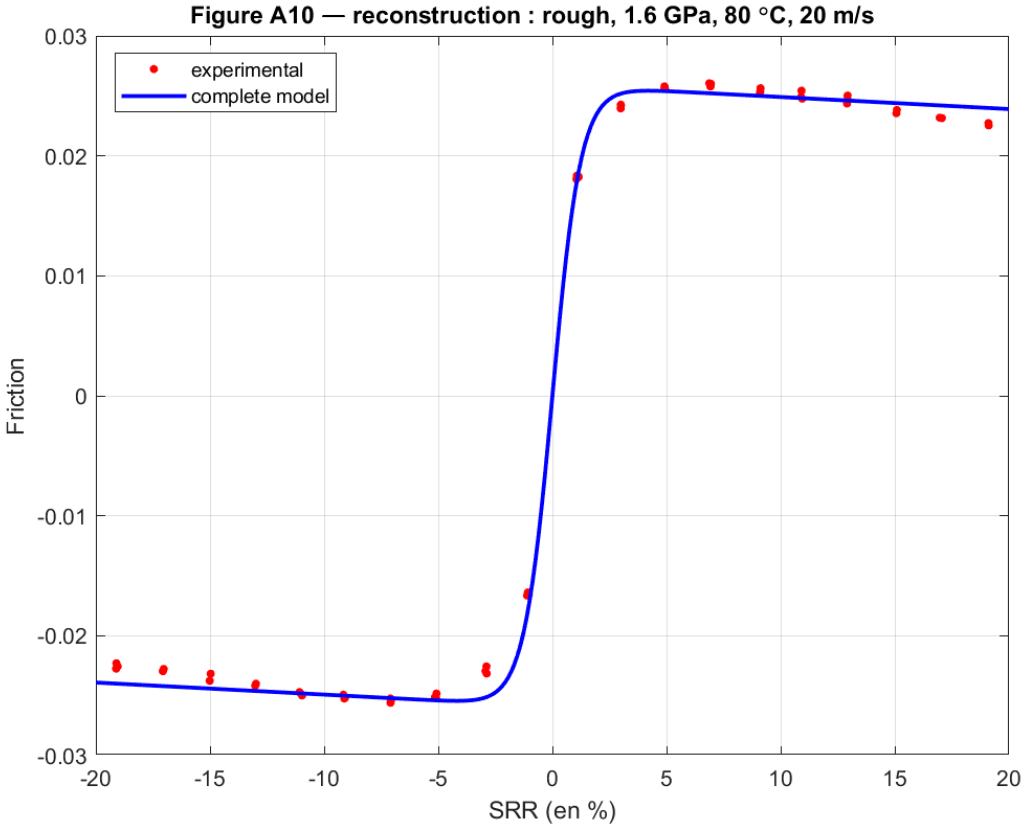
Figure A9. Complete set of the bootstrap distributions of the fifteen coefficients of the complete non-linear predictive model (Section 7.3): rows = a, h, v; columns = intercept, load, temperature, speed and roughness effects.

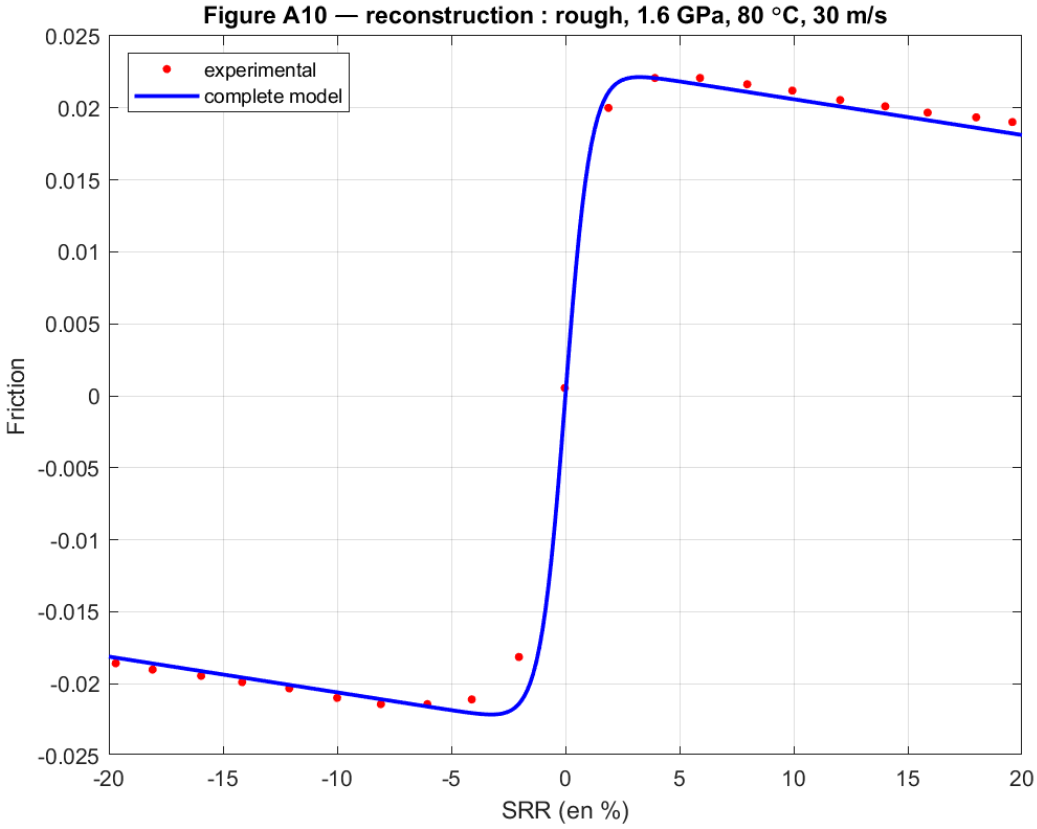
A.10. Recalculated Friction Curves (complete set of Figure 18)

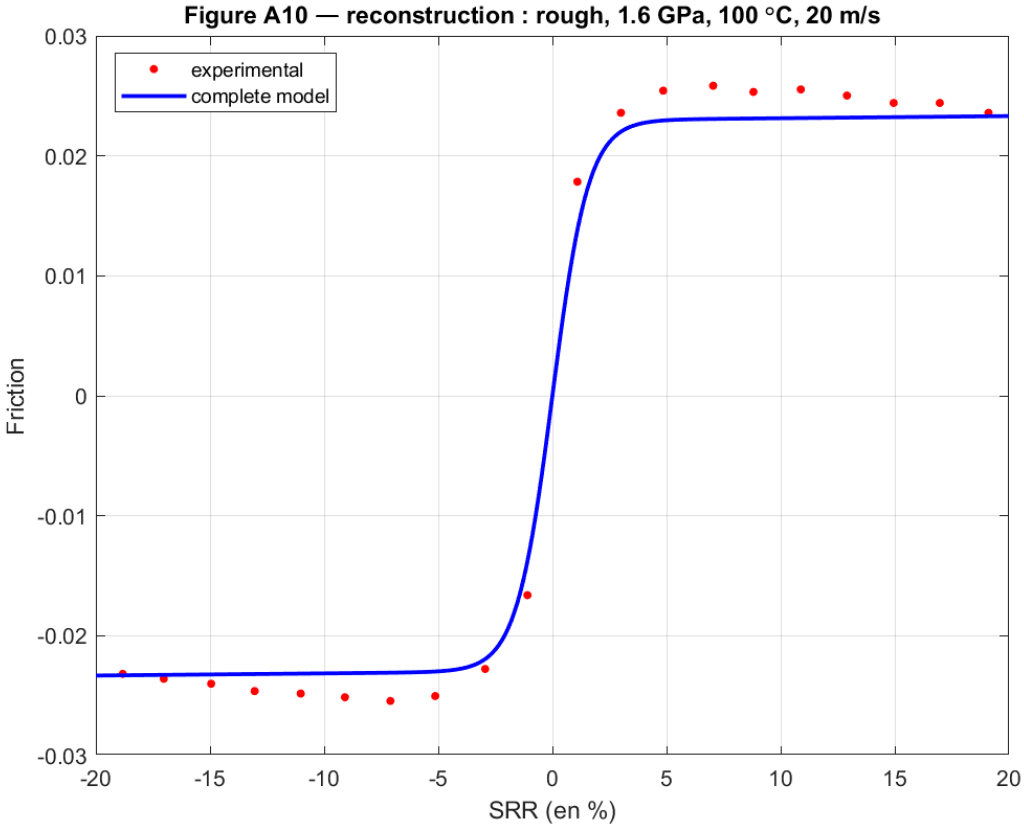


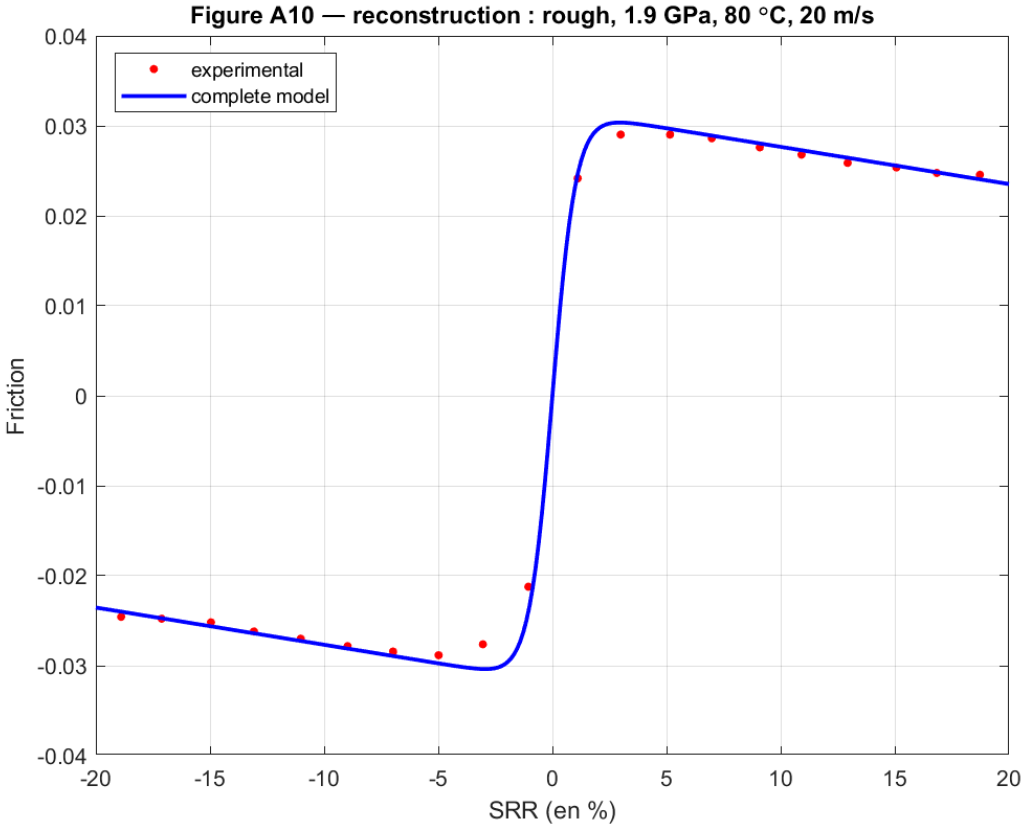

Figure A10 — reconstruction : rough, 1.6 GPa, 40 °C, 20 m/s
experimental
complete model
Friction
SRR (en %)
0.04
0.03
0.02
0.01
0
-0.01
-0.02
-0.03
-0.04
-20
-15
-10
-5
0
5
10
15
20

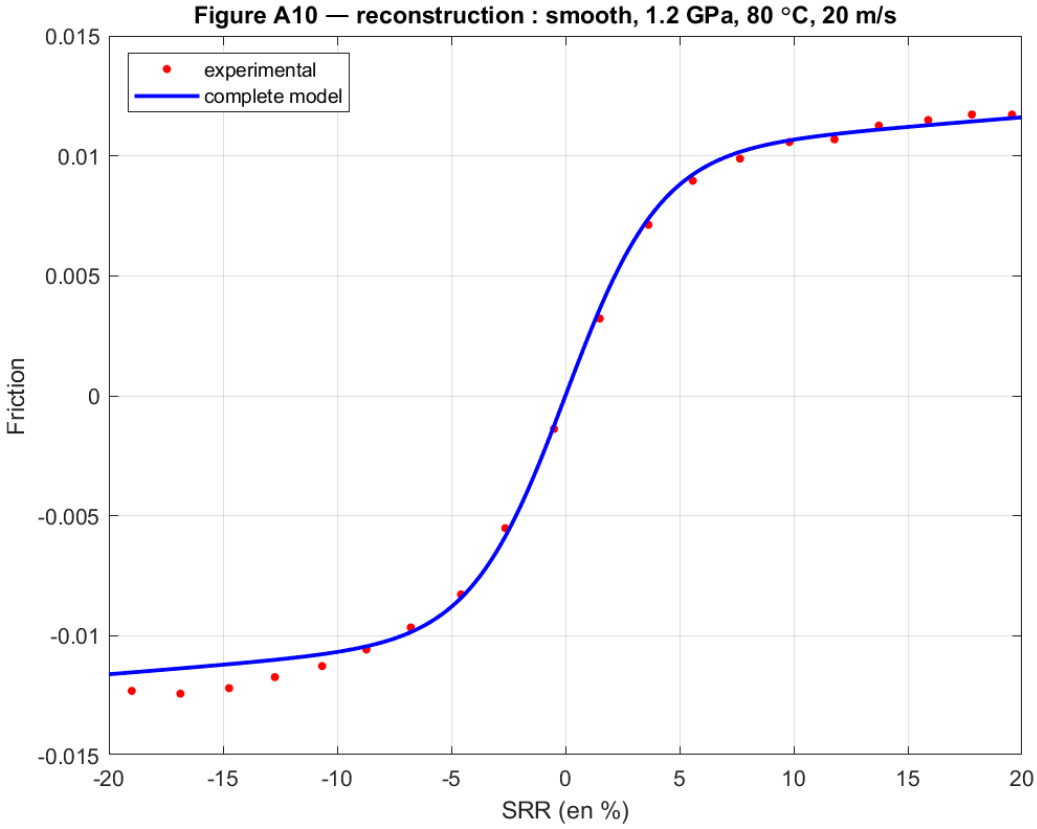

Figure A10 — reconstruction : rough, 1.6 GPa, 80 °C, 10 m/s
experimental
complete model
Friction
SRR (en %)
0.04
0.03
0.02
0.01
0
-0.01
-0.02
-0.03
-0.04
-20
-15
-10
-5
0
5
10
15
20

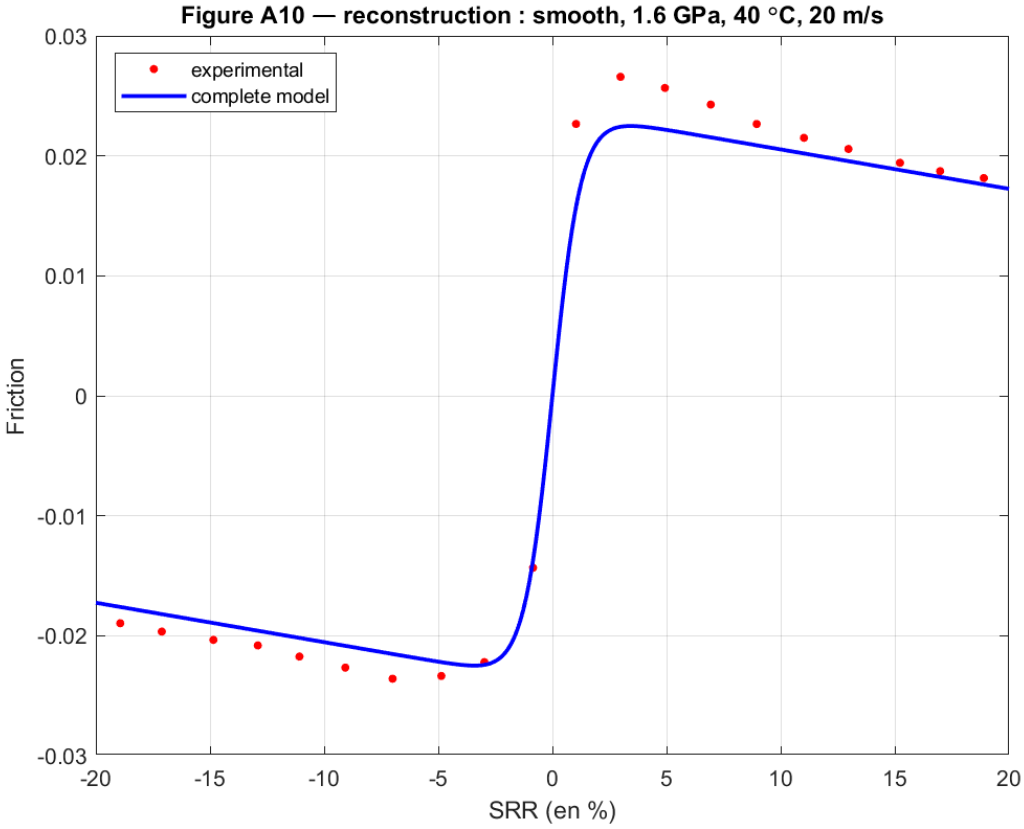

Figure A10 — reconstruction : rough, 1.6 GPa, 80 °C, 20 m/s
experimental
complete model
Friction
SRR (en %)
0.03
0.02
0.01
0
-0.01
-0.02
-0.03
-20
-15
-10
-5
0
5
10
15
20

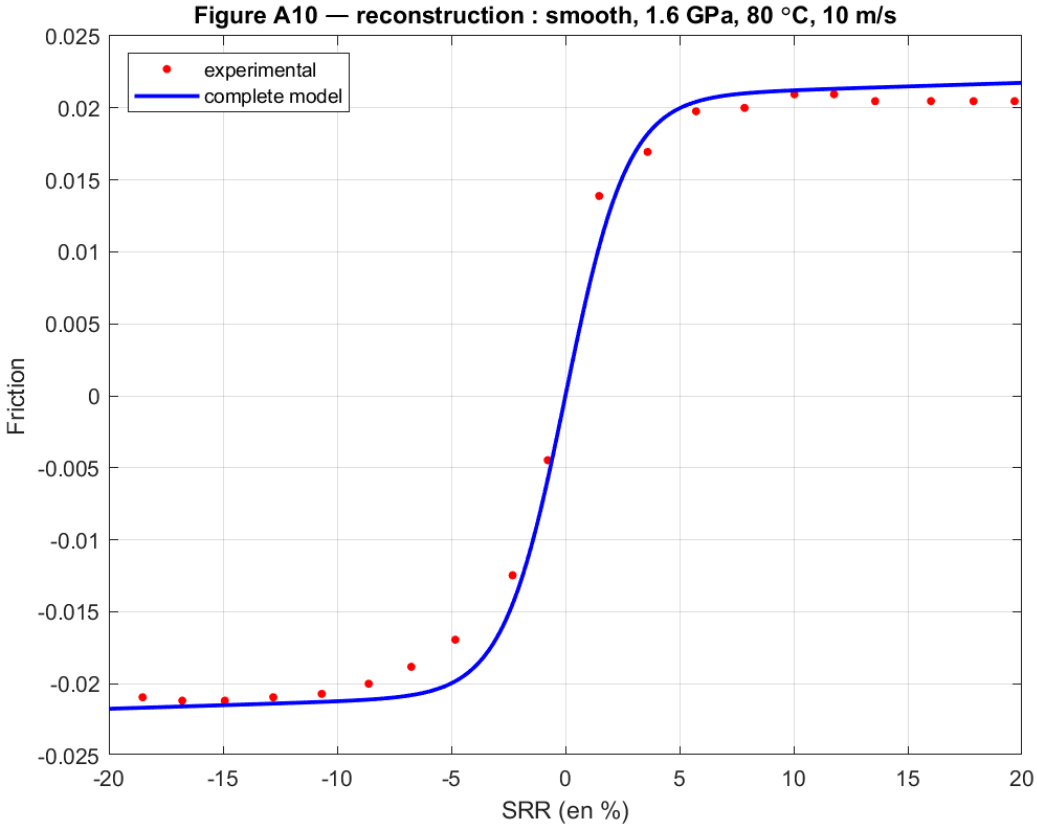

Figure A10 — reconstruction : rough, 1.6 GPa, 80 °C, 30 m/s
experimental
complete model
Friction
SRR (en %)
0.025
0.02
0.015
0.01
0.005
0
-0.005
-0.01
-0.015
-0.02
-0.025
-20
-15
-10
-5
0
5
10
15
20

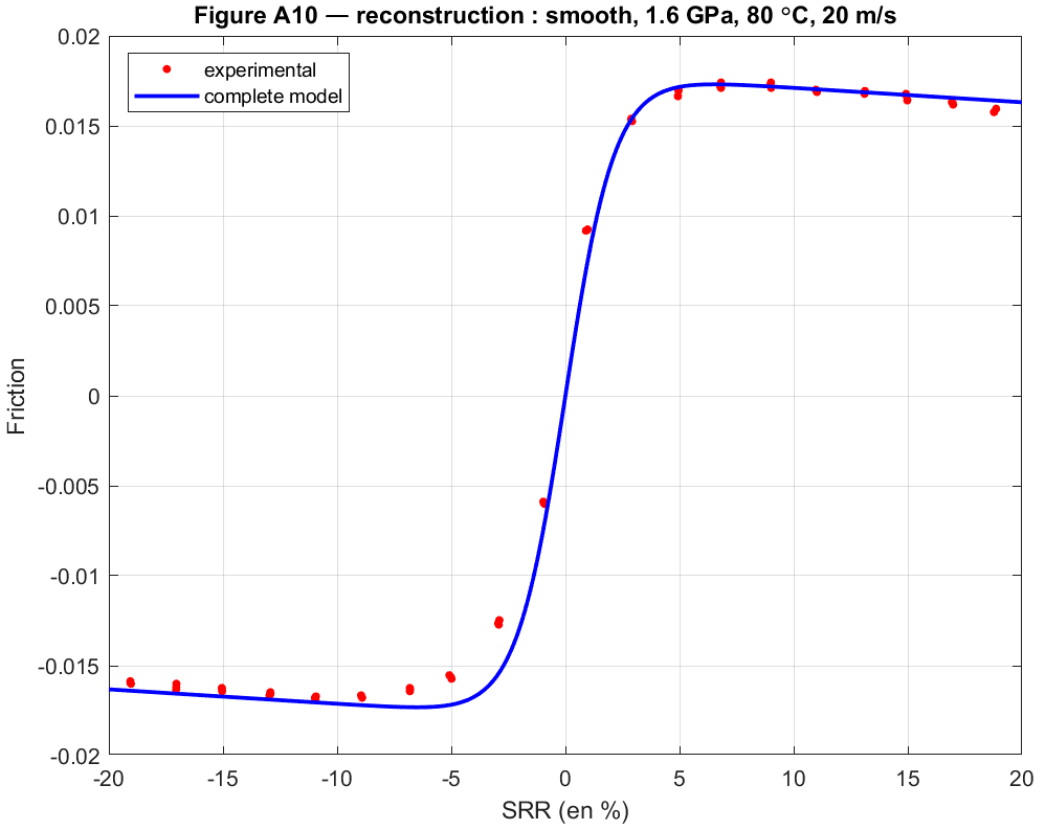

Figure A10 — reconstruction : rough, 1.6 GPa, 100 °C, 20 m/s
experimental
complete model
Friction
SRR (en %)
0.03
0.02
0.01
0
-0.01
-0.02
-0.03
-20
-15
-10
-5
0
5
10
15
20

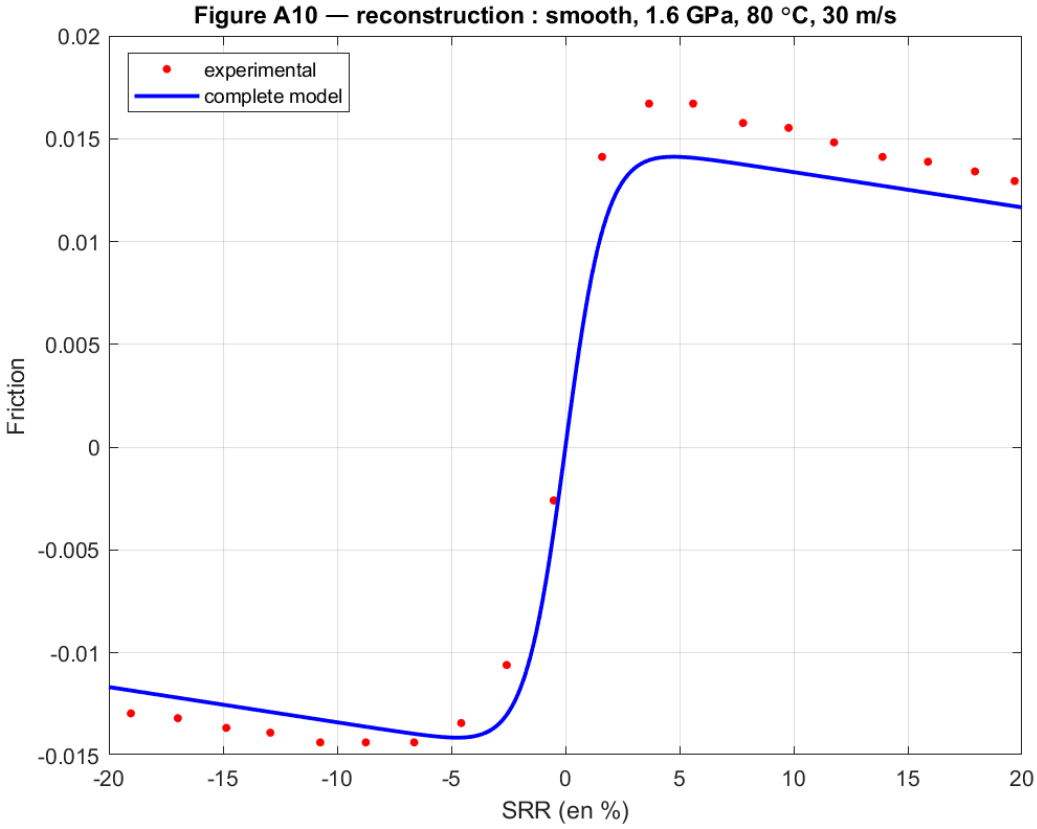

Figure A10 — reconstruction : rough, 1.9 GPa, 80 °C, 20 m/s
experimental
complete model
Friction
SRR (en %)
0.04
0.03
0.02
0.01
0
-0.01
-0.02
-0.03
-0.04
-20
-15
-10
-5
0
5
10
15
20

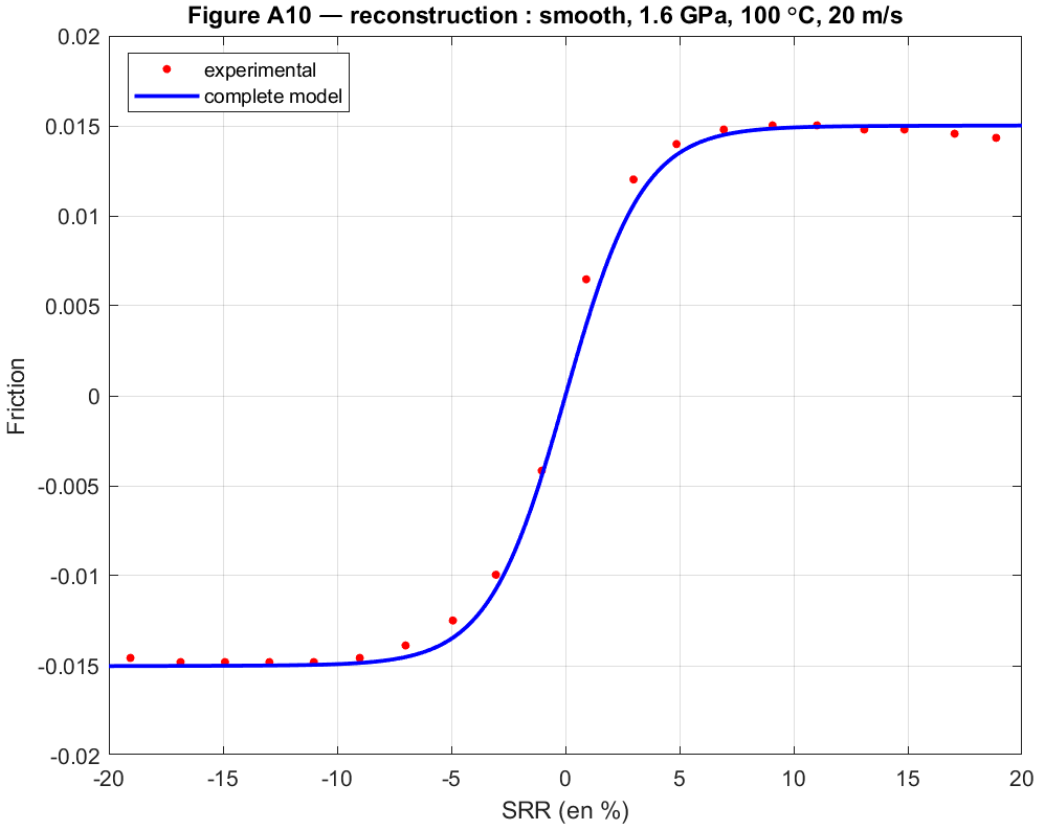

Figure A10 — reconstruction : smooth, 1.2 GPa, 80 °C, 20 m/s
experimental
complete model
Friction
SRR (en %)
0.015
0.01
0.005
0
-0.005
-0.01
-0.015
-20
-15
-10
-5
0
5
10
15
20


Figure A10 — reconstruction : smooth, 1.6 GPa, 40 °C, 20 m/s
experimental
complete model
Friction
SRR (en %)
0.03
0.02
0.01
0
-0.01
-0.02
-0.03
-20
-15
-10
-5
0
5
10
15
20


Figure A10 — reconstruction : smooth, 1.6 GPa, 80 °C, 10 m/s
experimental
complete model
Friction
SRR (en %)
0.025
0.02
0.015
0.01
0.005
0
-0.005
-0.01
-0.015
-0.02
-0.025
-20
-15
-10
-5
0
5
10
15
20


Figure A10 — reconstruction : smooth, 1.6 GPa, 80 °C, 20 m/s
experimental
complete model
Friction
SRR (en %)
0.02
0.015
0.01
0.005
0
-0.005
-0.01
-0.015
-0.02
-20
-15
-10
-5
0
5
10
15
20


Figure A10 — reconstruction : smooth, 1.6 GPa, 80 °C, 30 m/s
experimental
complete model
Friction
SRR (en %)
0.02
0.015
0.01
0.005
0
-0.005
-0.01
-0.015
-20
-15
-10
-5
0
5
10
15
20


Figure A10 — reconstruction : smooth, 1.6 GPa, 100 °C, 20 m/s
experimental
complete model
Friction
SRR (en %)
0.02
0.015
0.01
0.005
0
-0.005
-0.01
-0.015
-0.02
-20
-15
-10
-5
0
5
10
15
20

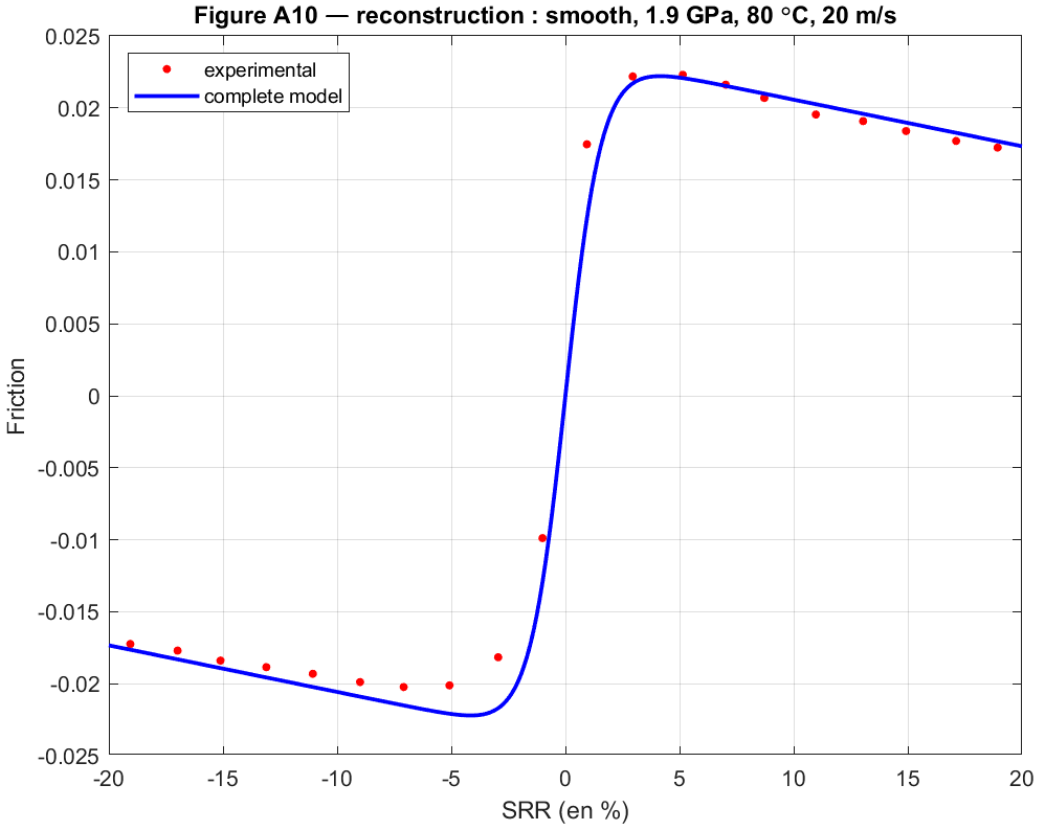


Figure A10. Experimental friction curves (points) and their reconstruction by the complete model (lines) for the full set of operating conditions (Section 7.3).

References

1. Quiban, R.; Grenet de Bechillon, N.; Touret, T.; Navet, P.; Diab, Y.; Cavoret, J.; Ville, F.; Changenet, C. On the interest of a semi-empirical model for the tooth friction coefficient in gear transmissions. Proc. Inst. Mech. Eng. Part J J. Eng. Tribol. 2021, 235, 2654–2663. https://doi.org/10.1177/13506501211052179

2. Britton, R.D.; Elcoate, C.D.; Alanou, M.P.; Evans, H.P.; Snidle, R.W. Effect of surface finish on gear tooth friction. J. Tribol. 2000, 122, 354–360. https://doi.org/10.1115/1.555367

3. Akbarzadeh, S.; Khonsari, M.M. Performance of spur gears considering surface roughness and shear-thinning lubricant. J. Tribol. 2008, 130, 021503. https://doi.org/10.1115/1.2805431

4. Zhmud, B.; Najjari, M.; Brodmann, B. The effects of the lubricant properties and surface finish characteristics on the tribology of high-speed gears for EV transmissions. Lubricants 2024, 12, 112. https://doi.org/10.3390/lubricants12040112

5. Yan, S.; Kong, Z.; Liu, H.; et al. Power loss evaluation of an E-axle gearbox considering the influence of gear oil factors. Lubricants 2024, 12, 11. https://doi.org/10.3390/lubricants12010011

6. Paturi, U.M.R.; Palakurthy, S.T.; Reddy, N.S. The role of machine learning in tribology: a systematic review. Arch. Comput. Methods Eng. 2023, 30, 1345–1397. https://doi.org/10.1007/s11831-022-09841-5

7. Marian, M.; Tremmel, S. Recent advances in machine learning in tribology. Lubricants 2024, 12, 168. https://doi.org/10.3390/lubricants12050168

8. Diab, Y.; Ville, F.; Velex, P. Prediction of power losses due to tooth friction in gears. Tribol. Trans. 2006, 49, 260–270. https://doi.org/10.1080/05698190600614874

9. Liu, L.; Kong, R.; Chen, Z. Prediction of mechanical efficiency of spur gear pairs based on tribo-dynamics model of multi-tooth meshing. Proc. Inst. Mech. Eng. Part J J. Eng. Tribol. 2024. https://doi.org/10.1177/13506501241238280

10. Diab, Y.; Touret, T.; Ville, F.; Changenet, C. Tooth friction in spur gear transmission: from local to mean tooth friction loss. Proc. Inst. Mech. Eng. Part J J. Eng. Tribol. 2024. https://doi.org/10.1177/13506501241272847

11. Bair, S.; Habchi, W. Quantitative elastohydrodynamic lubrication—seventeen years in. ASME J. Tribol. 2024, 146, 080801. https://doi.org/10.1115/1.4065299

12. Bair, S. The high-pressure rheology of gear oils. Proc. Inst. Mech. Eng. Part J J. Eng. Tribol. 2025. https://doi.org/10.1177/13506501251358926

13. Efron, B.; Tibshirani, R.J. An Introduction to the Bootstrap; Chapman & Hall: New York, NY, USA, 1993.

14. Olver, A.V.; Spikes, H.A. Prediction of traction in elastohydrodynamic lubrication. Proc. Inst. Mech. Eng. Part J J. Eng. Tribol. 1998, 212, 321–346. https://doi.org/10.1243/1350650981542137

15. Xu, H.; Kahraman, A.; Anderson, N.E.; Maddock, D.G. Prediction of mechanical efficiency of parallel-axis gear pairs. J. Mech. Des. 2007, 129, 58–68. https://doi.org/10.1115/1.2359478

16. Arana, A.; Larrañaga, J.; Ulacia, I. Partial EHL friction coefficient model to predict power losses in cylindrical gears. Proc. Inst. Mech. Eng. Part J J. Eng. Tribol. 2019, 233, 303–316. https://doi.org/10.1177/1350650118778655

17. Benedict, G.H.; Kelley, B.W. Instantaneous coefficients of gear tooth friction. ASLE Trans. 1961, 4, 59–70. https://doi.org/10.1080/05698196108972420

18. Kelley, B.W.; Lemanski, A.J. Lubrication of involute gearing. Proc. Inst. Mech. Eng. 1967, 182, 173–184.

19. Fernandes, C.M.C.G.; Martins, R.C.; Seabra, J.H.O. Coefficient of friction equation for gears based on a modified Hersey parameter. Tribol. Int. 2016, 101, 204–217. https://doi.org/10.1016/j.triboint.2016.03.028

20. Johnson, K.L.; Tevaarwerk, J.L. Shear behaviour of elastohydrodynamic oil films. Proc. R. Soc. Lond. A 1977, 356, 215–236. https://doi.org/10.1098/rspa.1977.0129

21. Bair, S.; Habchi, W. Rheology extracted from traction curves: is there enough information? ASME J. Tribol. 2026, 148, 081101. https://doi.org/10.1115/1.4069376

22. Bair, S.; Habchi, W. Elastohydrodynamic lubrication traction coefficient is not a property of the liquid alone. ASME J. Tribol. 2025, 147, 044501. https://doi.org/10.1115/1.4067692

23. Transtrum, M.K.; Machta, B.B.; Sethna, J.P. Geometry of nonlinear least squares with applications to sloppy models and optimization. Phys. Rev. E 2011, 83, 036701. https://doi.org/10.1103/PhysRevE.83.036701

24. Gutenkunst, R.N.; Waterfall, J.J.; Casey, F.P.; Brown, K.S.; Myers, C.R.; Sethna, J.P. Universally sloppy parameter sensitivities in systems biology models. PLoS Comput. Biol. 2007, 3, e189. https://doi.org/10.1371/journal.pcbi.0030189

25. Cordier, M.; Diab, Y.; Cavoret, J.; Majdoub, F.; Changenet, C.; Ville, F. An experimental study on the impact of roughness orientation on the friction coefficient in EHL contact. Lubricants 2025, 13, 340. https://doi.org/10.3390/lubricants13080340

26. Prajapati, D.K.; Hansen, J.; Björling, M. An assessment of the effect of surface topography on coefficient of friction for lubricated non-conformal contacts. Front. Mech. Eng. 2024, 10, 1360023. https://doi.org/10.3389/fmech.2024.1360023

27. Cheng, G.; Ma, J.; Li, J.; Sun, K.; Wang, K.; Wang, Y. Study on the dynamic characteristics of gears considering surface topography in a mixed lubrication state. Lubricants 2024, 12, 7. https://doi.org/10.3390/lubricants12010007

28. Mao, K. Gear tooth contact analysis and its application in the reduction of fatigue wear. Wear 2007, 262, 1281–1288. https://doi.org/10.1016/j.wear.2006.06.019

29. Yoshizaki, M.; Naruse, C.; Nemoto, R.; Haizuka, S. Study on frictional loss of spur gears. Tribol. Trans. 1991, 34, 138–146. https://doi.org/10.1080/10402009108982021

30. Fernandes, C.M.C.G.; Marques, P.M.T.; Martins, R.C.; Seabra, J.H.O. Gearbox power loss. Part II: Friction losses in gears. Tribol. Int. 2015, 88, 309–316. https://doi.org/10.1016/j.triboint.2014.12.004

31. Velex, P.; Ville, F. An analytical approach to tooth friction losses in spur and helical gears — influence of profile modifications. J. Mech. Des. 2009, 131, 101008. https://doi.org/10.1115/1.3179156

32. Höhn, B.-R.; Michaelis, K.; Hinterstoißer, M. Optimization of gearbox efficiency. Goriva i Maziva 2009, 48, 462–480.

33. Granja, V.; Higgs, C.F. Deep learning data-driven model for Stribeck curve prediction of lubricated tribo-pairs. Lubricants 2026, 14, 25. https://doi.org/10.3390/lubricants14010025